8-2022

Fundamental understanding of the transient melt pool dynamics, solidification kinetics and build texture in spot-melt additive manufacturing of Ti-6Al-4V

Rakesh Rajaram Kamath
University of Tennessee, Knoxville, rkamath@vols.utk.edu

To the Graduate Council:

I am submitting herewith a dissertation written by Rakesh Rajaram Kamath entitled "Fundamental understanding of the transient melt pool dynamics, solidification kinetics and build texture in spot-melt additive manufacturing of Ti-6Al-4V." I have examined the final electronic copy of this dissertation for form and content and recommend that it be accepted in partial fulfillment of the requirements for the degree of Doctor of Philosophy, with a major in Materials Science and Engineering.

Hahn Choo, Major Professor

We have read this dissertation and recommend its acceptance:

Sudarsanam S. Babu, Yanfei Gao, Ke An

Accepted for the Council:

Dixie L. Thompson

Vice Provost and Dean of the Graduate School

(Original signatures are on file with official student records.)

Fundamental understanding of the transient melt pool dynamics, solidification kinetics and build texture in spot-melt additive manufacturing of Ti-6Al-4V

A Dissertation Presented for the
Doctor of Philosophy
Degree
The University of Tennessee, Knoxville

Rakesh Rajaram Kamath
August 2022

DEDICATION

This thesis is dedicated to my parents, Rekha and Rajaram Kamath.

ACKNOWLEDGEMENTS

First and foremost, I would like to express my sincere gratitude to my thesis advisor, Prof. Hahn Choo, who helped me become a better researcher through his patient guidance and support. I will always cherish our discussions which pushed me to think deeper and harder about the underlying science and ask the right questions first. His advice on always keeping an eye on the bigger picture and about going the extra mile while making research presentations has helped me become more effective and efficient while communicating my findings.

Next, I would like to express my sincere thanks to my dissertation committee members, Prof. Sudarsanam Suresh Babu, Prof. Yanfei Gao and Dr. Ke An, who provided me with valuable suggestions to improve my thesis and much-needed encouragement during my PhD journey.

I would like to thank my colleagues from the Choo group – Dr. Peijun Hou, Dr. Yuan Li, Dr. Hyojin Park and Dr. Kin-Ling Sham for all the stimulating discussions on metallurgy, life, their native cultures and more. I would like to thank my bright and hard-working undergraduate colleagues for their help with radiography and other projects before (and for lending a patient ear to my "teaching" moments) - Logan White, Ryan Heldt, Raymond Wysmierski, Garrett Fields, Matthew Valderrama, Elijah Darby, and Mariano Del Rosso. In addition to having gained excellent research peers, I am grateful to have made amazing life-long friends at the Choo group.

Throughout this stint, I have had the good fortune of having great collaborators to help me add to my findings and produce a great research story. In this regard, I would like to thank Dr. Sriram Vijayan, Dr. Meiyue Shao and Prof. Joerg Jinschek (now at DTU, Denmark) from The Ohio State University for help with the microstructural characterization of Ti-6Al-4V melt pools. I would also like to thank Dr. Peeyush Nandwana (ORNL) and Dr. Yang Ren (ANL, now at City University of Hong Kong) for their valuable help with the ex-situ characterization paper.

Additionally, I had the privilege of interacting with brilliant scientists who helped me venture into and understand things that were not anywhere near to my prior knowledge base in metallurgy. In this regard, I would like to thank Dr. Stuart Slattery (ORNL), Dr. Narendran Raghavan (LANL), Dr. Sam Reeve (ORNL) and the whole ExaAM / OpenFoam team for interesting discussions on melt pool simulations and their support over the past couple years. I would also like to thank Rongxuan (Raphael) Wang, Dr. David Garcia (now at PNNL), Bo Shen and Prof. Zhenyu (James) Kong from Virginia Tech for our fruitful interactions on simultaneous melt-pool temperature measurements during the in-situ experiments. A special mention to Dr. Vijayan and Dr. Raghavan for being great sounding boards for my research ideas and for great advice in professional and personal matters.

I am grateful to have been a part of the Multi-University Research Initiative (MURI) Program led by Prof. Suresh Babu and having the unique opportunity to collaborate with an interesting and hardworking group of PIs and students from several universities across the US and Australia. I would like to acknowledge the Office of Naval Research (Award #N00014-18-1-2794) for funding my research work. I am confident that all the skills I learnt along this journey will serve me well in the years to come in my research career.

I would like to thank my friends Prachi, Jerome, Dony, Yadu, Lakshmi, Hasitha, Eureka, Kaustubh, Indrani, Sai Bachu, Anwesha (and everyone from the IISc M.E group), Anirudh Srinivas, Aditya Srinivasan, Sandeep, Pranav and Vijay for all the great times together and their unending patience and support throughout this journey.

Finally, I am most grateful to my parents, Rekha and Rajaram Kamath for being my most fierce cheerleaders during this journey. I owe all the great opportunities that I was able to experience along my journey to their hard work and sacrifices they made for my sake all these years. Thank you, Amma and Annu - I promise to honor all you did for me by giving my best to in the opportunities to come.

ABSTRACT

The overarching goal of this dissertation is to better understand the underlying process-structure relationships in play during the implementation of a spot melt strategy for metal additive manufacturing, which has become a popular alternative to the conventional raster melt strategy for site-specific microstructure control. In the first part of this dissertation, the effect of a spot melt strategy on the solidification texture, variant selection, phase fraction, and their variations along the build height of an E-PBF Ti-6Al-4V is investigated in comparison to a conventional linear melt strategy using high-energy synchrotron x-ray diffraction. In spite of the thermal excursions involved, the α [alpha] phase exhibit a Burgers orientation relationship (BOR) with the parent β [beta] phase for both melt strategies. Overall, the novel spot melt strategy produces a more homogeneous microstructure in terms of both the phase fraction and texture across the build height.

Motivated by these findings, the second part of this dissertation tries to understand the fundamentals of microstructure formation in laser spot melts (on Ti-6Al-4V alloy, as a function of laser power) by probing the transient evolution of melt pool dimensions and solid-liquid interface velocity using a rapid (μm-μs resolution) in-situ, dynamic synchrotron x-ray radiography (DXR) and post-mortem EBSD. Solidification kinetics was observed to follow three stages (with a prominent steady state) in both the conduction and keyhole mode. Further, the steady-state solidification velocity was found to decrease with increasing laser power. Finally, physical processes operational during the melting and solidification events are ascertained using dimensional analysis and their bearing on solidification microstructure is discussed.

In the last part of this dissertation, the conversion of radiography images of a spot melting event to density maps (using Beer-Lambert's law as the physical basis) and further, to transient sub-surface temperature evolution is demonstrated. In summary, a deeper understanding of the

fundamental processes behind the spot melt strategy has been achieved in this work through experimental means such as in-situ radiography, ex-situ diffraction, and post-mortem EBSD. This understanding to serve as a basis to validate existing and improve spot melt pool models and help AM process design.

TABLE OF CONTENTS

LIST OF TABLES

LIST OF FIGURES

Chapter 1
Introduction

1.1. Background

Additive manufacturing (AM), commonly known as 3-D printing, is a novel technology developed a little over 30 years ago. Since, AM involves additively depositing the raw material layer-by-layer and further consolidation by melting or solid state joining, a considerable increase in material waste is avoided compared to that in conventional subtractive manufacturing processes, such as machining. The ability to build components with complex geometries otherwise inaccessible or cost ineffective using conventional manufacturing processes is another significant advantage of the AM process.

Metal additive manufacturing (AM) techniques are classified on the basis of feedstock type and mode of energy input for consolidation. Common energy input sources include laser beam, electron beam and ultrasound; with powder, wire and sheets being the most common type of feedstocks [1]. The most conventional heat sources used are laser and electron beam, and the layer-by-layer deposition is carried out in a raster fashion. The commercially available materials built using AM techniques include Ti alloys, Ni alloys and steels [2-5]. Ti-6Al-4V, the workhorse alloy of the aerospace industry, is one among the most studied alloys in the context of metal AM [6]. In spite of the numerous advantages of the AM process, one of the key issues hindering precise microstructure control is the thermal cycling of the sub-surface layers due to the layer being deposited and the heat buildup in the sub-surface layers affecting the build layer. The capability to tailor the grain and defect structure of the final product is critical in realizing the full potential of AM technologies.

With regard to fusion-based metal AM techniques, a fundamental knowledge of the ensuing phase transformations (vapor-liquid, liquid-solid and solid-solid) is critical to establish a correlation between AM process parameters and the key physical variables governing the build microstructure [7]. A wealth of fundamental solidification literature points to the thermal gradient across the liquid-solid interface (G) and the velocity of the liquid-solid interface (R), as being the key physical variables in the liquid-to-solid phase transformation. These G-R maps have been traditionally used in welding (and now in AM) research to determine the process parameters to obtain a desired microstructure. One of the popular issues in this field is that of control of grain structure, columnar or equiaxed. Studies by Gaumann et al. [8-10] on epitaxial laser metal forming of Ni superalloys showed that G and R can be used as a basis to obtain processing-microstructure maps with regions of equiaxed grain formation for process parameters such as laser power, scan speed, laser diameter and preheat temperature.

In the context of AM, a conventional raster melt strategy results in the heat accumulation (resulting in low R) and high G usually leads to the formation of a columnar microstructure along most of the build height. The process window, in terms of the laser power and scan speed, to obtain an equiaxed microstructure exists [11] and is mostly narrow, depending on the material. Among the many process parameters that can be used to affect the microstructure, scan strategy has been used recently to increase the equiaxed grain fraction in a predominantly columnar build microstructure [12]. In addition to the wider process space available for the equiaxed transformation, the spot melt strategy can provide a good opportunity to obtain site specific microstructure [13] and needs to be well understood.

The effect of various novel spot melt configurations and their effect on the G and R of the melt pool (and therefore, on the microstructure) has been studied for the case of Ni-superalloys using thermal models [14, 15]. Preliminary studies on the rationalization of observed porosity and

α-microstructure in the novel spot-melt E-PBF Ti-6Al-4V and its comparison with the conventional raster-melt counterpart has been reported by Nandwana and Lee [16]. However, a detailed comparison between the solidification conditions in the above melt strategies in Ti-6Al-4V through the study of solidified β-microstructure and the transformed α-microstructure after the thermal excursions seen in AM is not yet well understood and is key to unlocking the full potential of the spot melt strategy.

The additive manufacturing community has leaned on the wealth of knowledge available on laser and electron-beam welding to answer fundamental questions related to heat and fluid flow in the single melt pool [17] and consequently, to the microstructure development in the AM build [18, 19]. Traditionally, the transient behavior of both the liquid-solid and vapor-liquid during melting and solidification in a welding process has been predicted through numerical simulations using coupled thermal and fluid flow models. While most of the work has been focused on the linear raster type of welds [20-23], significant work has been carried out with regards to spot melting as well [17, 20, 21, 24, 25]. However, the above models are calibrated only using the ex-situ microstructure data (for maximum melt pool size) and make assumptions ignoring certain physics in model, which is again not uniform across the modelling studies. Therefore, transient melt pool evolution data from in-situ laser melting experiments is essential in informing these models to obtain high-fidelity simulations which can be further used to better perform part-scale AM simulations.

1.2. Key scientific questions

With an aim to address the issues raised above, this thesis will be focusing on the following specific questions/goals under three themes:

1) Exploration of differences in microstructure between the novel spot-melt and conventional raster-melt built Ti-6Al-4V

(i) Does the crystallographic texture and phase fraction vary as a function of scan strategy and build height?

(ii) Does the Burgers Orientation Relationship (BOR) between the β and α phases sustain through the thermal excursions around the β-transus experienced during the build process?

(iii) Is there a preferred set(s) of α-variants observed in the build microstructure?

2) In-depth parametric study of the transient evolution of laser spot melt in Ti-6Al-4V alloy

(i) How does a single laser spot evolve spatially and temporally in terms of dimensions and velocity of the melt pool and vapor cavity?

(ii) How do key characteristics of spot melting dynamics and solidification kinetics as change as a function of laser power?

(iii) Do the solidification microstructures in conduction and keyhole mode melt pools correlate well with the measured transient melt pool evolution data?

3) Physics-based approach to obtain transient temperature evolution based on in-situ radiographs of spot melting event

(i) Can we convert a time series of radiographs depicting spot melting into density maps using the Beer-Lambert's law as the physical basis?

(ii) Can we further extract useful sub-surface temperature distribution and its transient evolution in and around the melt pool by converting the above density map into a temperature map?

1.3. Thesis structure

This dissertation consists of 6 chapters. Following the introduction, **Chapter 2** provides a literature review and discusses the gaps in the current state of knowledge on metal additive manufacturing, physical metallurgy of Ti-6Al-4V alloy, melt pool dynamics and solidification kinetics. **Chapter 3** discusses the difference in crystallographic texture and phase fractions of the α- and β-phases between the E-PBF Ti-6Al-4V built using spot-melt and raster-melt strategies. With an aim to obtain a deeper understanding of the physical processes occurring in the spot melt strategy, **Chapter 4** focuses on the melt pool dynamics and solidification kinetics in a single laser-spot-induced melt pool and investigates the effect of laser power on them. **Chapter 5** demonstrates the feasibility and details the workflow to convert the radiography images into density and temperature maps using Beer-Lambert's law. Finally, **Chapters 6 and 7** summarize this dissertation, provide guidelines relevant to the spot melt strategy for AM, and outline suggestions for future work.

Chapter 2
Literature Review

2.1. Metal Additive Manufacturing

2.1.1. Description and classification of metal AM processes

Additive manufacturing (AM) processes use a bottom-up approach to build components via a layer-by-layer addition of material while being guided by a 3-D CAD model. The most prominent advantage of this technique is a significant reduction in material waste is avoided compared to that in conventional subtractive manufacturing processes, such as machining. Additionally, the ability to build components with complex geometries otherwise inaccessible or cost ineffective using conventional manufacturing processes. A significant reduction in lead times can be achieved by reducing the part count and eliminating/decreasing the part assembly times. Keeping these advantages in mind, AM is now accepted as an effective route to produce custom-made, high-performance components for demanding applications in aerospace and medical industries.

Based on the ASTM standard [26], metal additive manufacturing (AM) techniques are classified on the basis of feedstock type and mode of energy input for consolidation. Common energy sources include laser beam, electron beam and ultrasound; with powder, wire and sheets being the most common type of feedstock [3]. In powder-bed fusion processes, the energy source is used to fuse selective areas on the powder bed, resulting in melting and solidification of the melt tracks. The part is built on a substrate which serves as mechanical support and thermal sink in the process. A layer-by-layer deposition is achieved by lowering the Z-axis of the stage after each layer is built. Although the build volume is quite low (of the order of 0.1 m^3) [27], a large amount of powder is used in both the process. The laser powder-bed fusion (L-PBF) system uses

a laser heat source (in tandem with galvanometer driven scanning mirrors) in an inert chamber, while the electron powder-bed fusion (E-PBF) system uses an electron beam heat source (in tandem with electromagnetic lenses) in a vacuum build chamber. Additionally, in the E-PBF system, a pre-heat/sintering step [1, 6] is performed prior to the fusion step to avoid charging and consequent repulsion of the powder. Also, the laser beam diameter range (20-100 μm) used is generally lower than the electron beam diameter (100-200 μm). This results in lower powder size ranges, layer thickness, input powers and surface roughness in the L-PBF compared to E-PBF. A schematic of an Arcam EBM (now a product of GE Additive) E-PBF system is shown in Fig. 2.1.

2.1.2. Process-structure-property relationships in AM Ti-6Al-4V alloy

The commercially available materials built using AM techniques include Ti alloys, Ni alloys and steels [2-5]. Among the Ti-alloys manufactured using AM, Ti-6Al-4V alloy has been studied the most due to its high strength-to-weight ratio and corrosion resistance. Ti-6Al-4V alloy (Ti-64) is a dual-phase titanium alloy commonly used in the aerospace, chemical, and biomedical industries.

The processing-microstructure relationships have been studied extensively for the AM Ti-64 manufactured using PBF and DED systems. The characteristics of the key microstructural features in Ti-64, i.e. β-grains and α-laths, are seen to be heavily dependent on the process parameters. Most AM (laser and e-beam) built Ti-64 were seen to solidify as elongated columnar β-grains with their major axis and the crystallographic <100> direction nearest to the heat transfer direction [18, 28, 29]. Further, the solidified prior β-grains in E-PBF built Ti-64 alloy [18] was shown to transform into a diffusional (α+β) on cooling, in contrast with the L-PBF [28] microstructure consisting of mostly α'-laths formed via a diffusionless transformation due to the higher cooling rates encountered in the latter process route.

Brandl et al. [30] reported that an increase in laser power, decrease in scan speed and/or increase in wire feed rate result in an increase in the size of the prior β-grains and, β- and α-laths (in the low-temperature basketweave structure) in a wire-fed, laser DED built Ti-6Al-4V. They attributed the observation of larger feature sizes to an increased heat input resulting in a decrease in thermal gradients and cooling rates and consequently, reducing the solidification rate. A similar rationale was used to justify observations made by Kobryn and Semiatin [29] wherein a change in α-morphology was seen in the low-temperature microstructure from mostly fine Widmanstätten in deposits made using Nd:YAG laser to mostly coarse Widmanstätten with grain-boundary α in deposits made using a CO_2 laser. A significant increase in the α-lath and colony sizes in E-PBF Ti64 built using a relatively higher preheat temperature of 700°C was reported by Al-Bermani et al. [18]. Antonysamy et al. [31] showed that a change in build geometry from a thick to thin cross-section changes the solidified β-grains from a coarse, straight columnar shape to a fine, curved columnar shape. This was attributed to powder nucleation being the dominant mechanism in the thin sections, whereas growth from previously grown layers being a key determinant in the microstructure formation of thick sections. A similar reasoning was used to justify the microstructure differences produced using a contour pass vs in-fill hatching [31].

Studies on post-build annealing treatments on E-PBF Ti-64 by Galarraga et al. [32] showed that sub-transus (below β-transus, i.e. T < 1000 °C) annealing results in a coarsened α-microstructure in depending on the time and temperature of the treatment. A similar observation was made by Al-Bermani et al. [18] while a hot-isostatic pressing (HIP) treatment was applied to E-PBF Ti-64. Subsequently, super-transus solutionizing treatments [33, 34] have been observed to result in the transformation of build columnar β-grains to an equiaxed shape and the pre-quench equiaxed β-grain size is found to be proportional to the super-transus holding times. However, the final properties of the E-PBF build are seen to be dependent on the combined effect

of cooling rate, post-quench aging hold times and extent of change in final α-texture (through super-transus β-grain rotation) than the pre-quench equiaxed β-grain size.

In addition to their effect on the build microstructure, the process parameters are shown to play an important role in determining the defect propensity, type (keyhole, gas pore, lack of fusion) and characteristics (location, size, shape) [35-38] in AM Ti64. Several studies have been performed to study the combined effect of key process parameters (laser power, scan speed, layer thickness) on microstructural and defect structure characteristics in AM Ti64 using combined variables such as linear energy density [28, 29] and volumetric energy density [35]. Research in this direction has yielded useful process maps to act as a guide during industrial production of AM Ti64 allowing for the optimization of microstructural features (grain morphology and size) [39] while producing a defect-free build [36]. On the topic of process-property relationships, all the aforementioned process variables in AM Ti64 builds resulting in a coarser α-laths have been shown to display a lower yield strength and hardness with a simultaneous decrease in ductility [18, 28-30, 32, 33, 40]. The yield strength of AM Ti64 build was also observed to increase with increase in oxygen content due to oxygen pickup from the process atmosphere in L-PBF [41] and due to oxygen excess from power reuse in E-PBF [42, 43]. In their review article, Chern et al. [44] have reported the fatigue properties to be highly dependent on direction of loading w.r.t build direction (due to the long direction of the α-laths and defects [45]) and surface roughness and, weakly dependent on post-treatment (HIP vs no-HIP [46]).

2.1.3. Melt strategy – An important process variable

In addition to the above process variables, it has been reported that one of the key processing variables to achieve microstructural changes in AM builds is the melt strategy. Carter et al. [47] found that changing the melt strategy from a bi-directional (“back-and-forth”) to an

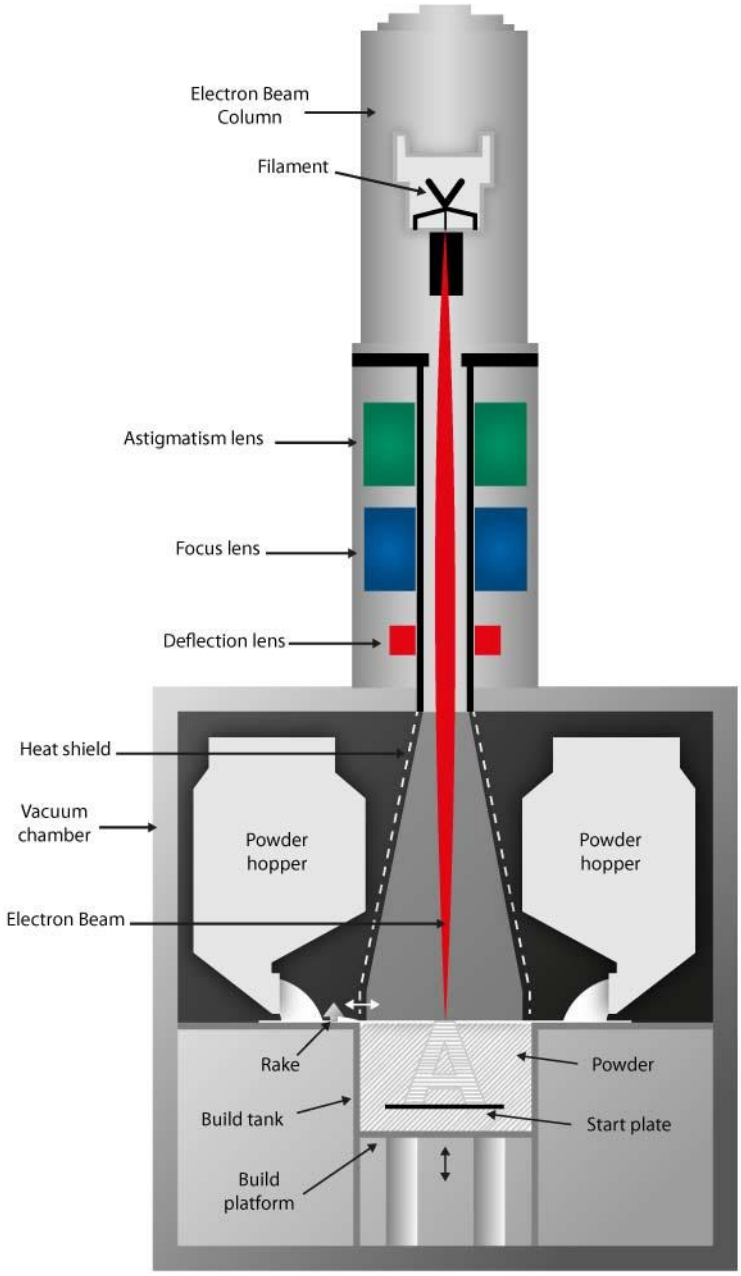

Figure 2.1. Schematic of an Arcam EBM E-PBF system [48].

"island" raster pattern resulted in a change in the crystallographic texture from a unimodal to a bimodal cube texture in L-PBF CM247LC. Helmer et al. [11] showed different amounts of equiaxed and columnar grains (and consequently, texture) can be obtained by using slightly different types of the bi-directional ("cross-snake") raster scan in E-PBF IN718 builds. Also, Tammas-Williams et al. [49] compared the porosity distributions by modifying the amounts of in-fill and contour rastering in E-PBF Ti-6Al-4V and found that most of the porosity was present in the in-fill region. Arısoy et al. [50] performed an optimization study on the laser process parameters for two layer-to-layer scan rotations (90° and 67°) in L-PBF IN625 and found that the scan rotation of 67° diminished the effect of the laser process parameters on the growth direction and resulted in finer grain sizes compared to the 90° rotation. In contrast, while majority of studies have focused on different variants of the linear raster-melt strategy, Dehoff et. al. [12] applied a spot-melt strategy on an E-PBF IN718 and demonstrated an effective manipulation of the grain size, orientation, and the morphology from columnar to equiaxed. Subsequently, Raghavan et. al. [15] investigated the relative importance of various process parameters involved in the spot-melt strategy to identify an optimal conditions to achieve a higher equiaxed grain fraction in the IN718 builds. Recent work by Nandwana and Lee [16] compares the build microstructure and porosity observed in E-PBF Ti-64 builds manufactured using a spot-melt strategy with the ones built using a conventional raster strategy. Using melt-pool simulations and EBSD characterization, the authors pointed out the importance of melt pool characteristics (size, shape, and cooling rate) on the resulting microstructure. Also, melt-pool simulations using a semi-analytical heat conduction model by Plotkowski et al. [51] showed that the melt-pool size and shape (and consequently, solidification velocity and thermal gradient) are strongly dependent on the melt strategy, process parameters, and thermal properties of the material being built. (*A version of this section (2.1.3.) was originally published in "Additive Manufacturing" by R.R. Kamath et al.* [52].)

2.2. Physical metallurgy of Ti-6Al-4V

2.2.1. Phases, crystallography and transformations

Commercially pure titanium (CP-Ti) can exist in one of two allotropic forms depending on its temperature – hexagonal close packed (α-HCP) structure from room temperature up to 882°C and body-centered cubic (β-BCC) structure above 882°C. The transformation temperature from α-HCP to β-BCC is called the "β-transus" temperature (882°C for CP-Ti). The β-transus can be altered by the addition of various alloying elements. These alloying elements can be divided into three categories - α stabilizers (Al, O, C, N, Ga, Ge, B) which raise the β-transus, β stabilizers (Isomorphous - V, Mo, Ta, Nb; Eutectoid – Fe, Cr, Cu, H) which lower the β-transus and neutral elements (Zr, Hf, Sn) which do not result in a significant change in the β-transus [53]. Depending on the relative amount of α- and β-stabilizers present in the given alloy, titanium alloys can be divided into three types: α alloys, β alloys and (α + β) alloys. A schematic phase diagram is shown in Fig. 2.2a [54].

A schematic of the α-HCP and β-BCC crystal structures in pure-Ti with the lattice parameters (and most densely packed planes shaded), at room temperature and 900°C respectively, is shown in Fig. 2.2b. The c/a ratio for the α-HCP structure in pure-Ti, calculated from the lattice parameters in Fig. 2.2b [53], is about 1.587 and is lower than the ideal c/a ratio for HCP crystal structures (i.e. 1.633). It should be noted that in addition to a change in temperature, the lattice parameter values shown can change based on alloying content [55]. The solid-solid phase transformation from α-HCP to β-BCC has been observed to follow a Burgers' orientation relationship (BOR) in most cases of both diffusional and displacive transformations. According to the BOR, the close-packed planes and directions in both the parent and child phase

tend to align with each other, i.e. the following relationship holds – β {110} || α {0002} and β <222> || α <11$\bar{2}$0> [56]. This relationship is graphically illustrated in Fig. 2.2c [57].

Ti-6Al-4V (wt%, Ti-64), the alloy system used for the studies presented in this dissertation, is an (α + β) alloy, since it's microstructure can consist of both the α-HCP and β-BCC phases at room temperature. The amounts and microstructural morphologies of the phases are highly dependent on the processing method and conditions. The (α + β) microstructure can be completely transformed into a fully-β microstructure on heating above the β-transus temperature. The β-transus for Ti-64 about 1000°C and is seen to be sensitive to the alloy composition [55]. On cooling below the β-transus temperature, the β-phase is seen to transforms into one of the many α-morphologies depending on the cooling rate. A martensitic α′ (with relatively low amount of retained β) is seen to form via a diffusionless pathway when subjected to high-cooling rates (> 410 K/s) [58]. The M_s (martensite start) temperatures are reported to be in the range of 600 - 850°C and, are observed to increase with increasing amounts of α-stabilizers and decrease with increasing amounts of β-stabilizers. [58]. On the other hand, when subject to lower cooling rates (< 20 K/s), a diffusional transformation of the β microstructure results in the formation of allotriomorphic α which nucleate on the β grain boundaries, followed by growth on the already-formed α layer. Further cooling in this system results in the formation of one of two configurations of α microstructure - colony/lamellar or Widmanstätten/basket-weave. An α-colony microstructure is formed when the α plates are aligned parallel to each other interspersed with β ribs. A Widmanstätten morphology is formed when new α-colonies grown perpendicular (to minimize strain energy) to existing colonies forming basket-weave-like structure. Example microstructures depicting these morphologies are shown in Fig. 2.3a,b [59].

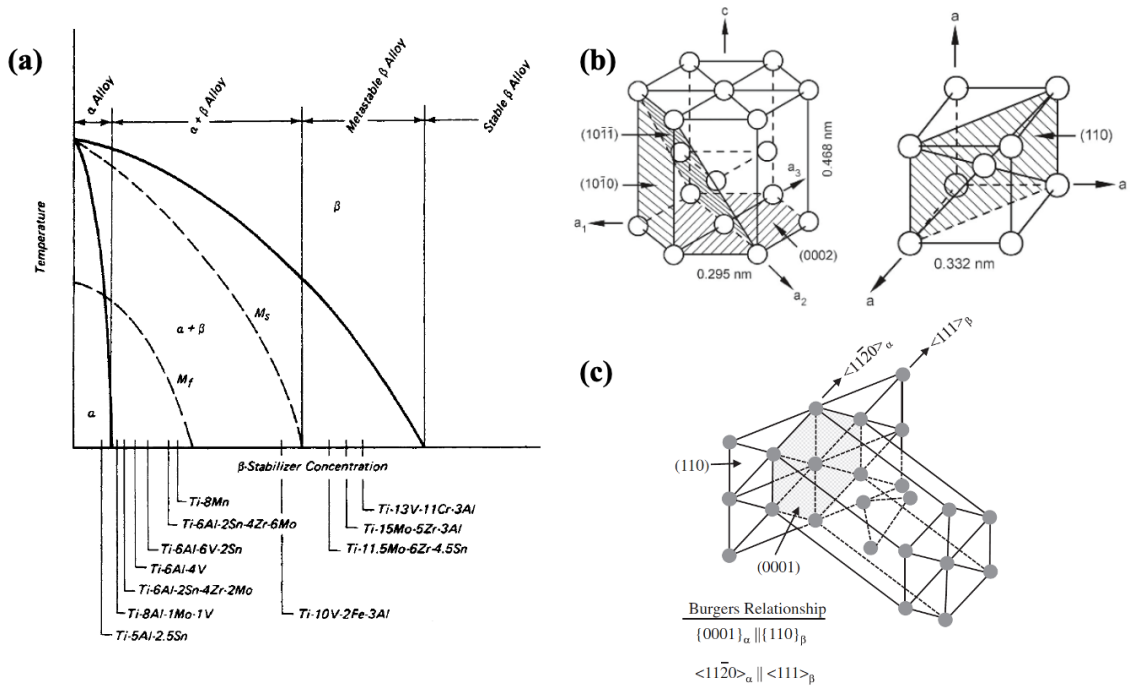

Figure 2.2. Schematics of the (a) pseudo-binary titanium (and α stabilizer) phase diagram showing the different categories of Ti-alloys, adapted from [54], (b) α-HCP and β-BCC unit cells for pure Ti with approximate values of the lattice parameters labelled, adapted from [53], (c) Burgers' orientation relationship between BCC and HCP phases, adapted from [57].

A massive transformed α phase has also been reported in microstructures subject to medium cooling rates (20 - 410 K/s).

Elmer et al. [55] reported an equilibrium β-phase fraction of 4 wt.% calculated using a pseudo-binary phase diagram of a Ti-6Al and V. The β-phase fractions in Ti-64 are reported to range from 0-10wt% depending on the processing route [55, 60-65]. Most linear-fill L-PBF builds consist of a fully α' martensitic structure with almost no β in their as-built condition due to a relatively higher cooling rate involved during the processing without an active substrate pre-heating. However, an increase in the β fraction is often observed when the L-PBF builds are subjected to an annealing treatment [63, 64]. In the case of linear-fill E-PBF Ti-64, the β fraction ranges from 1 to 5 wt.% even in the as-built condition [60-62, 65] in spite of the cooling rate still being orders of magnitude higher than that necessary for the α' martensite formation (410 K/s [58]). Explanations for this observation have been provided by Tan et al. [60, 65] using a diffusional mechanism and by Sridharan et al. [66] based on a shear-based mechanism of transformation from α' to (α + β).

2.2.2. Crystallographic texture and variant selection

The α and β texture of the room temperature microstructure have been reported to depend on the processing route and temperature [67, 68] (Fig. 2.3c). Since the c/a ratio of Ti-6Al-4V is lower than 1.633, the deformation through the prismatic and basal planes are seen to play an important role in determining the product textures [67]. The α-texture in as-built AM Ti-64 has been observed to follow the β-solidification texture in raster-filled L-PBF [69], E-PBF [18, 31, 70-72] and DED [73]. These studies report a {100}-type cube texture along the build direction in the solidified β and consequent α-texture following the BOR during transformation [18] (Fig. 2.4).

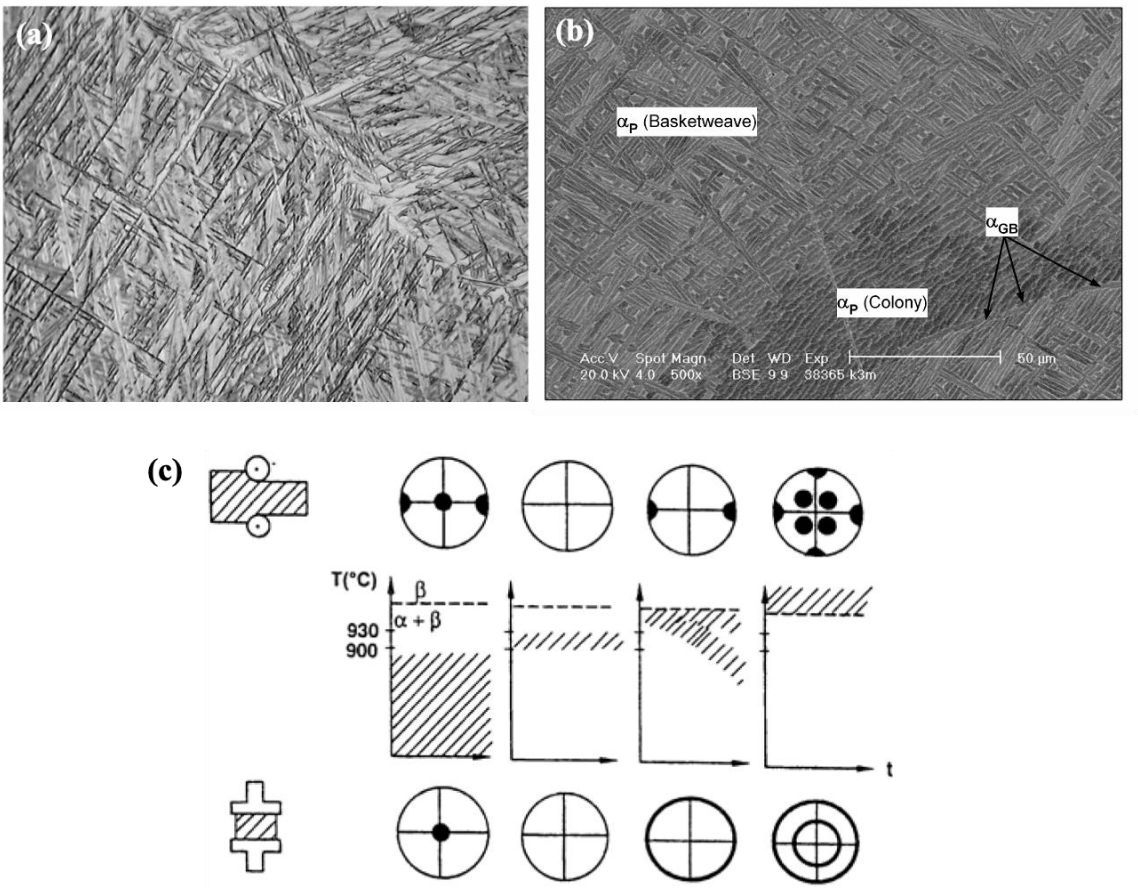

Figure 2.3. Example micrographs of different α morphologies formed in Ti-6Al-4V subject to (a) high cooling rate (acicular α), (b) low cooling rate (grain-boundary/allotriomorphic α, colony α, basket-weave/ Widmanstätten α), adapted from [59]; (c) α basal (0002) texture observed for different rolling and axisymmetric compression in different phase fields, adapted from [68].

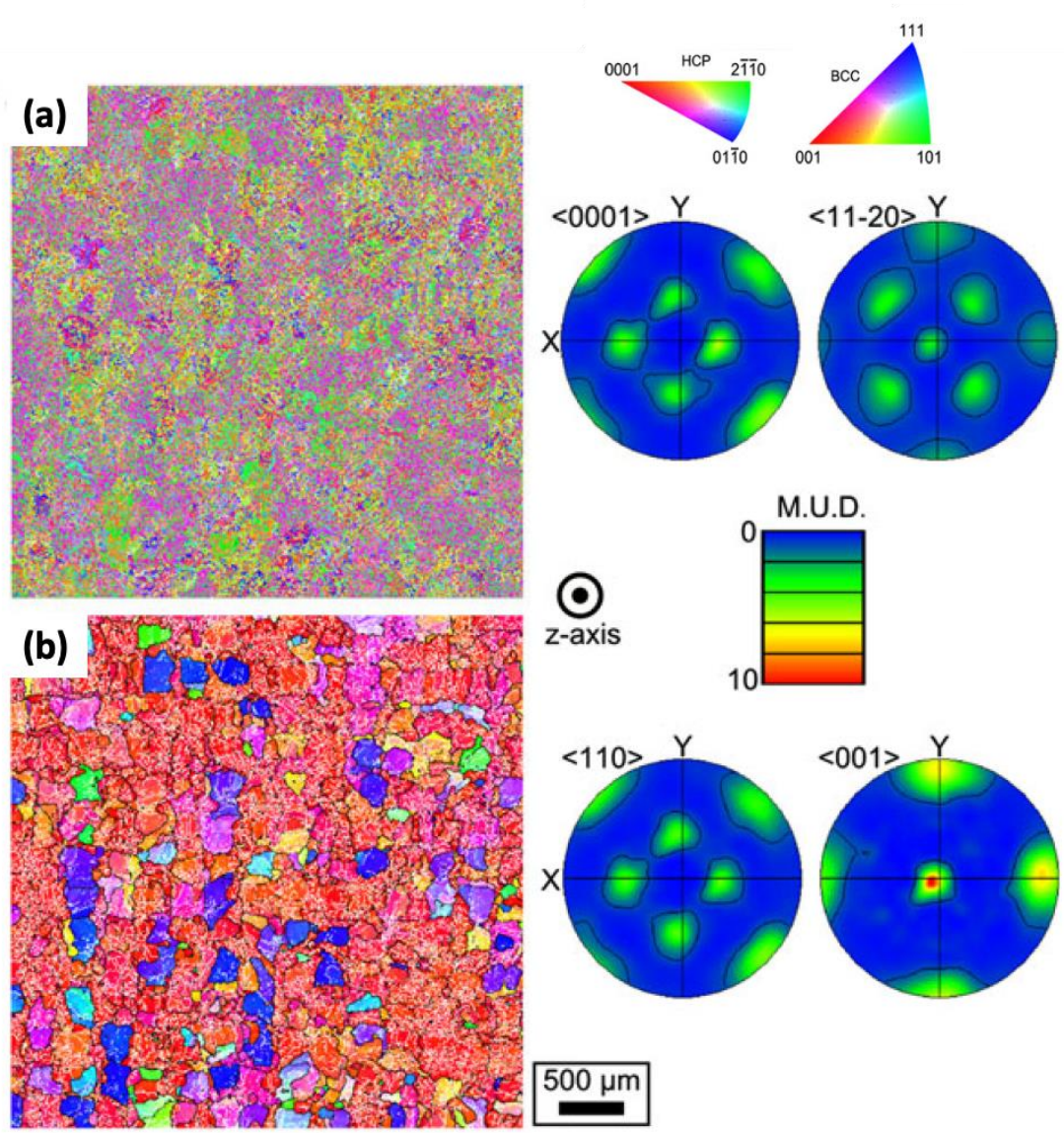

Figure 2.4. IPF-Z and pole figures for an E-PBF Ti-6Al-4V along the build plane showing (a) α microstructure, (b) reconstructed β microstructure, adapted from [18]. Note that Z-axis is parallel to the build direction. The β (100) pole figure shows a solidification cube texture.

This observation is justified by Wei et al. [19] wherein, it was shown that the easy growth direction (which is of the <100> type for cubic systems) aligns with the direction of the maximum thermal gradient at the liquid-solid interface during the solidification of a melt pool.

Fundamental in-situ heating/cooling studies on wrought Ti-64 alloy by Bhattacharyya et al. [74], Lonardelli et al. [75], and Obasi et al. [76] concluded that, on heating, the α-to-β transformation occurs by the growth of the pre-existing/retained β, as opposed to the nucleation of new β. This "texture memory effect", often observed in thermo-mechanically processed Ti-64 alloys [74-76]. These studies also reported the possibility of grain growth in the β field and the consequent production of new α' variants, thus resulting in an appearance of new texture components.

As described before, the α-to-β transformation results in the formation of multiple α-variants. A high-angle grain boundary (HAGB) is formed when two α laths with different orientations are formed adjoining each other in a prior β grain. Wang et al. [77] mathematically proved that out of the 144 possible combinations of α/α lath boundaries that can form only 5 distinct types of α/α HAGB exist, due to crystallographic considerations. Additionally, in their study on a pure Ti sample [77], they determined that Type 2 and Type 4 HAGBs occur more frequently than the others and attributed it the 'self-accommodation' of strain energy during to the formation of α' through the formation of three variant clusters. Lonardelli et al. [75] reported that during the α-to-β transformation, variant selection is more pronounced in CP-Ti than in Ti-6Al-4V alloy, due to the absence of preexisting β phase. Moustahfid et al. [78] reported that during the β-to-α transformation in a Ti-64 sheet after β treatment showed weak or no variant selection, whereas, after a heat treatment in the α+β phase field, variant selection is observed. Gey et al. [79] and Zhu et al. [80] concluded that heavy cold-rolling before an α-β-α transformation sequence results in sharpening of inherited a texture in Ti-64 and CP-Ti sheets, therefore,

suggesting variant selection. Variant selection has also been observed in Ti-64 hot-rolled in the β field in the study by Gey et al. [81]. The key variables which affect the extent of variant selection during the β-to-α transformation in Ti-64 (and CP-Ti) are the characteristics of the high-temperature β phase (β grain size [76, 82] and β texture [79]) and, heat treatment parameters (type of treatment [78, 81], rolling temperature [83], amount of cold/hot work [79, 80] and cooling rate [57]).

A few mechanisms proposed to explain the above observations are as follows [57]:

(i) Residual stress in the high temperature β phase due to change in volume on heating and/or externally applied stresses might prefer certain variants.

(ii) Defect structure of the deformed β phase might aid in the nucleation of selected variants.

(iii) Preferred nucleation due to presence of metastable α at high temperature.

(iv) Selection of variants which best accommodate the transformation-induced strains.

(v) Neighboring grains with common or slightly misaligned (110) poles favor the nucleation of specific variants [84].

Crystallographic texture plays an important role in determining the tensile [85, 86], fatigue [86-88], fracture [89], and corrosion [90] behavior of Ti-6Al-4V components. For example, the preferred alignment of basal (0002) planes perpendicular to the loading axis results in higher tensile strength, fatigue strength, and fracture toughness [85-87, 89]. On the other hand, the corrosion and tribo-corrosion resistance [90] has been observed to reduce when the (0002) planes are parallel to the corrosion surface. Therefore, detailed studies on the role of processing variables in the crystallographic texture development and its distribution in AM builds is essential.

2.3. Melt pool dynamics and solidification kinetics

2.3.1. Overview

As alluded to in previous sections, fusion-based welding and additive manufacturing processes can be classified based on the nature of heat source used [7].The most common heat sources used are electric arc, laser and electron beam. Depending on the heat source and the material being processed, a fraction of the incident energy is used to form a melt pool of the material. The remaining fraction of the incident energy is dissipated via various routes - conduction through the solid, convection due to melt flow and radiation from the top of the melt pool. In the case of laser and electron beams, there is a high propensity for the material to develop a vapor cavity (keyhole) due to localized, excessive evaporation caused by the high-energy density of the heat source. During melting in laser spot welds [7], it has been seen that as the input energy exceeds a certain limit, the surface tension pressure on the top surface of the melt pool is overwhelmed by the recoil pressure due to excessive vaporization and results in the formation of a vapor cavity. In this high-energy density input regime, the melt pool is said to exhibit a “keyhole” mode melting, whereas in the low-energy density input regime it is said to exist in a “conduction” mode. Ideally, AM process parameters are designed to stay in the conduction region to avoid possibility of pore retention after keyhole collapse. The criterion put forward by King et al. [91] is one of most widely used design parameter to estimate the conduction-to-keyhole transition. This criterion uses a material-dependent threshold value of the ratio of absorbed energy density to melting enthalpy to mark the transition.

The dynamics of the melt pool and the vapor cavity are dependent on the complex interactions between surface tension, recoil and hydrostatic pressures acting on them [92-94]. A schematic of the forces is shown in Fig. 2.5a [95]. The combined effect of these forces determines the size and shape of the melt pool and vapor cavity and their rate of increase or decrease at any

instant during the melting process. The melt pool flow is determined by the interplay between the buoyancy, surface tension gradient and viscosity forces (also electromagnetic/Lorentz force, in the case of arc and electron beam sources). As opposed to raster welds, spot welds do not exhibit a “steady-state” during melting. Additionally, spot welds are seen to solidify with a higher cooling rate, thus, leading to a higher propensity for non-equilibrium phase formation and solidification cracking [96]. The solidification kinetics (and therefore, the microstructure) in the raster weld case (Fig. 2.5b) [97] is dependent on the angle of the solidification front w.r.t the welding direction and the (constant) velocity of the heat source. However, in the spot-melt case, the solidification kinetics depends only on the angle w.r.t. the heat source [17, 20, 21, 24].

Traditionally, the transient behavior of both the liquid-solid and vapor-liquid interfaces during melting and solidification in a welding process has been predicted through numerical simulations using coupled thermal and fluid flow models. While most of the work has been focused on the linear raster melting [20-23], significant work has also been carried out with regards to spot melting as well [17, 20, 21, 24, 25]. A detailed review of the theoretical, modelling and simulation studies describing the above-mentioned physical phenomena in the context of a spot-laser heat source is provided in the following sections. Further, both the legacy and state-of-the-art experimental studies on the subject are described in a later section (2.4.2).

2.3.2. Dynamics during the melting stage

As noted in the previous section, the melt pool and vapor cavity dynamics depend on the balance between the surface tension, recoil, and hydrostatic pressures. The recoil pressure arises from the recoil force on the vapor-liquid interface when the evaporated atoms are ejected from the interface. The recoil pressure is directly proportional to the vapor pressure of the element in the vapor cavity and is therefore proportional to the temperature of the liquid-vapor interface

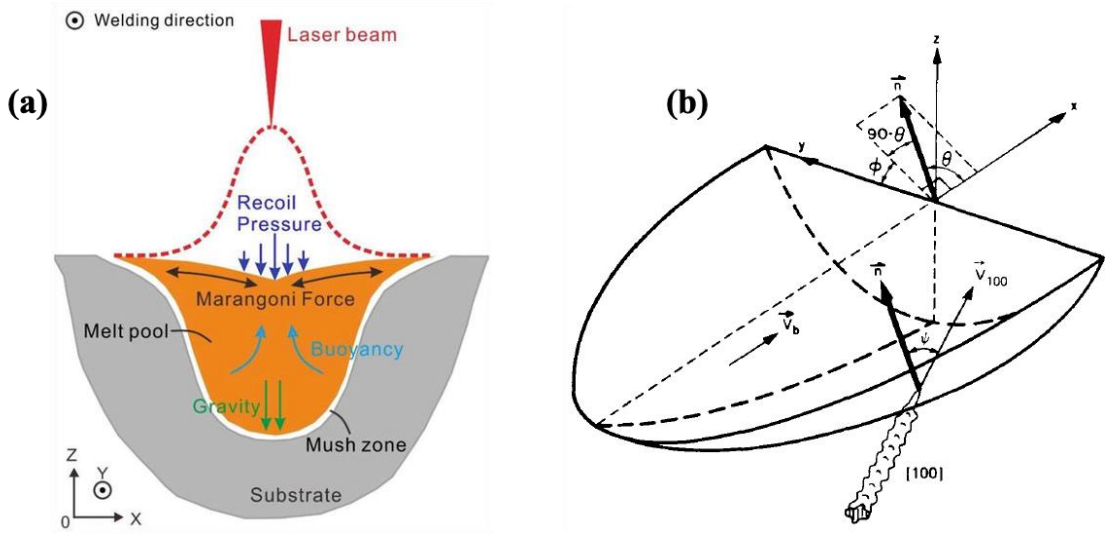

Figure 2.5. Schematic of (a) forces which dictate melt pool and vapor cavity dynamics, adapted from [95], (b) trailing end of a raster weld pool showing the relationship between the solidification normal (n) and the reference frame (x-y-z), adapted from [97].

[92]. The surface tension pressure arises from the surface tension force which tends to minimize the liquid surface. These modelling studies use the final melt pool dimensions to calibrate for the heat source term and simulate the transient dynamics. However, pioneering experimental studies (described in a later section) by Matsunawa et al. [94, 98, 99] and recent studies by Rollett et al. [23, 100-103] have enabled the measurement of the transient nature of the vapor cavity (and melt pool, to a lesser extent) through x-ray radiography to better inform the modelling efforts.

2.3.3. Fluid flow and heat transfer during melting

In the case of conduction-mode laser spot melting, there are two likely causes driving fluid flow in the melt pool against the viscosity of the molten liquid – surface tension gradient and buoyancy. The flow due to surface tension (also called the Marangoni flow) is caused due to the surface tension gradient resulting from the high temperature gradient on the surface of the melt pool. The surface tension has also observed to be very sensitive to concentration of surface-active elements/impurities [104, 105]. The buoyancy driving force is a result of the pressure differential occurring due to spatial changes in the temperature dependent density in the melt pool. In the case of arc/electron-beam welding, an electromagnetic (Lorentz) force might also contribute to the melt pool flow. The relative contributions of the above driving forces to the fluid flow are estimated using dimensionless numbers – Grashof number (buoyancy vs viscous force), Surface-tension Reynolds number (surface tension vs viscous force) and magnetic Reynolds number (electromagnetic force vs viscous force) [20, 21, 24, 106]. On the other hand, studies on the simulation of keyhole mode melting [92, 107] suggest that the evaporation recoil pressure plays a stronger role in liquid metal flow than the surface tension and hydrostatic pressures. Semak and Matsunawa [92] estimated that such flows result in about 70% of the absorbed heat being carried away from the interaction zone.

He et al. [21] point out that as the melt-pool gets larger, the surface-tension driven (Marangoni) flow predominantly drives the liquid metal convection and thus, significantly changes the heat transfer mechanism. The predominance of a particular mechanism for heat transfer is estimated using the Peclet number (Pe) [20, 21, 24, 106]. Pe is a dimensionless number equal to the ratio of heat transferred by convection to that by conduction. In the context of additive manufacturing, Debroy et al. [108, 109] have successfully leveraged these dimensionless numbers to help predict distortion-free, compositionally sound, and well bonded metal AM prints.

2.3.4. Dynamics during the solidification stage

The two key physical variables that dictate the solidification microstructure are thermal gradient (G) at and velocity (R) of the liquid-solid interface. The combined forms of the solidification parameters, (G × R) and (G/R) dictate the size and morphology of the solidified substructure, respectively [110]. The product (G × R, the cooling rate) indicates whether the obtained structure is fine (high G × R) or coarse (low G × R), as can be seen from Fig. 2.6 [111]. The ratio (G/R) however, divides the G-R space into several regions in Fig. 2.6 [111] corresponding to the morphology of the growing solid-liquid interface (Planar, Cellular or Dendritic) and the solidified grain structure (equiaxed or columnar).

The Columnar-to-Equiaxed Transition (CET) phenomena is important to many technological applications where one wants to eliminate equiaxed solidification (e.g. directional solidification of superalloys and epitaxial laser metal forming) or applications where one wants to enhance the equiaxed solidification (e.g. continuous casting, welding and AM parts with near isotropic properties). A transition from columnar to equiaxed growth (CET) is said to take place when nucleation of equiaxed grains takes place in the liquid ahead of the columnar growth front. Hunt [112] developed the first model for the CET phenomenon, which is an analytical relation

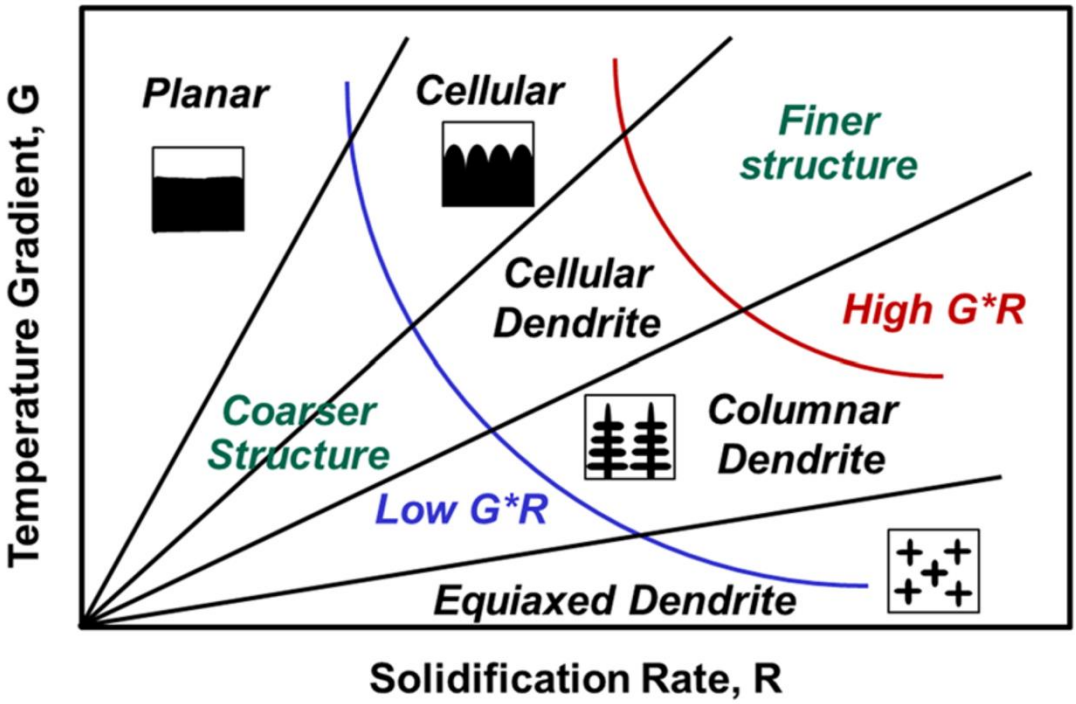

Figure 2.6. A schematic G-R map showing the effect of G × R on solidification substructure (left bottom to right top) and G/R on solidification morphology (left top to right bottom), reproduced from [111].

between G, R and Φ (volume fraction of equiaxed grains). Researchers including Rappaz et. al. and, Gäumann and co-workers [8, 10, 113, 114] extended Hunt's analytical solution for processes with rapid solidification conditions and high thermal gradients, such as welding.

The solidification parameters, G and R, are extracted from temperature-field solutions of coupled heat transfer and fluid flow models [20, 21, 24, 106]. In their work on simulation of spot-welding in steels, He et al. [21] and Zhang et al. [24] report that thermal gradient (G) at the solid-liquid interface decreases and the interface velocity (R) increases as the solidification progresses. Similar trends are seen in spot-melt simulations in IN-718 by Raghavan et al. [15] and Knapp et al. [17]. Katayama and Matsunawa [96] included the effect of latent heat and different microsegregation models and observed that the R follows a three-stage solidification showing an initial increase, steady-state solidification and final sudden increase, in that order. Knapp et al. [17] and Lee [115], found that fluid flow in the single phase liquid region during solidification plays an important role in determining the pool geometry and solidification parameters.

Therefore, given the process parameters and material properties, heat transfer models can be used to extract key thermal variables (G and R) which can be further be input into the said phenomenological models to predict solidification microstructure, enabling microstructure control through process control. Taking advantage of the aforementioned approach, Raghavan et. al. [15, 116] demonstrated the importance of various process parameters and melt strategies in the site-specific control of grain morphology, using an E-PBF setup for an IN718 build. It is noteworthy that in this approach, the accuracy of G and R estimation is entirely dependent on the accuracy of the heat transfer models. To alleviate this shortcoming, in a study evaluating the role of a novel melt strategy on microstructure, Lee et. al. [14] use a similar procedure as Raghavan et. al. [15, 116], with an in-situ temperature measurement during the 3-D printing process from a high-speed infrared camera informing the heat transfer models. The present study uses a different

approach wherein, dynamic in-situ synchrotron X-ray imaging experiments are used to extract R directly and an indirect calculation of the G will be made ex-situ microstructure characterization.

2.4. Characterization tools

2.4.1. Synchrotron high-energy x-ray diffraction

The first objective of the current study is to understand the effect of spot melting on the build texture, orientation relationship, variant selection, phase fraction, and their distribution along the height of an E-PBF Ti-64 alloy build. In particular, high-energy synchrotron x-ray diffraction (S-XRD) technique is used in this work to study the crystallographic texture and phase fraction of the constituent phases in Ti-64, taking advantage of the unique attributes of S-XRD [117-119]. The high-energy x-rays enable a deeper penetration into the sample, allowing for a volume-representative measurement, a spatial mapping, and a full pole coverage during the texture measurement. A scattering volume on the order of 1 mm^3 used in the current study offers sufficient grain statistics for a 3D bulk representative texture measurement, complementing EBSD studies [71, 72, 120, 121] of local grain-to-grain relationships. Moreover, the high angular resolution of S-XRD enables the analysis of a multiphase microstructure such as the Ti-64 alloy, where a small amount of β phase can be resolved for a quantitative analysis of phase fraction and texture. Finally, the low wavelength also allows for the collection of numerous reflections from both BCC and HCP phases providing a better statistical analysis during the Rietveld profile refinement of the diffraction data. (*A version of this section (2.4.1.) was originally published in "Additive Manufacturing" by R.R. Kamath et al.* [52].)

2.4.2. In-situ dynamic synchrotron x-ray radiography

The second objective of the current study is to understand the melt pool dynamics and solidification kinetics of a laser spot melt on Ti-6Al-4V. In recent years, in-situ, dynamic synchrotron x-ray radiography (DXR) has enabled the observation of fundamental physical processes occurring at fine length and time scales in events such as high strain-rate deformation [122] and melting [102]. In the context of additive manufacturing and welding, this ultrafast technique has been leveraged to gain insights into processes such as liquid-to-solid and solid-to-solid phase transformations [102], conduction-to-keyhole transition [100], Marangoni convection [123, 124], pore formation and elimination [125, 126], powder spattering [127], powder spreading [128] and effect of build atmosphere [129] with a variety of metallic systems including Fe- [124, 130], Ti- [100, 102, 126] and Al-alloys [123] being the subject of study. The high x-ray photon flux from the synchrotron, coupled with the high-speed detector, provides excellent spatial and temporal resolution in the order of μm and μs, respectively. This unique advantage of the DXR setup enables us to track rapid solidification events, such as that following laser melting, with the velocities of the order of m/s. The following paragraphs discuss the both the legacy and state-of-the-art experimental studies on melt pool dynamics during laser melting performed using x-ray radiography.

Dynamics during melting stage: Matsunawa, Katayama and co-investigators [99] led pioneering experimental studies on melt pool and keyhole dynamics in-situ during laser welding using x-ray radiography at a temporal resolution of the order of 1-10 kHz. In their studies on pulsed spot and continuous wave laser welding, they were able to capture the instability in the keyhole and proposed that a more dynamic pressure balance model needs to be used for simulating a keyhole (which was implemented by them in [92]).Further, the mechanisms behind pore retention during keyhole collapse [94, 99] were elucidated and leveraged to design a suitable

process to suppress pore formation by wave-form control and change in shielding gas. In a subsequent study on the effect of shielding gases on keyhole dynamics, Katayama et al. [98] found that changing the ambient atmosphere to vacuum greatly decreases the propensity of bubble formation (and therefore, pore retention) while providing a higher depth of penetration during welding in Al-alloys. An extension of this study, performed recently by Calta et al. [129] using state-of-art radiography apparatus with higher temporal resolution (order of 10 kHz), on multiple materials with varying composition and pressure of the process atmospheres showed the high sensitivity of keyhole and melt pool dimensions to temperature- and composition-dependence of the surface tension force.

In their recent spot melting experiments on Ti64, Cunningham et al. [100] were able to capture the keyhole dynamics at a very high temporal resolution (order of 100 kHz) and showed that the critical vapor depression depth for transition from non-fluctuating to a fluctuating keyhole is approximately same for a given beam diameter (irrespective varying laser powers) and has a lower value for a smaller beam diameter. It was also seen that for a given beam diameter, the time taken to reach the critical depth was lower for lower laser powers. They also found that the conduction-to-keyhole transition occurred at a constant power density of around 0.4 MW/cm^2 – which is in line with the traditional welding definition of the order of 0.1 MW/cm^2 for transition to the keyhole regime [7]. Another key step forward in understanding the highly fluctuating nature of the keyhole came through the recent work of Allen et al. (316L SS - [131]) and Simonds et al. (Ti64 - [132]), wherein an integrating sphere radiometry was used, simultaneously with x-ray radiography (order of 100 kHz), to obtain high-speed data (order of 10 MHz) for absorptivity of the sample. They showed that the absorptivity value in the case of a conduction mode melt pool is nearly constant and is relatively lower, whereas it is highly fluctuating and has a higher value for keyhole mode melt pool. It was also shown that the coupling efficiency (absorptivity) increases with increasing laser power [132]. Further, this experimental data was used in tandem

with high-fidelity simulations by Khairallah et al. [133], wherein it was found that fluctuations in absorptivity correlated well with the instabilities in keyhole shape and that pore-generating turbulence is preceded by narrow frequency periodic oscillations. In addition to its fundamental breakthrough, this study showed the potential for the utilization of back-scatter light-based techniques for process monitoring during industrial AM.

Experimental studies on transient changes in melt pool dimensions have been fewer in number compared to the studies on keyhole dynamics. This is partly because studies on raster melting constitute a significantly large part of the literature and for most of the raster melting event, the melt pool exhibits a "steady-state" with near similar dimensions and shape. In their proof-of-concept article for a state-of-the-art radiography measurement setup, Zhao et al. [102] studied the transient dynamics of during spot melting with a higher spatial (order of μm) and temporal (order of 10-100 kHz) resolution, wherein they observed the occurrence of a delay time before melting initiation and a bilinear change in melt pool dimensions with laser dwell time. This dissertation addresses the research gap in the study of transient evolution during by building on Zhao et al.'s [102] work and providing a detailed study on transient melting event as a function of a process parameter (laser power).

Fluid flow during melting: In their seminal work, Matsunawa et al. [99] used tungsten particles (0.1-0.4 mm) to track the fluid flow in a melt pool and found that the flow velocity was in the range of 0.25-0.4 m/s for a raster melt pool in an Al-alloy. Also, Katayama et al. [98] observed a reversal in flow pattern while an ambient vacuum was used during raster melting in an Al-alloy. More recently, the melt pool flow was mapped in a spot TIG melt on steels (with low and high sulphur compositions) using heavy element powders (W and Ti) by Aucott et al. [124] and it was found that inspite of several forces that can drive fluid flow, the surface tension (changed using the sulphur /impurity composition) was a major determinant. They showed that

the flow reversed with the change in composition and the magnitude of the velocity was of the order of 0.1-0.5 m/s. Another recent study by Guo et al. [123] mapped the full-field fluid flow raster melts on Al-alloy substrates (with a powder layer – to more closely mimic AM conditions) via heavy element powders and bubbles ejected from the keyhole. They found that the flow pattern in a conduction mode melt pool is dictated by surface-tension, whereas for a keyhole mode melt pool different driving forces were responsible at different locations (e.g. surface tension force in the hotter regions, forces due to vaporization along the keyhole walls etc.). They also found that the flow velocities ranged from 0.1-5 m/s maximum and average flow velocity decreased with increasing distance from the keyhole.

Dynamics during solidification stage: Experimental studies on transient changes in melt pool dimensions during solidification have been fewer in number compared to the counterpart studies on transient evolution during melting. In their study on laser spot melting, Zhao et al. [102] found that solidification of a spot melt shows an three stages: initial incubation time where no solidification occurs, followed by a near-steady rate of solidification and a final jump in solidification rate. They attributed the initial incubation to recalescence phenomena due to nucleation ahead of the solidification front. However, the correlation between the transient solidification velocity and corresponding melt pool microstructure is not discussed by Zhao et al.'s [102]. The current dissertation addresses this research gap by providing a detailed study on transient solidification event as a function of a process parameter (laser power) and its correlation to build microstructure.

Chapter 3

Solidification texture, variant selection, and phase fraction in a spot-melt electron beam powder bed fusion processed Ti-6Al-4V

3.1. Introduction

As reviewed in Sec. 2.1.3, melt strategy has been demonstrated as one of the key parameters to help tune the AM build microstructure. While majority of studies [11, 47, 49, 50] have focused on different variants of the linear raster-melt strategy, Dehoff et. al. [12] applied a spot-melt strategy on an E-PBF IN718 to obtain an effective manipulation of the grain size, orientation, and the morphology from columnar to equiaxed. Subsequently, Raghavan et. al. [15] investigated the relative importance of various process parameters involved in the spot-melt strategy to achieve a higher equiaxed grain fraction in the IN718 builds. Recent work by Nandwana and Lee [16] compared the build microstructure and porosity observed in E-PBF Ti-64 builds manufactured using a spot-melt strategy with the ones built using a conventional raster strategy and found that the novel spot strategy can be used to produce build with minimal porosity with desired microstructures. However, a detailed comparison between the solidification conditions in the above melt strategies in Ti-6Al-4V through the study of solidified β-microstructure and the transformed α-microstructure after the thermal excursions seen in AM is not yet well understood.

In this chapter, we evaluate the differences between a novel spot-melt strategy and a conventional linear-melt (raster scan) in terms of the final build microstructure in an E-PBF Ti-64 alloy. First, the constituent phase fractions (α and β) in the two builds and their variations along the build height are compared. Second, the representative solidification (β) and transformation

(α) textures, and the BOR between the two phases are examined for the linear and spot melt cases. Third, the β <100> build texture characteristics, its relationship with β {110} and β <222>, and their inheritance onto α {0002} and α $<11\bar{2}0>$ are quantified. Further, the variation and prevalence of the BOR along the height of the two builds are examined. Finally, using quantitative analysis of the pole figures, the volume fraction distribution of the texture variants is discussed to identify a potential preferred variant selection in the α phase. (*A version of this chapter was originally published in "Additive Manufacturing" by R.R. Kamath et al.* [52])

3.2. Experimental details

3.2.1. AM build parameters and sample details

The AM samples were built using an ARCAM Q10 Plus electron beam melting machine at the Manufacturing Demonstration Facility, Oak Ridge National Laboratory. The spherical Ti-64 alloy powders used here were manufactured by TEKNA using a plasma atomization process. The composition and particle size distribution of the as-received powders are presented in Table 3.1. The stainless steel substrate was heated to 470°C and held for 30 min to allow the temperature to stabilize across the first powder layer. The vacuum in the build chamber was maintained at 4.5×10^{-2} mbar. Each subsequent powder layer was pre-heated using the electron beam after the powder was raked in on the build. Two cuboid samples were prepared using two different melt strategies, namely linear (L) and spot (S) methods. The linear-melt sample was processed using a typical bi-directional raster scan with a 67.5° rotation for each successive layer as shown in Fig. 3.1a. The beam current and scan speed were determined by the machine software according to the scan length required for a given melting pass by means of a "speed function" parameter [134]. On the other hand, the spot melt sample was processed by a series of single spot melting events following a pre-designed fill sequence as illustrated in Fig. 3.1b.

Table 3.1. Chemical composition (in wt.%, with Ti in balance) and the particle size distribution of the TEKNA (Ti64 -105/45) plasma atomized Ti-6Al-4V alloy powder.

Powder composition (wt.%)					**Size distribution**		
Al	V	Fe	O	C + H + N + Y	< 45 μm	45-105 μm	> 105 μm
6.0-6.5	3.5-4.5	< 0.25	< 0.10	< 0.14	2-5%	85-90%	5-10%

Specifically, during the first pass, a series of spots were melted at the 11th point away from the previous spot, on a given row in an imaginary grid superimposed on the physical build layer. After the first pass on the first row is complete, the next melt sequence is made at the 4th row below from the previous row, however, starting halfway in between the first two points in the previous row. This procedure is repeated until the first pass is complete on a given build layer (as marked with black squares in Fig. 3.1b). Then, the second pass (marked with red squares) is made adjacent to the spots created during the first pass. The procedure continues until all the points on the imaginary grid on the build layer are molten once. For the spot-melt strategy, the electron beam current was maintained at 11 mA) with a gun voltage of 60 kV and a dwell time of 0.3 ms for each spot. The beam diameter was approximately 200 μm, with the beam focus offset set to zero. The thickness of each deposited layer was maintained at 50 μm, translating into a total of about 500 layers in the build. The dimensions of the final 3D printed cuboids were approximately 15 mm (X) × 15 mm (Y) × 25 mm (Z) (Fig. 3.1c). The build time for each layer was approximately 80 s, resulting in a total build time of about 11 hr. The samples were allowed to cool in the build chamber for about 3 hr and no post-process heat treatments were performed. Two rectangular samples, with the dimensions of 1 mm (X) × 1 mm (Y) × 12 mm (Z), were extracted from each cuboid (i.e., L and S) near the center of the build for the texture and phase fraction measurements using S-XRD. The S-XRD measurement locations and their designations are depicted in Fig. 3.1d.

3.2.2. High-energy synchrotron x-ray diffraction

High-energy synchrotron x-ray diffraction (S-XRD) was performed to measure the crystallographic texture and phase fraction in the E-PBF Ti-64 builds at beamline 11-ID-C at the Advanced Photon Source (APS), Argonne National Laboratory. A schematic of the diffraction

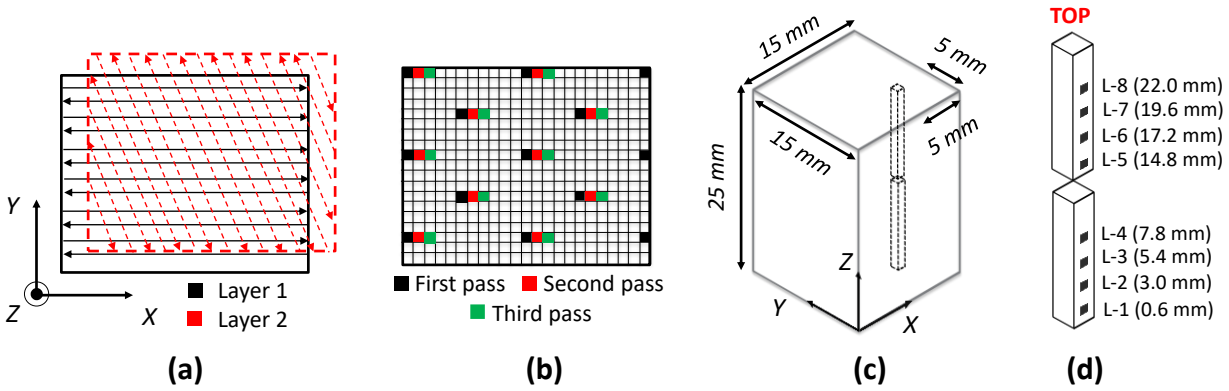

Figure 3.1. Schematics of the melt strategies, sample dimensions, and synchrotron x-ray diffraction (S-XRD) measurement locations: (a) linear (L) melt, (b) spot (S) melt, (c) E-PBF Ti-6Al-4V cuboid with the extracted matchstick samples marked in dotted lines, and (d) sample designations and corresponding locations of S-XRD measurements on the matchstick samples (referred to as AM sample in Fig. 3.2a). For example, L-3 (5.4 mm) indicates the linear melt sample and S-XRD measurement location 3, which is 5.4 mm from the substrate.

measurement setup is presented in Fig. 3.2a. The monochromatic x-ray wavelength was 0.1173 Å (beam energy of 105.7 keV) and the nominal sample-to-detector distance was about 1315 mm, which allowed enough 2θ coverage to obtain 22 HCP (from $10\bar{1}0$ to $21\bar{3}3$) and 8 BCC (from 110 to 400) reflections. Debye-Scherrer rings were measured with a 2D amorphous silicon (Perkin Elmer) detector using a transmission scattering geometry. The incident x-ray beam was collimated to 600 μm × 600 μm. The matchstick AM sample was mounted onto a rotary stage and rotated about the Z-axis (ω) from 0° to 180° at intervals of 30° to obtain full pole coverage for the texture and phase analyses. Nominal diffraction sampling volume of about 1 mm (X) × 1 mm (Y) × 0.6 mm (Z) was used for each measurement and a total of 8 locations were measured along the height for each case from L-1 (or S-1) at 0.6 mm from the substrate to L-8 (or S-8) at 22 mm from the substrate (i.e., near the top), as shown in Fig. 3.1d. The Debye-Scherrer rings were "caked" for piecewise integrations along the azimuthal angle (η) at intervals of 10° using the Fit2D software [135] after calibrating for the detector distance and tilt using a standard CeO_2 powder (NIST SRM 674b). A total of 252 diffraction patterns (i.e., 36 along η times 7 ω angles) were obtained for each measurement location. These diffraction patterns were analyzed using the Rietveld profile refinement method using the Material Analysis Using Diffraction (MAUD) software [136, 137]. The texture extraction from the Rietveld analysis was based on the E-WIMV algorithm. Then, MTEX, a MATLAB-based quantitative texture analysis and plotting software [138], was used to process the pole figures (PFs). Moreover, in order to quantify the intensity of each texture component, the MTEX software was used to locate the pole maxima and to integrate the pole intensity with a radius of 10° around each maximum. These integrated intensities were used for quantitative comparisons between different texture components rather than the maximum peak intensities. Furthermore, the integrated intensity of a specific texture variant is normalized using the summation of all integrated intensities within a given pole figure to obtain a volume

fraction for a given component or a variant set. Fig. 3.2b shows an example pole figure with the sample coordinates superimposed on it. Also, shown are the definitions of the rotation about Y (β) and X (γ) axes used to quantify the inclination of a specific texture components with respect to the sample coordinates.

Owing to a combination of good volumetric statistics and high angular resolution, S-XRD measurements allowed for a direct measurement of the texture and phase fraction of retained β phase. The EBSD study conducted by Shao et al. on a similar set of samples [71] indicates that the width of the retained β ribs varies from 0.08 to 0.1 μm depending on the build location and scan strategy. They also observed the phase fraction of the retained β varying from 7.5 to 10.5 area%, which is similar to our current results to be discussed in the following sections. Assuming that the out-of-plane width and in-plane length of the retained β ribs in the micrographs presented in [71] are on the order of 1 μm and 10 μm, it is estimated that about 10^8 retained β ribs are present in the current S-XRD scattering volume of $1 \times 1 \times 0.6$ mm^3. According to the recalculated prior β grain size of 52 – 57 μm in the spot-melt sample and 106 – 192 μm in the linear-melt sample reported by Shao et al. [71], the average number of prior β grains in the current S-XRD scattering volume are approximately 3500 and 175, respectively. Additionally, Shao et al. [71] reported that the thickness of the α laths varies from 0.43 to 0.73 μm depending on build location and scan strategy. Using the reported α-area fraction range (89.5 – 92.5 area%) and assumptions about the width and length of the retained β ribs, about 10^7 α laths are sampled in the current S-XRD scattering volume. The measured Debye-Scherrer rings in the current study exhibited continuous rings (as opposed to spots) at all measurement locations and orientations, also indicating adequate sampling of β and α phases.

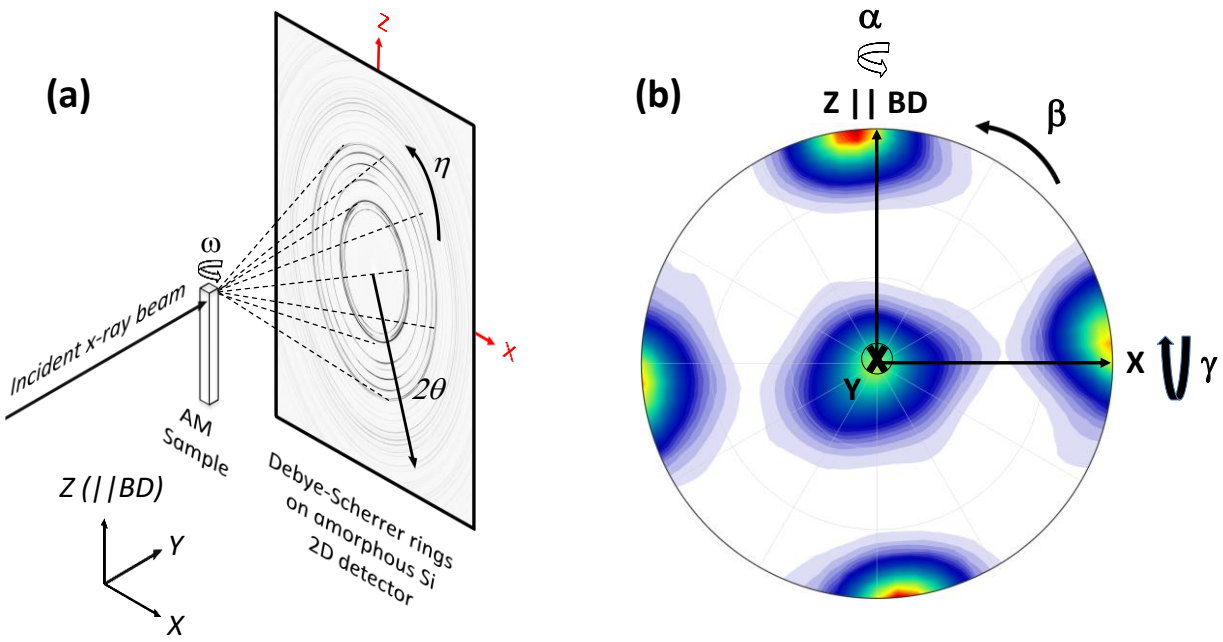

Figure 3.2. Schematic of S-XRD measurement setup and orientation designations. (a) Debye-Scherrer diffraction setup in a transmission geometry at the beamline 11-ID-C, APS. (b) Example pole figure (BCC {200} from L-8) with the sample coordinates. Also, shown are the definitions of the rotation about Y-axis (β) and rotation about X-axis (γ), which describe the tilt of the {200} poles with respect to the sample coordinates.

3.3. Results

3.3.1. Phase fraction, pole figures, and Burgers orientation relationship observed at the top of the build

Fig. 3.3 presents example S-XRD diffraction patterns. Two patterns from L-8, measured along the build direction (i.e., Z-direction) and along 40° away from the build direction towards the -X direction are shown in Fig. 3.3a,b. The diffraction patterns clearly show the presence of the minor BCC (β) phase and the major HCP (α) phase. Also, the differences in the corresponding peak intensities, e.g., among β {200}, β {110}, and α {0002}, along the two different scattering vectors are a typical indication of the texture in both phases. The simultaneous Rietveld refinement of 252 such diffraction patterns at each measurement location for the L and S samples provides the quantitative deconvolution of the texture and phase fraction contributions to the measured diffraction intensities. Also shown in Fig. 3.3c is the diffraction pattern obtained by the full azimuthal integration (0° to 360° along η) of the diffraction rings from the Ti-64 powder used for the build. The measured phase fractions near the top of the two builds (L-8 and S-8) are almost identical with 11 wt.% β (89 wt.% α), which show a significantly larger β fraction compared to the 3 wt.% β (97 wt.% α) measured from the Ti-64 powder feedstock.

The key pole figures (PFs) of β and α phases measured from the linear (L-8) and spot (S-8) melt cases are summarized in Fig. 3.4. This measurement location represents the top-most sampling volume that was subjected to a typical number of re-melting and re-heating cycles but to a minimum duration of the annealing effect during the processing of the entire build. Therefore, the PFs measured from the L-8 and S-8 will be examined first to establish a representative build texture followed by an observation of potential variations along the height of

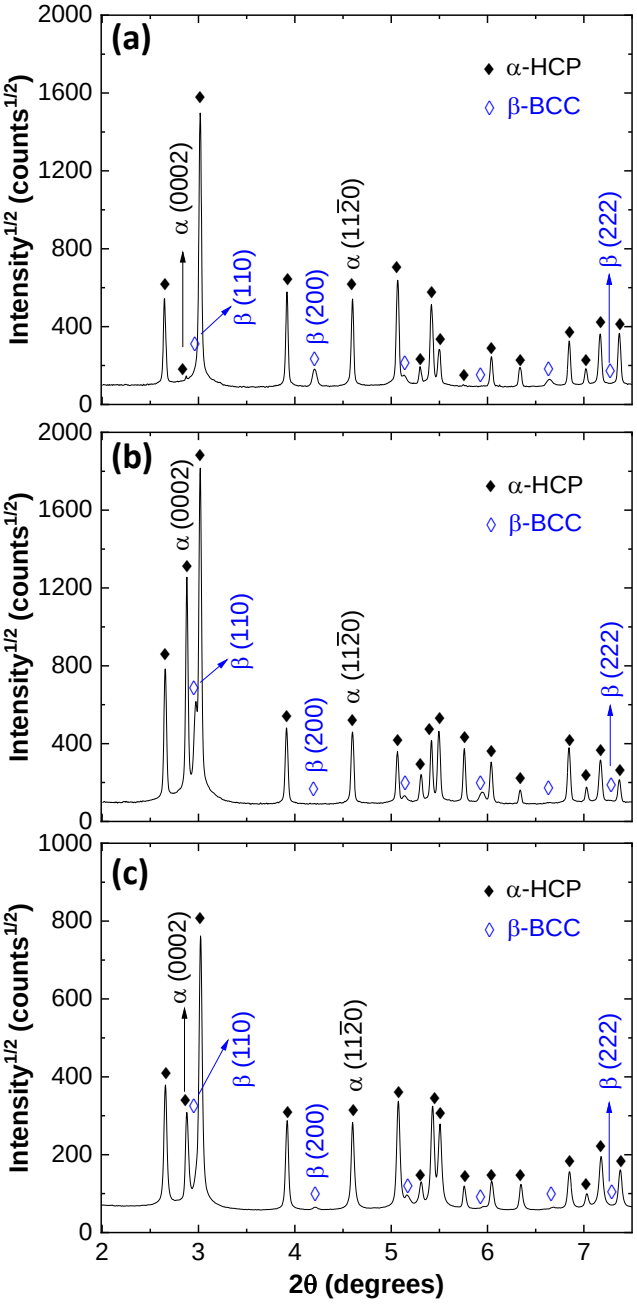

Figure 3.3. Example diffraction patterns obtained by an azimuthal (η) caking of 10° from the Debye-Scherrer rings measured at ω = 0° for the L-8 (i.e., linear melt sample at 22 mm from the substrate): (a) Diffraction pattern measured along the build direction (i.e., Z direction) and (b) Diffraction pattern measured along 40° to the Z direction towards (-X) direction. Also, the diffraction pattern measured from the as-received powder (obtained by full integration of the diffraction rings) is presented in (c) for comparison. The BCC and HCP peaks are labeled in blue (open) and black (closed) diamond markers, respectively.

each sample. First, as a reference, standard projections of β {200}, β {110}, α {0002}, β <222>, and α <11$\bar{2}$0> are presented in Fig. 3.4a from left to right, along with the sample coordinates and relevant β {200} poles (P1-P3) and BOR variants (V1-V12). The specific variants marked in Fig. 3.4a are summarized in Table 3.2 in terms of the planar and directional pairings following a general convention from [77]. The measured PFs of L-8 and S-8 are presented in Fig. 3.4b and Fig. 3.4c, respectively.

For the L-8 (Fig. 3.4b), β {200} PF shows a cube texture, where the P1 (002), P2 (0$\bar{2}$0), and P3 (200) poles align closely with the Z (build direction), Y, and X directions in the sample coordinate, respectively. However, the intensities of the individual poles are not the same. The pole locations in β {110} and β <222> PFs in L-8 are consistent with the β {200} PF as shown in the standard projections in Fig. 3.4a. Moreover, the crystallographic relationship during a transformation from the high-temperature parent BCC β phase to the low-temperature daughter HCP α phase is known to follow the BOR: β {110} || α {0002} and β <222> || α <11$\bar{2}$0> [56]. Fig. 3.4b clearly shows that the pole locations in the α {0002} and α <11$\bar{2}$0> PFs coincide with the ones in the β {110} and β <222> PFs, respectively, qualitatively verifying that the BOR was indeed followed during the β – α phase transformation. Note that the non-BOR α <11$\bar{2}$0> poles are also observed according to the directional symmetry of the HCP crystal structure and are marked accordingly in Fig. 3.4a.

Similarly, for the S-8 (Fig. 3.4c), β {200} PF shows a fiber texture. The most intense P1 (002) pole aligns near parallel to the build direction (with an approximate β-tilt of 12.5° and γ-tilt of 17.5°). A diffuse intensity distribution is observed on the X-Y build plane although the P2 and P3 components are still identifiable. Accordingly, the β {110} and β <222> poles also show a diffuse intensity distribution around the ideal pole locations, with a corresponding tilt consistent with the β {200} fiber texture. Nevertheless, the qualitative correlations between the poles in the

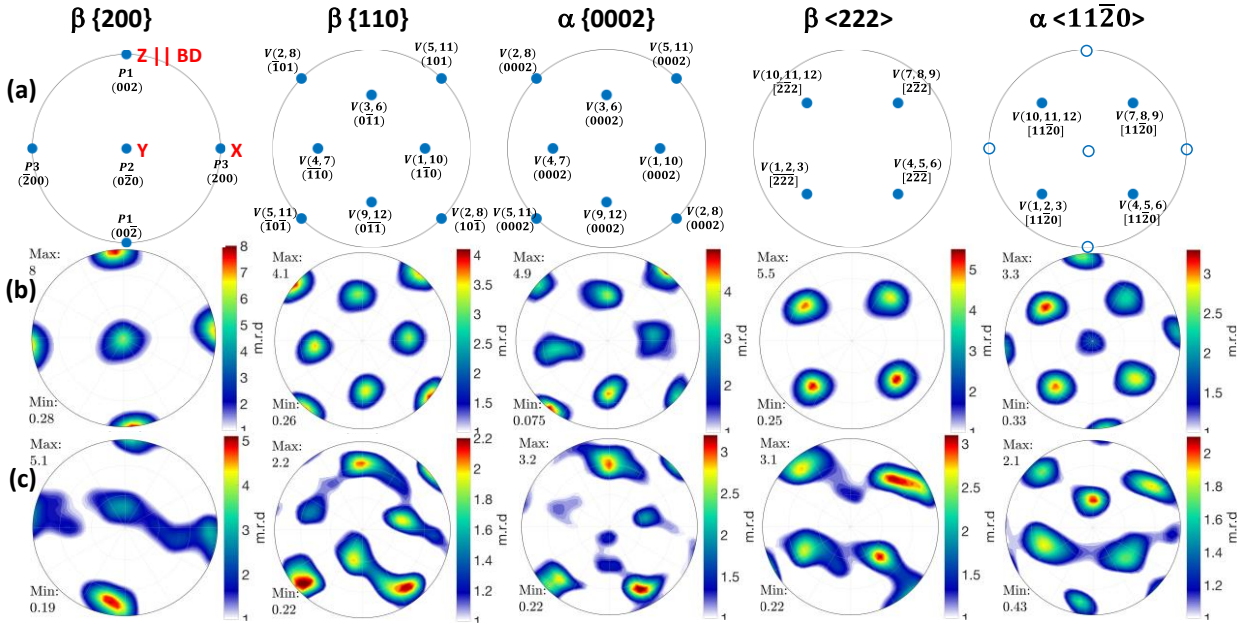

Figure 3.4. Pole figures (PFs) measured from L-8 and S-8 locations of the linear melt and spot-melt samples, respectively. PFs are presented from left to right for the following planes/directions: β {200}, β {110}, α {0002}, β <222>, and α <11$\bar{2}$0>. (a) Standard projections, sample coordinates, and relevant poles marked with contributing variants (Table 3.2). (b) Measured PFs from L-8. (c) Measured PFs from S-8. Note that non-BOR <11$\bar{2}$0> poles are also marked with an open blue circle in (a). The build direction points north and each pole figure is plotted using individual scale to identify key components.

Table 3.2. Summary of variant sets according to the Burgers orientation relationship that are uniquely identifiable from the pole figures of β and α phases measured using synchrotron x-ray diffraction. For a visual representation, see Fig. 3.4a. Note that the naming convention for the variants (V#) follows from Wang et al. [27].

Planar Variant Pairs	Common $\{110\}_\beta$ Plane	Corresponding Directions
V1	$(\mathbf{1\bar{1}0})_\beta \parallel (0002)_\alpha$	$[\bar{2}\bar{2}\bar{2}]_\beta \parallel [11\bar{2}0]_\alpha$
V10	$(\mathbf{1\bar{1}0})_\beta \parallel (0002)_\alpha$	$[\bar{2}\bar{2}2]_\beta \parallel [11\bar{2}0]_\alpha$
V2	$(\mathbf{\bar{1}01})_\beta \parallel (0002)_\alpha$	$[\bar{2}\bar{2}\bar{2}]_\beta \parallel [11\bar{2}0]_\alpha$
V8	$(\mathbf{\bar{1}01})_\beta \parallel (0002)_\alpha$	$[2\bar{2}2]_\beta \parallel [11\bar{2}0]_\alpha$
V3	$(\mathbf{0\bar{1}1})_\beta \parallel (0002)_\alpha$	$[\bar{2}\bar{2}\bar{2}]_\beta \parallel [11\bar{2}0]_\alpha$
V6	$(\mathbf{0\bar{1}1})_\beta \parallel (0002)_\alpha$	$[2\bar{2}\bar{2}]_\beta \parallel [11\bar{2}0]_\alpha$
V4	$(\mathbf{\bar{1}\bar{1}0})_\beta \parallel (0002)_\alpha$	$[2\bar{2}\bar{2}]_\beta \parallel [11\bar{2}0]_\alpha$
V7	$(\mathbf{\bar{1}\bar{1}0})_\beta \parallel (0002)_\alpha$	$[2\bar{2}2]_\beta \parallel [11\bar{2}0]_\alpha$
V5	$(\mathbf{\bar{1}0\bar{1}})_\beta \parallel (0002)_\alpha$	$[2\bar{2}\bar{2}]_\beta \parallel [11\bar{2}0]_\alpha$
V11	$(\mathbf{\bar{1}0\bar{1}})_\beta \parallel (0002)_\alpha$	$[\bar{2}\bar{2}2]_\beta \parallel [11\bar{2}0]_\alpha$
V9	$(\mathbf{0\bar{1}\bar{1}})_\beta \parallel (0002)_\alpha$	$[2\bar{2}2]_\beta \parallel [11\bar{2}0]_\alpha$
V12	$(\mathbf{0\bar{1}\bar{1}})_\beta \parallel (0002)_\alpha$	$[\bar{2}\bar{2}2]_\beta \parallel [11\bar{2}0]_\alpha$

Directional Variant Triplets	Common $\langle 222\rangle_\beta$ Direction	Corresponding Planes
V1	$[\mathbf{\bar{2}\bar{2}\bar{2}}]_\beta \parallel [11\bar{2}0]_\alpha$	$(1\bar{1}0)_\beta \parallel (0002)_\alpha$
V2	$[\mathbf{\bar{2}\bar{2}\bar{2}}]_\beta \parallel [11\bar{2}0]_\alpha$	$(\bar{1}01)_\beta \parallel (0002)_\alpha$
V3	$[\mathbf{\bar{2}\bar{2}\bar{2}}]_\beta \parallel [11\bar{2}0]_\alpha$	$(0\bar{1}1)_\beta \parallel (0002)_\alpha$
V4	$[\mathbf{2\bar{2}\bar{2}}]_\beta \parallel [11\bar{2}0]_\alpha$	$(\bar{1}\bar{1}0)_\beta \parallel (0002)_\alpha$
V5	$[\mathbf{2\bar{2}\bar{2}}]_\beta \parallel [11\bar{2}0]_\alpha$	$(\bar{1}0\bar{1})_\beta \parallel (0002)_\alpha$
V6	$[\mathbf{2\bar{2}\bar{2}}]_\beta \parallel [11\bar{2}0]_\alpha$	$(0\bar{1}1)_\beta \parallel (0002)_\alpha$
V7	$[\mathbf{2\bar{2}2}]_\beta \parallel [11\bar{2}0]_\alpha$	$(\bar{1}\bar{1}0)_\beta \parallel (0002)_\alpha$
V8	$[\mathbf{2\bar{2}2}]_\beta \parallel [11\bar{2}0]_\alpha$	$(\bar{1}01)_\beta \parallel (0002)_\alpha$
V9	$[\mathbf{2\bar{2}2}]_\beta \parallel [11\bar{2}0]_\alpha$	$(0\bar{1}\bar{1})_\beta \parallel (0002)_\alpha$
V10	$[\mathbf{\bar{2}\bar{2}2}]_\beta \parallel [11\bar{2}0]_\alpha$	$(1\bar{1}0)_\beta \parallel (0002)_a$
V11	$[\mathbf{\bar{2}\bar{2}2}]_\beta \parallel [11\bar{2}0]_\alpha$	$(\bar{1}0\bar{1})_\beta \parallel (0002)_\alpha$
V12	$[\mathbf{\bar{2}\bar{2}2}]_\beta \parallel [11\bar{2}0]_\alpha$	$(0\bar{1}\bar{1})_\beta \parallel (0002)_\alpha$

α {0002} and α <11$\bar{2}$0> PFs and those in the parent β {110} and β <222> show that the BOR is followed in the spot melt case as well. Moreover, the texture of S-8 is weaker than that of L-8 according to the maximum texture intensities observed in all PFs.

3.3.2. Quantitative analysis of texture measured at the top of the build

The measured pole intensities were integrated as described in section 3.2.2 for a quantitative analysis of the β build texture and its correlation with the different α variant sets.

3.3.2.1 β{200} intensities

Fig. 3.5a,b present the integrated pole intensities of the β {200} components of L-8 and S-8, respectively. In Fig. 3.5a (L-8), the P1 pole along the build (Z) direction has the highest integrated intensity, followed by P3 and P2. Fig. 3.5b shows a similar result for the S-8 case, where intensity hierarchy follows P1 > P3 > P2. However, the texture intensities of S-8 are significantly lower than those of L-8. For example, P1 and P3 poles for S-8 are about 60% and 40% of those of L-8. Also shown are the volume fractions of each pole component. When comparing the three β {200} components, S-8 case exhibits higher anisotropy (even though the overall texture intensity is lower) with a relatively higher volume fraction of P1 pole along the build direction compared to those of P2 and P3 on the build plane.

3.3.2.2 Intensity distribution among planar and directional variant sets

Fig. 3.5c,d present the intensities measured for the 6 planar variant pairs of β {110} parent and α {0002} daughter (Table 3.2 and Fig. 3.4a) for L-8 and S-8, respectively. The 6 planar variant pairs represent the 6 β {110} planes. For example, the pair of two planar variants V1 and V10 for the β phase represents $(1\bar{1}0)_\beta$ plane with the two body-diagonal directions of

$[\bar{2}\bar{2}\bar{2}]_\beta$ and $[\bar{2}\bar{2}2]_\beta$, respectively (Table 3.2). Since these two variants appear at the same location in the β {110} PF (Fig. 3.4), their intensities are presented collectively as V(1,10) for $(1\bar{1}0)_\beta$ in Fig. 3.5c. Also shown for V(1,10) set is the corresponding intensity of $\{0002\}_\alpha$ daughter. For the β {110} parents in L-8 (solid bars in Fig. 3.5c), the variant pairs of V(2,8) and V(5,11) have higher intensities than other pairs. Similarly, in the α {0002} daughters (hatched bars), the same V(2,8) and V(5,11) pairs have higher intensities. But, in comparison to the parent intensities, the V(9,12) daughter has higher intensity than its parent and appears to be preferentially selected. For the β {110} parents in S-8 (Fig. 3.5d), the variant pair V(5,11) displays the highest integrated intensity followed by V(2,8) and V(3,6). For the α {0002} daughters, V(2,8), V(3,6) and V(5,11) are predominantly selected.

The integrated intensities for the 4 directional variant triplets in L-8 and S-8 are presented in Fig. 3.5e,f. The four directional variant sets represent the four β <222> directions. For example, the set of three directional variants V1, V2, and V3 for the β phase represents $[\bar{2}\bar{2}\bar{2}]_\beta$ direction that lies on $(1\bar{1}0)_\beta$, $(\bar{1}01)_\beta$, and $(0\bar{1}1)_\beta$ planes, respectively (Table 3.2). Again, since these variants appear at the same location in the β <222> PF (Fig. 3.4a), their intensities are presented collectively as V(1,2,3) for the $[\bar{2}\bar{2}\bar{2}]_\beta$ direction in Fig. 3.5e,f. Also shown for V(1,2,3) set is the corresponding intensity of α $<11\bar{2}0>$ daughter. Overall, the intensities of the parent β <222> are relatively evenly distributed among different variants in both L-8 and S-8 cases. Although the differences are subtle, the parent V(7,8,9) is the lowest in L-8 but the highest in S-8. Moreover, the parent to daughter ratios do not suggest an obvious preference in directional variants in both melt cases.

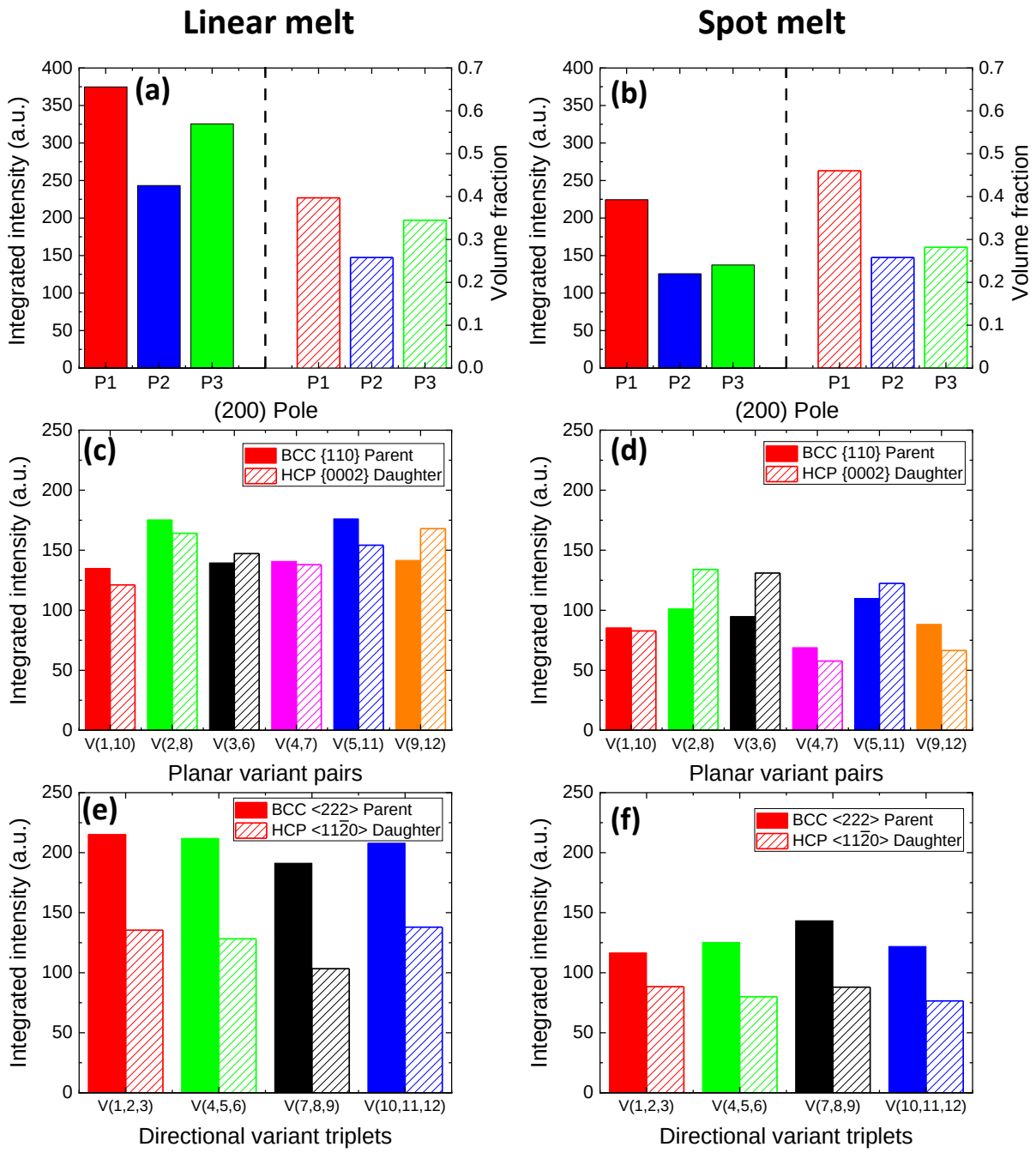

Figure 3.5. The integrated intensities (solid bars) and corresponding volume fractions (hatched bars) of β{200} poles of P1, P2, and P3 are presented for (a) L-8 and (b) S-8. The integrated intensities of parents (solid bars) and corresponding BOR daughters (hatched bars) of the six pairs of planar variant pairs of β {110} and α {0002} are shown for (c) L-8 and (d) S-8. The integrated intensities of parents (solid bars) and corresponding BOR daughters (hatched bars) of the four directional variant triplets of β <222> and α <11$\bar{2}$0> are shown for (e) L-8 and (f) S-8.

3.3.3. Variations of phase fractions and texture along the build height

It is well known that the microstructure of AM builds can be spatially heterogeneous within the build due varying thermal conditions [18, 31, 65, 69, 70]. Hence, in this section, the potential variations of the phase fraction and texture along the build height are examined in a similar fashion to the analysis performed for the top of both builds in the previous section.

3.3.3.1 Variations of phase fractions along the build height

Fig. 3.6 presents the changes in α and β phase fractions along the build height for both L and S cases. First, both AM builds have significantly higher β phase fraction compared to the as-received powder (about 3 wt.% β). Second, both AM builds show a slight decrease in the β phase fraction from the top of the build towards the substrate. Finally, the β phase fraction in the linear melt case is slightly higher than the spot melt case throughout the build height.

3.3.3.2 Pole figures measured along the build height

The variation of the texture along the sample height is shown for the linear and spot melt samples in Fig. 3.7, 3.8. The β {200} build texture in the linear melt case (Fig. 3.7) shows the cube texture similar to that observed in L-8 for all of the measurement locations, while the overall intensity decreases from the top to the substrate. Also, slight tilts in the PFs were observed across the height. Nevertheless, the locations of α {0002} and α $<11\bar{2}0>$ components coincide very well with the parent β {110} and β <222> components showing that the BOR prevails in all measured locations even when the overall texture intensity weakens quite significantly. In the spot melt (Fig. 3.8), the β {200} fiber texture is consistently observed along the height except for S-4. The overall intensity remains relatively constant unlike the linear melt case.

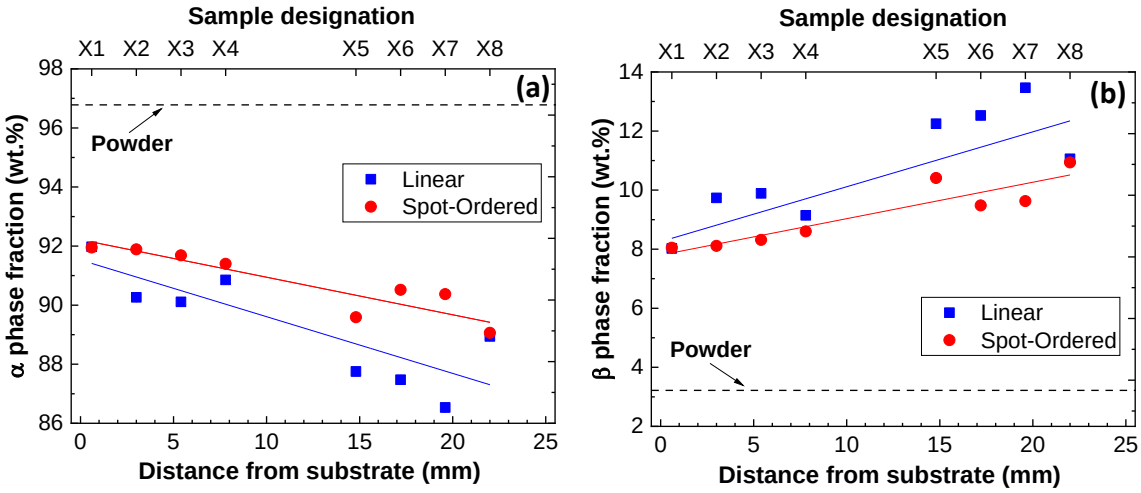

Figure 3.6. The changes in the phase fractions along the height of the linear (L) and spot (S) melt samples measured using S-XRD. (a) α phase and (b) β phase. The phase fractions measured from the as-received alloy powder are also presented. A typical standard deviation for the phase fraction obtained from the Rietveld refinement is about ± 0.2 wt.%. Note that the X in the sample designation stands for L or S.

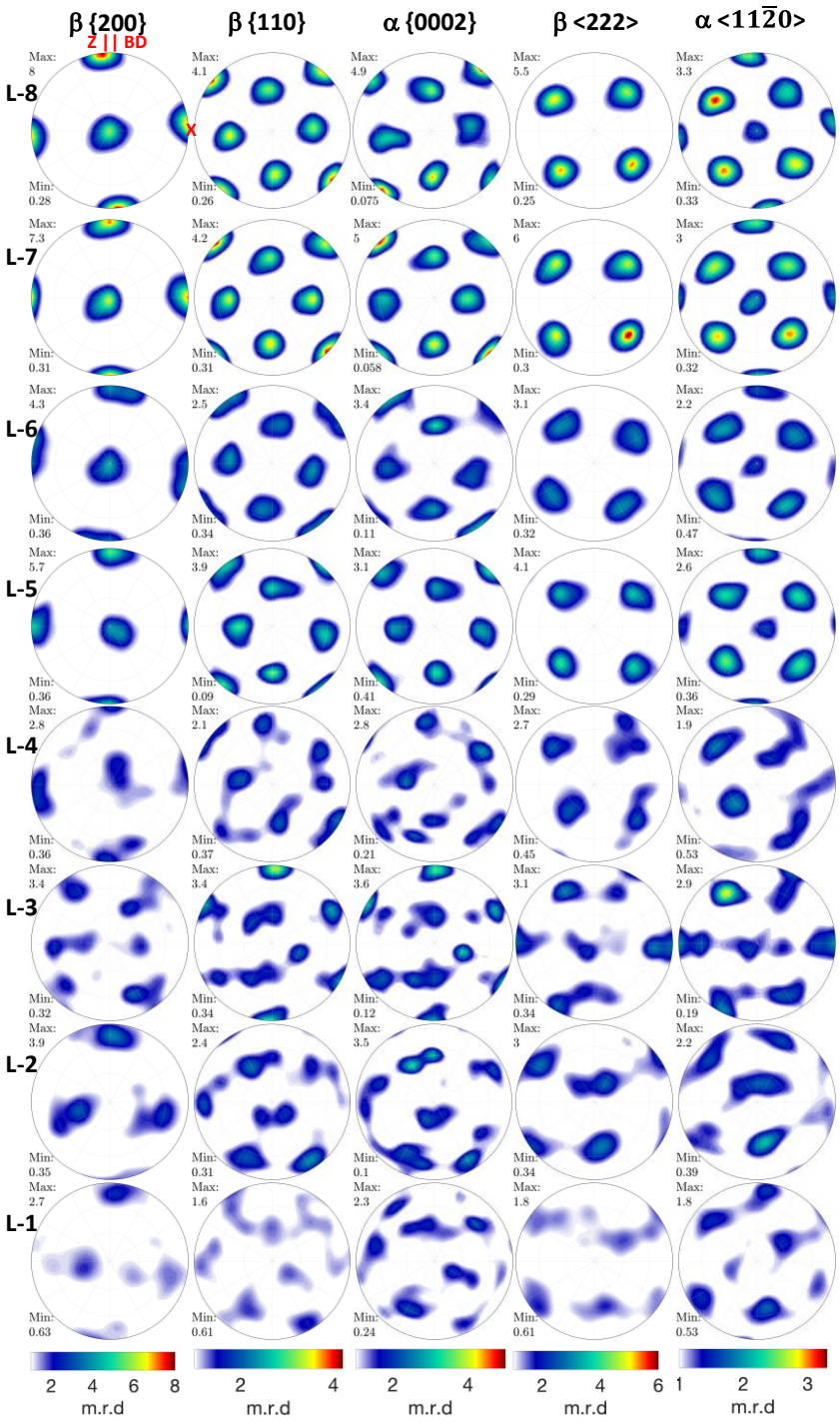

Figure 3.7. The PFs, measured along the height of the linear melt case (L), are presented for the β {200}, β {110} || α {0002} pair, and β <222> || α <11$\bar{2}$0> pair. A common scale is used for each PF for a qualitative comparison along the build height. The overall intensity of the texture decreases from top to substrate while maintaining the cube characteristics for the β {200} build texture.

Also, the maxima to maxima correlations can be quite clearly identified within the diffuse bands in the PFs according to the BOR at all measurement locations.

3.3.3.3 β {200} pole intensities and misorientations

The β {200} build texture intensities and misorientations observed in Fig. 3.7, 3.8 are quantified. First, Fig. 3.9a shows that, in the linear melt sample, the integrated intensities of P1, P2, and P3 exhibit a deceasing trend from near the top of the build (L-8) to near the substrate (L-1). On the other hand, Fig. 3.9b shows that, in the spot melt sample, the intensity fluctuates and does not show a clear trend along the height. The volume fractions of P1, P2, and P3 poles are presented for the linear and spot melt samples in Fig. 3.9c,d. For the linear melt case, while the overall intensity changed systematically from the top to the bottom of the build, the volume fraction of P1 pole remains quite consistently in between 0.35 and 0.4, which is slightly above the ideal cube volume fraction of 0.33. Moreover, the P1 > P3 > P2 hierarchy observed at L-8 seems to be the general trend throughout the sample height with the P3 at near ideal (0.33) and the P2 mostly below it. In the spot melt sample (Fig. 3.9d), the volume fraction of P1 pole is significantly higher throughout the sample height and the hierarchy of P1 >> P3 > P2 represents the general trend.

The PFs in Fig. 3.7, 3.8 showed that the P1 pole is often tilted away from the build direction. Fig. 3.10 summarizes those tilts of the P1 pole about Y and X directions (in terms of the tilt angles β and γ, respectively). For the linear melt (Fig, 10a), the γ-tilt of the P1 pole is higher near the substrate and decreases to a low value of 0°- 5° moving away from the substrate. The β-tilt of the P1 pole away from the build direction is generally low (0°- 5°), except for L-3.

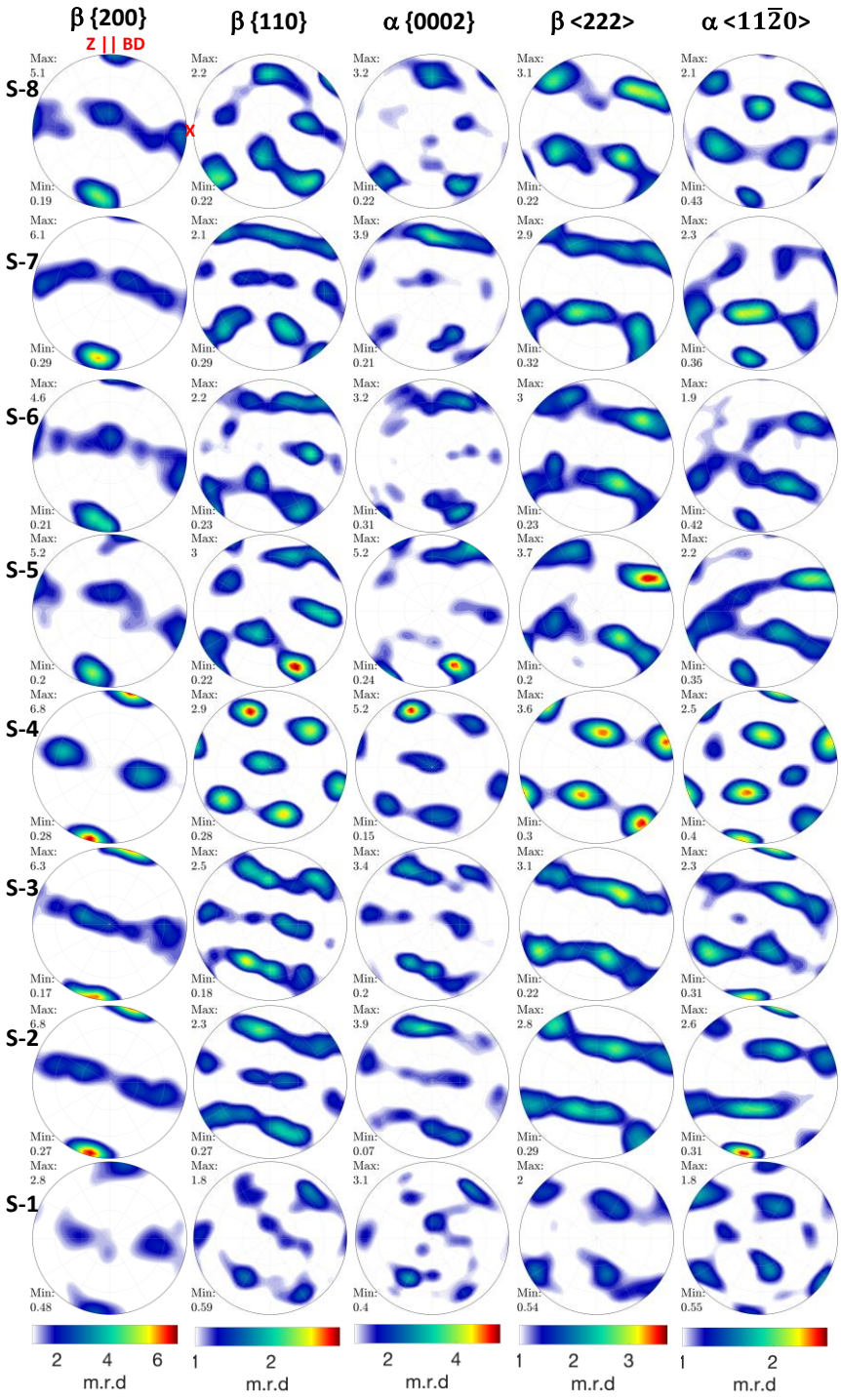

Figure 3.8. The PFs, measured along the height of the spot melt case (S), are presented for the β {200}, β {110} || α {0002} pair, and β <222> || α <11$\bar{2}$0> pair. A common scale is used for each PF for a qualitative comparison along the build height. The overall intensity of the texture does not change significantly along the build height. The β {200} mostly remains as a fiber type.

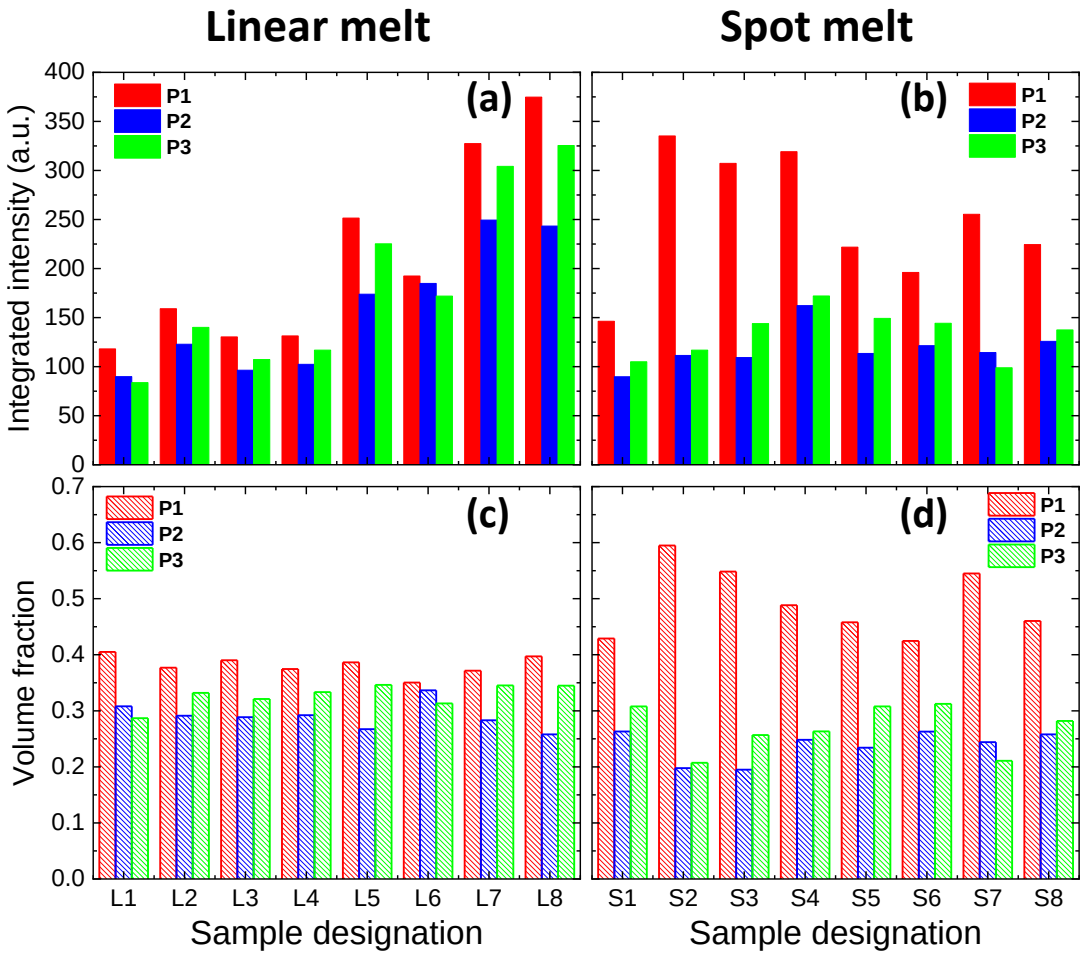

Figure 3.9. The integrated intensities of the β {200} poles of P1, P2, and P3 measured as a function of the build height for (a) linear (L) and (b) spot (S) melt samples. The corresponding volume fractions are presented for (c) L and (d) S.

For the spot melt, the γ-tilt of the P1 (Fig. 3.10b) pole is in the 0°- 5° range for the lower half of the sample and 15°- 18° for the top half of the sample. The β-tilt of the P1 pole is constant at about 10°- 15°.

3.3.3.4 Planar and directional variants

The integrated intensities measured for the planar and directional variants in the linear melt sample are presented as a function of the build height in Fig. 3.11. The 6 planar variant pairs for the β {110} parents and α {0002} daughters are shown in Fig. 3.11a,b. The general trend of decreasing β {200} seen along the height towards the substrate (Fig. 3.9a) is directly translated to the β{110} parent, which in turn, is inherited by the α {0002} daughter. Among the six planar variant pairs, V(2,8) and V(5,11) have the highest intensities among the β {110} poles at most locations, whereas V(2,8) and V(9,12) are the most prominent among the α {0002} poles. The 4 directional variant triplets of parent β <222> and daughter α $<11\bar{2}0>$ are shown in Fig. 3.11c,d. Similar to the planar variants, the integrated intensities of β <222> and α $<11\bar{2}0>$ decrease from the top to the bottom of the sample. Among the 4 directional variant triplets, V(1,2,3) seems to be weakly favored for both β <222> and α $<11\bar{2}0>$, whereas V(7,8,9) is clearly the least favorite at almost all locations along the build height.

Fig. 3.12 presents the planar and directional variants for the spot melt sample. The integrated intensities of β {110} || α {0002} (Fig. 3.12a,b) and β <222> || α $<11\bar{2}0>$ (Fig. 3.12c,d) exhibit a relatively uniform intensity along the build height except for S4 where a relatively strong rotated cube texture was observed. The planar variants of V(2,8) and V(5,11) for the β {110} and V(2,8), V(3,6) and V(5,11) for the α {0002} are prominent at most build locations.

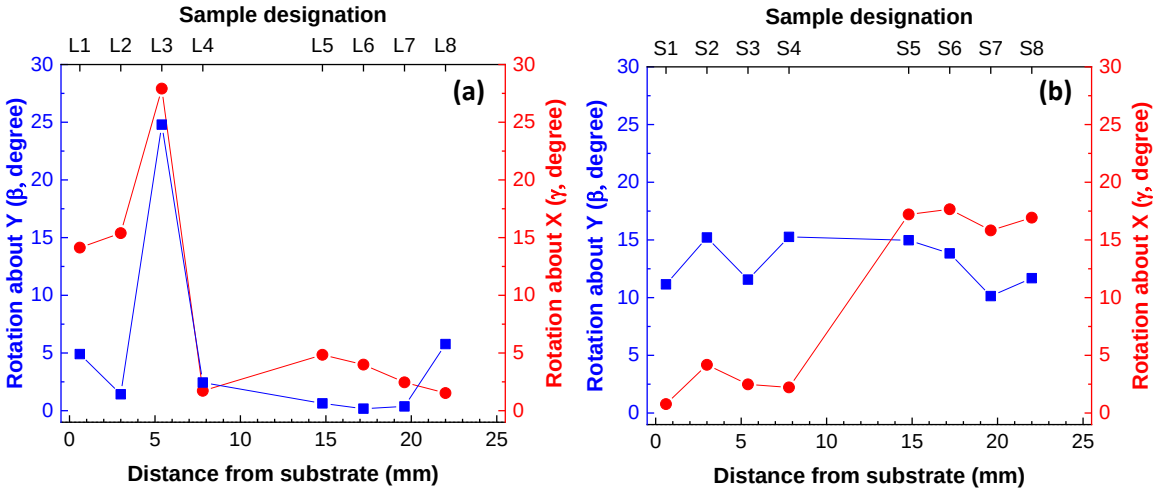

Figure 3.10. The misorientation of the β {200} pole (P1) with respect to the build (Z) direction measured in terms of the rotation of the PF about Y and X axes: (a) linear and (b) spot melt.

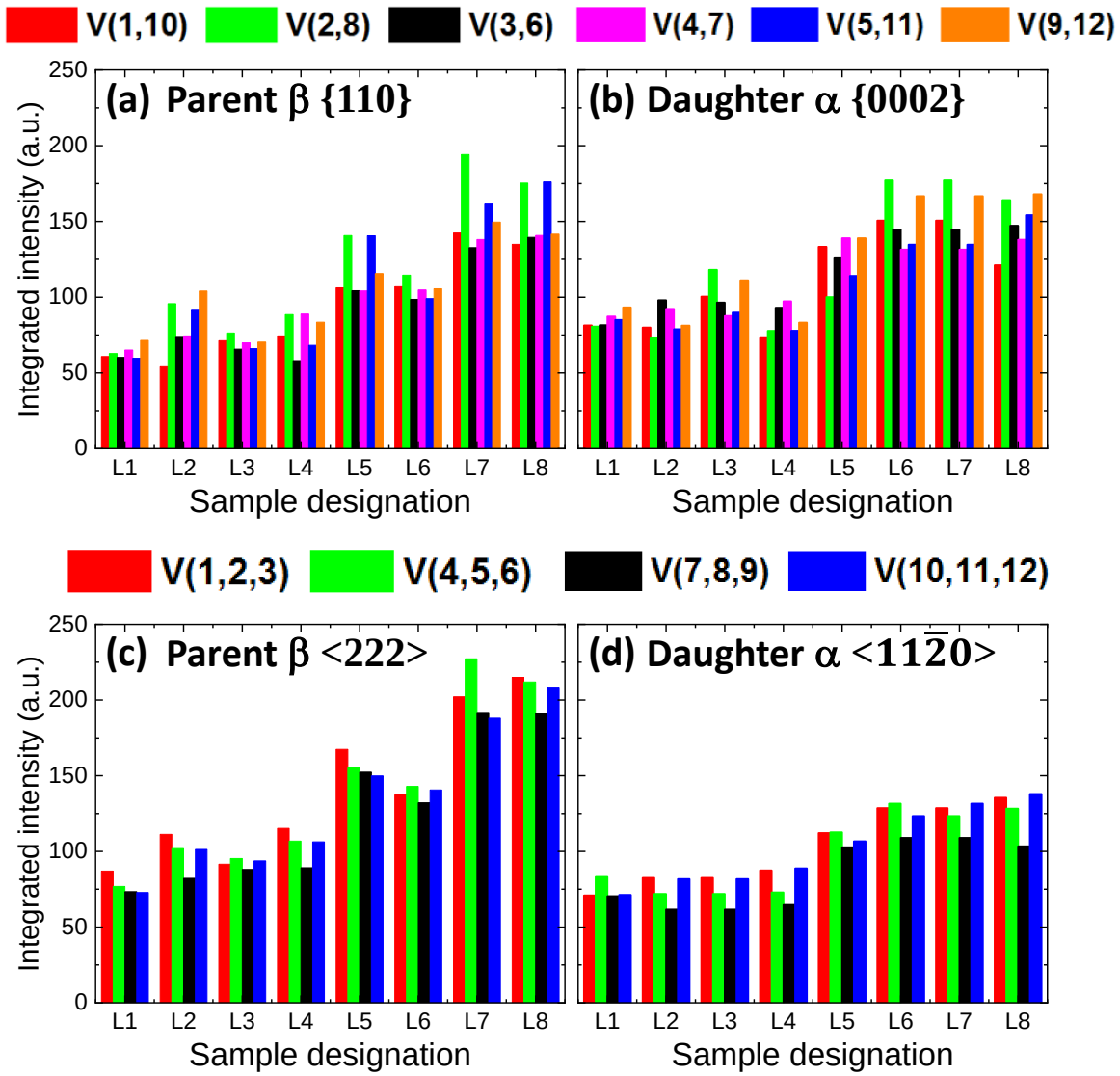

Figure 3.11. The integrated intensities of planar and directional variants in the linear (L) melt case obtained from the PFs as a function of the build height. Planar variants of: (a) parent β {110} and (b) daughter α {0002}. Directional variants of: (c) parent β <222> and (d) daughter α <11$\bar{2}$0>.

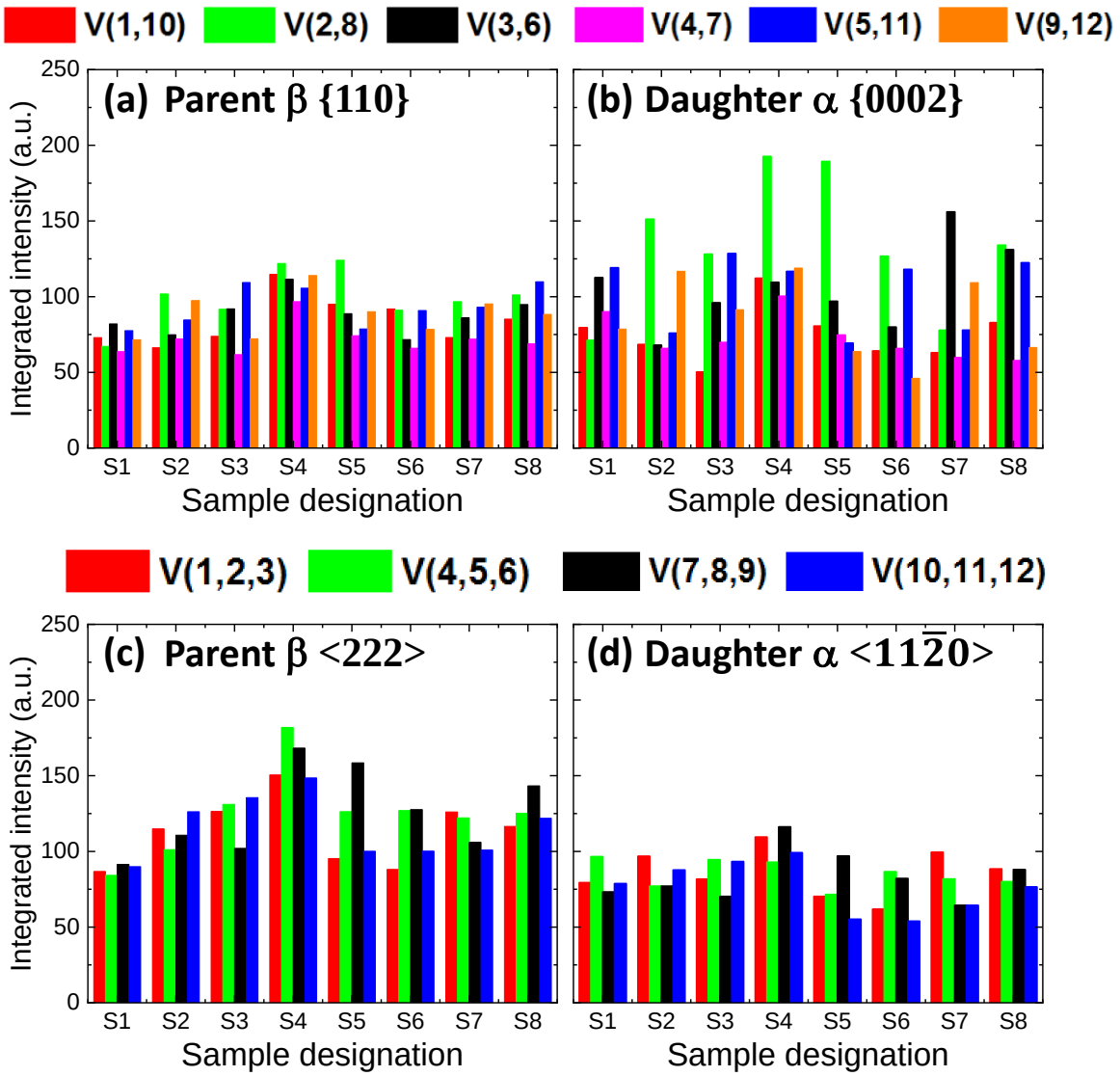

Figure 3.12. The integrated intensities of planar and directional variants in the spot (S) melt case obtained from the PFs as a function of the build height. Planar variants of: (a) parent β {110} and (b) daughter α {0002}. Directional variants of: (c) parent β <222> and (d) daughter α <11$\bar{2}$0>.

Among the 4 directional variant triplets, β <222> (Fig. 3.12c) poles and α <11$\bar{2}$0> (Fig. 3.12d) poles do not present a dominant variant set but either V(4,5,6) or V(7,8,9) is somewhat stronger than others in most locations.

3.4. Discussion

3.4.1. Phase fractions in the AM builds

On equilibrium cooling, the β phase transforms to Al-rich α phase and V-rich β phase, following the Burgers orientation relationship between the two phases [56]. Elmer et al. [55] reported an equilibrium β-phase fraction of 4 wt.% calculated using a pseudo-binary phase diagram of a Ti-6Al and V with similar nominal compositions as the alloy powders used in the present study. The β-phase fractions observed for various AM-Ti64 builds with the processing methods and characterization techniques used for the phase fraction measurement are summarized in Table 3.3 [55, 60-65]. Most linear-fill L-PBF builds consist of a fully α' martensitic structure with almost no β in their as-built condition due to a relatively higher cooling rate involved during the processing without an active substrate pre-heating. However, an increase in the β fraction is often observed when the L-PBF builds are subjected to an annealing treatment [63, 64]. In the case of linear-fill E-PBF Ti-64, the β fraction ranges from 1 to 5 wt.% even in the as-built condition [60-62, 65] in spite of the cooling rate still being orders of magnitude higher than that necessary for the α' martensite formation (410 K/s [58]). This is attributed to the decomposition of the α' to α + β phases due to the annealing of the previously-built layers [60, 65] facilitated by the substrate being heated to relatively higher temperatures (450-700°C for Ti-64). Such an annealing effect allows for the diffusion of vanadium away from the V-supersaturated α' phase and results in the formation of α and β phases. While this hypothesis is based on the idea of complete transformation of α' to β phase via the diffusion of V, a study on a

competing hypothesis has been carried out by Sridharan et al. [66]. The study used atom-probe tomography and correlative transmission Kikuchi diffraction to determine that the product β phase is the product of a shear-induced transformation of α' to α + β phases below the β transus. In the present work, the former hypothesis was used that involves the diffusional transformation of α' to β phase.

In the present study, the β fraction of the feedstock powders is about 3 wt.% (Fig. 3.6b). According to a study on plasma-atomized Ti-64 powders by Birt et al. [139], a small amount of β phase could be retained during cooling in larger powder particles (> 40 μm) even when the estimated cooling rates are in the range of 100 – 1000 K/s. Such observation is consistent with the current result since over 90% of the particles has the size greater than 45 μm (Table 3.1).

The β fractions in the current E-PBF Ti-64 builds are consistently higher than the feedstock powder along the height. Moreover, the β fraction is the highest near the top and decreases towards the substrate in both the builds (Fig. 3.6b). Potential changes in the extent of decomposition of the initial α' into α + β phases during the successive depositions of the build layers and annealing during the entire build duration might be responsible for the changes in the phase fraction along the build height. During the melting of a fresh powder layer, the previously processed sub-surface layers experience thermal excursions ranging from re-melting to re-heating, gradually reaching lower peak temperatures deeper below the current layer. Tens of sub-surface layers below the current build surface would experience such thermal cycling reaching temperatures well above the average substrate temperature during the E-PBF processing [33]. Moreover, as the build height increases gradually, the poor thermal conductivity of Ti-64 would result in a higher heat accumulation at the locations nearer to the build surface. Thermodynamic simulations show that the equilibrium β phase fraction decreases [33] and the corresponding V content in the β phase increases [55] with decreasing temperature. Then, it can be postulated that

the α' would have decomposed to result in a higher β phase fraction as the build height and the heat accumulation increase accordingly. Consequently, the β phase fraction would be lower near the substrate than near the top surface, which is consistent with the current S-XRD results for both linear and spot melt cases (Fig. 3.6b). A similar observation in β fraction was made from the EBSD results on linear-fill E-PBF Ti-64 by Lu et al. [140] and it was attributed to the higher heat accumulation occurring near the top than the bottom of the build. Moreover, this trend is more pronounced for the linear melt sample than for the spot melt sample (Fig. 3.6). This can be explained in terms of the simulated melt pool characteristics shown by Nandwana and Lee [16], where single linear melt resulted in a shallower melt pool compared to the single spot melt. Combined with a more rapid re-melting cycles, this generates a higher heat accumulation in the linear melt compared to the spot melt. This would result in an overall higher β phase fraction in the linear-melt sample than in the spot melt sample.

However, it can be also speculated that the near top surface data represents the as-built microstructure and, therefore, there are inherent differences between the linear and the spot-melt cases as manifested by the higher β phase fraction in the raster case. Moreover, the initially higher β phase fraction could, in turn, gradually decrease due to the subsequent lower temperature annealing during the build duration. As such, the locations that were near to the substrate, that were subjected to a longer annealing duration, could exhibit a lower β phase fraction.

Table 3.3. β phase fractions (in wt.%) observed for various AM-Ti64 builds with their processing methods and characterization techniques used for the phase fraction measurement. (Note that the balance is α in wt.%.)

Processing method	Technique*	β fraction (wt.%)	Comments	Reference
Mill annealing	LOM	12.71	vol.% (**)	[46]
AM E-PBF	APT	3.5 ± 0.5	10-mm build	[47]
	APT	4.6 ± 0.8	20-mm build	[47]
	ND	1 ± 0.3	As built	[48]
	ND	6 ± 0.3	Heat treated	[48]
	LOM	5	-	[44]
	APT	3.56 ± 0.51	-	[44]
	TEM-EDX	2.85	vol.%	[49]
AM L-PBF	SEM	1.5-6.15	Heat treated	[50]
	SEM	0-5	Heat treated	[51]
Equilibrium	Thermo-Calc	4	-	[46]

*AM: additively manufactured, LOM: light optical microscopy, APT: atom probe tomography, ND: neutron diffraction, TEM-EDX: transmission electron microscopy - energy dispersive x-ray analysis, SEM: scanning electron microscopy, EBSD: electron back-scattered diffraction.
**Values reported in vol.% were converted to wt.% using ideal atomic densities of the β-Ti and α-Ti obtained from the average lattice parameters obtained during the Rietveld refinement.

3.4.2. β {200} texture development

The build texture of AM Ti-64 parts has been studied extensively using the EBSD technique [18, 31, 69-73]. Owing to a relatively low β phase fraction, the α build texture is determined experimentally and a β reconstruction algorithm is used to deduce the orientation of parent β grains using the BOR as a basis [141]. Studies carried out on both raster-filled L-PBF [69] and DED [73] Ti-64 report that the prior β grains have a <100> type texture along the build direction with a slight tilt. Similar observations were made on their E-PBF [18, 31, 70-72] counterparts. Bulk neutron diffraction measurements of AM-Ti64 also reported similar results [61, 142, 143]. It is noteworthy that Pesach et al. [142] observed a weak cube type β <100> texture in raster-fill E-PBF Ti-64, as opposed to a strong fiber type texture in the case of L-PBF Ti-64.

In the present S-XRD study, the β {200} build texture, measured directly from the β phase, is a cube type texture in the linear melt sample (Fig. 3.4), which is in good agreement with the literature. On the other hand, the spot melt sample exhibits a fiber type texture. Given that the unit process of E-PBF is melt-pool solidification, recent studies employed the thermal gradient (G) and interface velocity (R) at the liquid-solid interface as the governing physical variables to explain solidification microstructure and texture development during processing [18, 29]. Wei et al. [19] showed that the easy growth direction (which is of the <100> type for cubic systems) aligns with the direction of the maximum thermal gradient at the liquid-solid interface during the solidification of a melt pool. This is corroborated by numerous studies on Ti-64 mentioned earlier [18, 28, 31, 69, 71, 144], wherein an epitaxial growth of coarse-grained, columnar β microstructure was reported with BCC <001> along the build direction.

The study on the effect of melt strategy on the microstructure development during the AM process has mainly been focused on the nickel-based superalloys [11, 12, 15, 47, 50, 116,

145]. Recently, however, several studies [16, 71, 72, 120, 121] reported the effect of spot-melt strategy on the microstructure development in the E-PBF Ti-64. For example, Nandwana et al. [146] reported that the spot-melt strategy offers a flexibility in the control of heat distribution imparted onto the build due to the availability of numerous fill patterns that can be implemented. This could potentially translate into a method of localized microstructural control in AM components.

In their study on spot-melt E-PBF IN718, Raghavan et al. [116] used two probable rapid solidification mechanisms to explain the grain size and overall misorientation of grains from the build direction, namely (i) epitaxial growth and (ii) heterogeneous nucleation ahead of the epitaxial solidification front followed by grain selection and subsequent columnar growth. In the case of epitaxial growth, the dendrite growth direction is determined by the shape of the melt pool bottom. Lower the curvature of the melt pool bottom, smaller is the deviation of the easy-growth direction <001> of pre-existing-grains from the maximum thermal gradient in the melt pool. This facilitates the growth of coarse columnar grains with a smaller misorientation from the build direction. In the second case, the higher curvature of the melt pool bottom results in a higher degree of deviation of the easy-growth directions from the maximum thermal gradient direction, consequently increasing the dendrite tip velocities. Then, the higher dendrite tip velocities lead to an increase in tip undercooling and result in the heterogenous nucleation of equiaxed grains ahead of the solidification front. After a brief period of competition, grains with the thermal gradient vector most favorably aligned <001> direction are selected and columnar growth is restored. This mechanism facilitates the growth of finer columnar grains with higher misorientation from the build direction. These mechanisms can be applied to explain the current results on the texture development.

First, the results obtained for the linear-melt case will be discussed. Nandwana and Lee [16] showed that the melt pool in the single linear melt is shallow in the depth direction (with a

lower curvature at the bottom of the melt pool interface) and is elongated in the direction of the raster. It is likely that a relatively quick re-melting would result in agglomerations of several such elongated melt pools [51]. This conjoined melt pool combined with a higher thermal gradient (G) across its depth follows the first mechanism outlined by Raghavan et al. [116] resulting in the epitaxial growth of large columnar β grains with a small misorientation along the build height, spanning over multiple build layers. This results in the observed cube texture for the linear-melt case with consistent and relatively smaller tilts along the build height (Fig. 3.10a). On the other hand, the fiber texture observed in the spot-melt case can be explained on the basis of the second mechanism outlined by Raghavan et al. [116]. Nandwana and Lee [16] showed that the melt pool in the single spot melt can be deeper (with a higher curvature) than the linear-melt case for the present beam parameters. Ideally, the complete solidification of the current spot melt pool could be achieved before the melting of the neighboring point (Fig. 3.1b) given a sufficiently long return time of the beam. However, due to the low thermal conductivity of Ti-64, a relatively shorter duration between adjacent melt spots can result in joining of the newly melted spot and previous incompletely solidified melt-pool spot, producing an irregular melt pool shape [51, 116]. Owing to its higher curvature at the melt pool bottom, this deeper, possibly irregular melt pool, results in the formation of smaller β columnar grains via the heterogeneous nucleation and competitive growth mechanism. This could rationalize the formation of the fiber texture and the higher tilts observed in the spot-melt case in most parts of the build (Fig. 3.10b) as compared to the linear-melt case. The reconstructed prior-β EBSD microstructures obtained by Shao et al. [71] corroborates well with the mechanisms described above.

In addition, the texture characteristics of the current spot-melt sample, in terms of the pole locations, their intensities, and overall tilt, are quite consistent throughout the entire build height (Fig. 3.8) unlike many AM samples that display significant heterogeneity in microstructure

and texture distributions [70, 142]. In fact, the current linear-melt case (Fig. 3.7) also exhibited a weaker texture intensity near the build plate, which is consistent with the observation by Pesach et al. [142] that showed the locations near the base plate had a lower texture intensity compared to the top of the build in their linear-melt E-PBF Ti-64. The average melt-pool dimensions are consistent across multiple layers as the build progresses in the spot melt, thus leaving a relatively homogenous thermal signature. This allows for the texture to be influenced more strongly by the bulk solidification rather than the substrate. On the contrary, the shallow, conjoined melt-pool described above for linear melts results in the epitaxial growth. And, as the build progresses, the gradual increase in the heat accumulation mentioned earlier [140] would further enhance the already prominent epitaxial growth and results in a stronger β texture intensity in the linear melt.

3.4.3. Burgers orientation relationship between β and α

EBSD studies on E-PBF Ti-64 [18, 31, 71, 72] and L-PBF Ti-64 [69, 70] often utilize the BOR as a basic assumption to perform β grain reconstruction from the measured α data. However, there are several EBSD [73, 120] and neutron diffraction [61, 142, 143] studies on AM Ti-64, where direct observations of the orientation relationship were reported. Similarly, the current S-XRD measurements resolved the β phase and allowed a direct determination of the orientation relationships between the parent β and daughter α. The BOR was identified using the measured PFs of both β and α phases for the linear and spot melts (Fig. 3.4, 3.5). Moreover, this relationship prevails along the build height for both linear and spot-melt cases, irrespective of the texture intensity (Fig. 3.7, 3.8, 3.11, 3.12). A noteworthy point here is that the texture components follow the BOR even after numerous progressive thermal excursions about the β transus, in the (α + β) phase field, and finally, during the in-situ annealing (at about 470°C due to the substrate heating). In an E-PBF Ti-64 build, the cooling rate is orders of magnitude higher than the critical

cooling rate for the martensitic phase transformation in Ti-64 (410 K/s [58]) as estimated by Galarraga et al. [33]. This martensitic transformation strictly follows the BOR [79] and results in the selective formation of α' variants, which favorably accommodate the transformation strain [77]. Fundamental in-situ heating/cooling studies on wrought Ti-64 alloy by Bhattacharyya et al. [74], Lonardelli et al. [75], and Obasi et al. [76] concluded that, on heating, the α-to-β transformation occurs by the growth of the pre-existing/retained β, as opposed to the nucleation of new β. It was also observed that a subsequent reverse transformation from β-to-α on cooling results in the strengthening of texture components corresponding to the α variants present before the forward α-to-β transformation. In the present context, since the texture of the retained β in a build layer is expected to be the same as the texture developed during the initial liquid-to-β transformation occurring at the melt-pool boundary, the above findings suggest that the final β texture after the thermal cycling about the β or (α + β) phase fields would resemble the initial solidification texture in β. Additionally, the α' variants formed during the cooling part of the thermal cycling would be the same initial α' formed during the deposition of the particular build layer. This "texture memory effect", often observed in thermo-mechanically processed Ti-64 alloys [74-76], may be responsible for the prevalence of the BOR relationship through the post-solidification thermal cycling in the E-PBF as well. Furthermore, when the layers are subjected to the in-situ annealing, the α' would transform into an (α + β) microstructure without any appreciable driving force for a change in the texture components. The studies mentioned above [74-76] also reported the possibility of grain growth in the β field and the consequent production of new α' variants, thus resulting in an appearance of new texture components. However, since longer hold times are required for such grain growth, this is unlikely in the case of E-PBF due to relatively short durations of the layer being present in the β field during the thermal cycling.

3.4.4. Predominant variants in the α phase

During the transformation of β-to-α following the BOR, each prior β orientation can transform into one of the twelve equivalent α orientation variants (Table 3.2). A non-random preference of certain variants (or variant selection) was not noted in many of the studies on linear-fill L-PBF and E-PBF Ti-64 [18, 31, 69]. However, preferred variant selection in the α phase was qualitatively indicated in a laser-fusion TC21 (α+β) titanium alloy based on the unequal intensity distribution in the pole figures [147]. In an EBSD study conducted by Waryoba et al. [73] on linear-fill L-PBF and E-PBF Ti-64 and by Fu et. al. [148] on laser-fusion processed Ti-64, variant selection was quantified using relative fractions of inter-variant boundaries present in the α/α' microstructure. Recent EBSD studies on the spot-melted E-PBF Ti-64 [71, 72, 120] reported an occurrence of preferred variant selections in contrast to the linear-melt E-PBF Ti-64 studies [18, 31].

Fig. 3.13 compares the planar variants between the parent and daughter for both the linear and spot melt cases. The goal is to quantitatively identify strong variants emerging in the daughter compared to their parent. First, analysis for the linear melt case (Fig. 3.13a,c) shows that the deviations of parent β {110} variants (from the ideal average volume fraction of 0.16 for each variant set) are quite minimal. More importantly, the deviations of daughter α {0002} variants do not indicate that there is any variant preferably selected out of the parent. In contrast, the spot melt case (Fig. 3.13b,d) shows that the daughter with V(2,8) planar variant is preferably selected out of the parent $(\bar{1}01)_{\beta}$ with $[\bar{2}\bar{2}\bar{2}]_{\beta}$ and $[2\bar{2}2]_{\beta}$. Even though the relatively stronger prevalence of V(2,8), V(5,11), and V(3,6) in the β {110} parent may be related to the strong build texture component of P1 along the build direction, the preference of V(2,8) in the daughter is noticeably stronger.

The directional variants are compared in Fig. 3.14. The Δ (volume fraction) for parent <222> directional variant triplets for the linear melt case (Fig. 3.14a) show slight preference for V(1,2,3) and slight absence for V(7,8,9) compared to the ideal average volume fraction of 0.25. On the contrary, in the spot melt case (Fig. 3.14b) the parent <222> directional variant triplets show slight preference for V(7,8,9) and slight absence for V(1,2,3). The Δ (volume fraction) for daughter directional triplets $<11\bar{2}0>$ (Fig. 3.14c,d) show trends similar to their corresponding parent directional triplets. In the linear melt case, V(7,8,9) is slightly lower than the average fraction (Fig. 3.14c), whereas V(1,2,3) is slightly higher. In the spot melt case, however, almost no trend is observed (Fig. 3.14d). Overall, in both build cases, there is no clear preferred selection of a particular directional variant set that prevails along the entire build height.

The studies by Wang et al. [77] and Farabi et al. [149] on pure Ti attributed the dominance of select variant types to the 'self-accommodation' of the strain energy change during the β to α' martensitic transformation by the formation of three-variant clusters. Wang et al. [77] reported that the lath boundaries formed between two α/α laths in self-accommodated clusters mostly correspond to Type 2 (with 60° misorientation) and Type 4 (with 63.26° misorientation) boundaries. While the study by Wang et al. [77] predicted the prevalence of both Type 2 and Type 4 inter-variant boundaries by the consideration of only volumetric shape strains, Farabi et al. [149] also took into account the shear component of the strain and predicted that the formation of only Type 2 lath boundaries will be favored. The Type 2 boundaries (rotation of 60°/$[11\bar{2}0]$ (angle/axis) from V1) correspond to V2 and V3, whereas the Type 4 boundaries (rotation of 63.26°/$[\overline{10}\ 5\ 5\ \bar{3}]$ from V1) correspond to V5 and V9 in the context of the present study (Table 3.2). Experimental observations by Beladi et al. [57] showed a predominance of Type 4 over Type 2 boundaries in martensitic Ti-64 suggesting a possible influence of composition on the variant selection mechanism. Recent observations made in E-PBF Ti-64 by Haghdadi and co-

workers [72, 120] showed a dominance of Type 2 lath boundaries, while Shao et al. [71] found that both Type 2 and Type 4 boundaries were dominant. The results from the former study align with the predictions made by Farabi et al. [149] and the latter with the predictions made by Wang et al. [77] based on the respective strain accommodation theories. However, a common finding in these studies is that the extent of variant selection was higher for the linear melts than the spot melts. While the results from the current volumetric S-XRD measurements also agree with the other studies on E-PBF [71, 72, 120] by displaying a predominance of BOR variants corresponding to the Type 2 lath boundaries, it differs from the previous studies in that the spot-melt case exhibits a higher degree of preferred variant selection compared to the linear melt across the build height. It should be noted that the BOR variants corresponding to the Type 4 and Type 3 (rotation of 60.83°/$[\overline{1.377}\ \bar{1}\ 2.377\ 0.359]$ from V1) boundaries were also observed in the current study but they cannot be considered as consistently prevalent as Type 2.

3.5. Summary

The variation of phase fraction, β build texture, and α variant selection in a novel spot-melted E-PBF Ti-64 alloy was studied using a high-energy synchrotron x-ray diffraction mapping as a function of the build height. The results were also compared to a conventional linear melted counterpart. The salient conclusions of our study are as follows:

- The β phase fractions in both E-PBF builds were significantly higher than the feedstock powder (3 wt.%). The β phase fraction for the spot-melt sample was about 11 wt.% at the top of the build and gradually decreased to about 8 wt.% near the substrate. This was attributed to the repeated thermal cycling of the build layers during the processing. The linear-melt sample showed an overall higher β phase fraction and also a stronger trend of decreasing β fraction

towards the substrate compared to the spot melt case likely due to a gradual increase in the heat accumulation towards the top of the build in the linear-melt case.

- Spot-melt strategy showed β<100> fiber texture, whereas the linear-melt strategy showed a cube texture about the build axis. The easy growth direction of BCC <001> aligned closely with the build direction consistent with the net maximum thermal gradient (G) being almost parallel to the build direction. The texture intensity in the spot-melt case was relatively uniform across the build height, while the linear-melt case showed a gradual decrease in the overall intensity from the top of the build to the substrate. In terms of both the phase fraction and texture, the novel spot melt produced a more homogeneous microstructure across the build height compared to the linear-melt case.
- The Burgers orientation relationship (BOR) between the parent β phase and the daughter α phase was clearly observed in both spot- and linear-melt samples across the entire build height despite the significant thermal excursions experienced during the build process.
- The daughter α texture intensities mostly inherited the trends set by the parent β texture. The α variant selection was more predominant in the spot-melt than in the linear-melt samples. In the case of spot-melt samples, the planar variant pair of V(2,8), corresponding to $(\bar{1}01)_\beta$ with $[\bar{2}\bar{2}\bar{2}]_\beta$ and $[2\bar{2}2]_\beta$, was most consistently preferred across the build height.

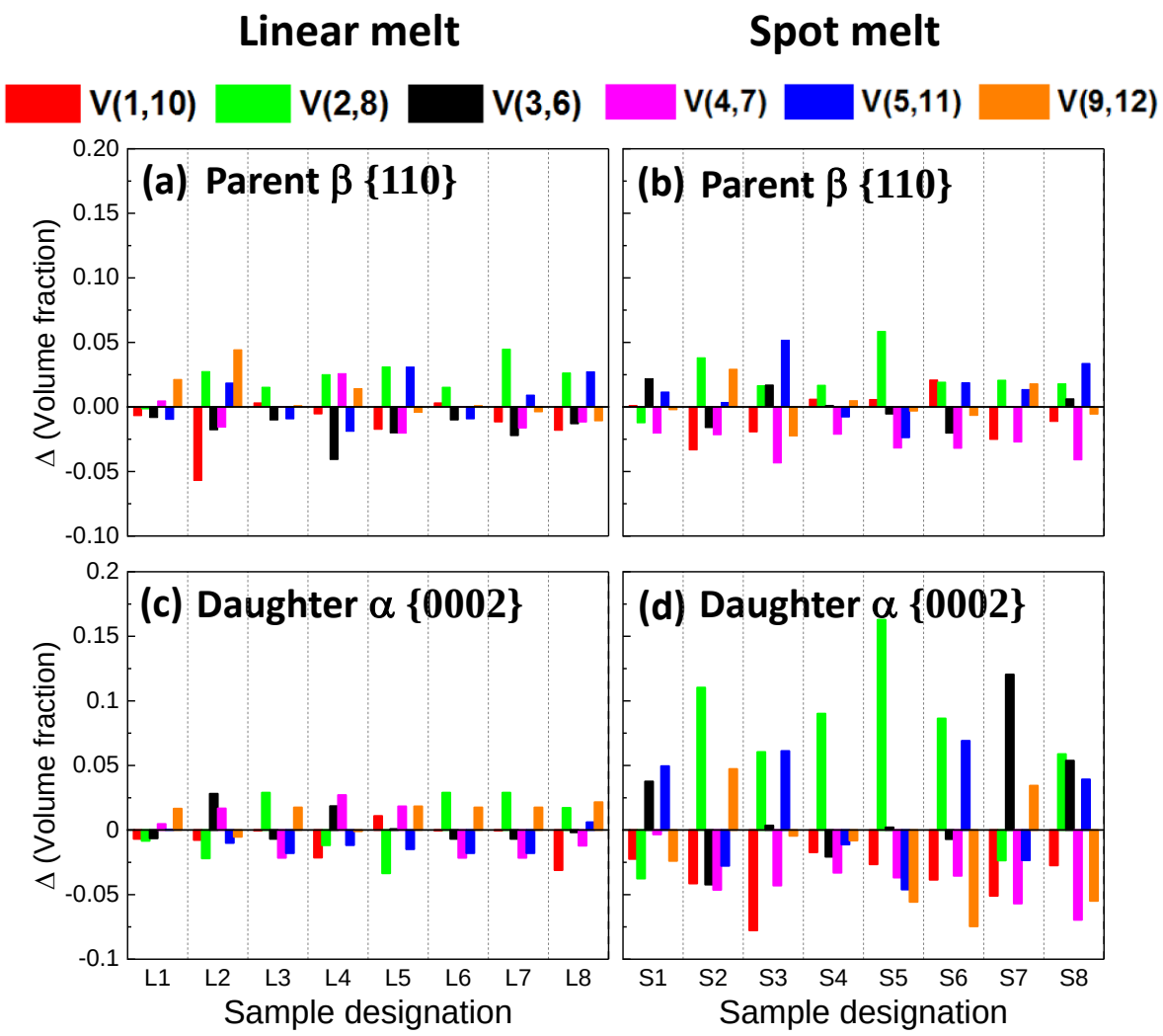

Figure 3.13. Comparison of planar variant selections in the linear (L) and spot (S) melt cases. The deviations (Δ) from the average volume fraction (i.e., 0.16) for each planar variant set are shown as a function of the build height for: the parent β {110} for (a) L vs. (b) S and the corresponding daughter α {0002} for (c) L vs. (d) S.

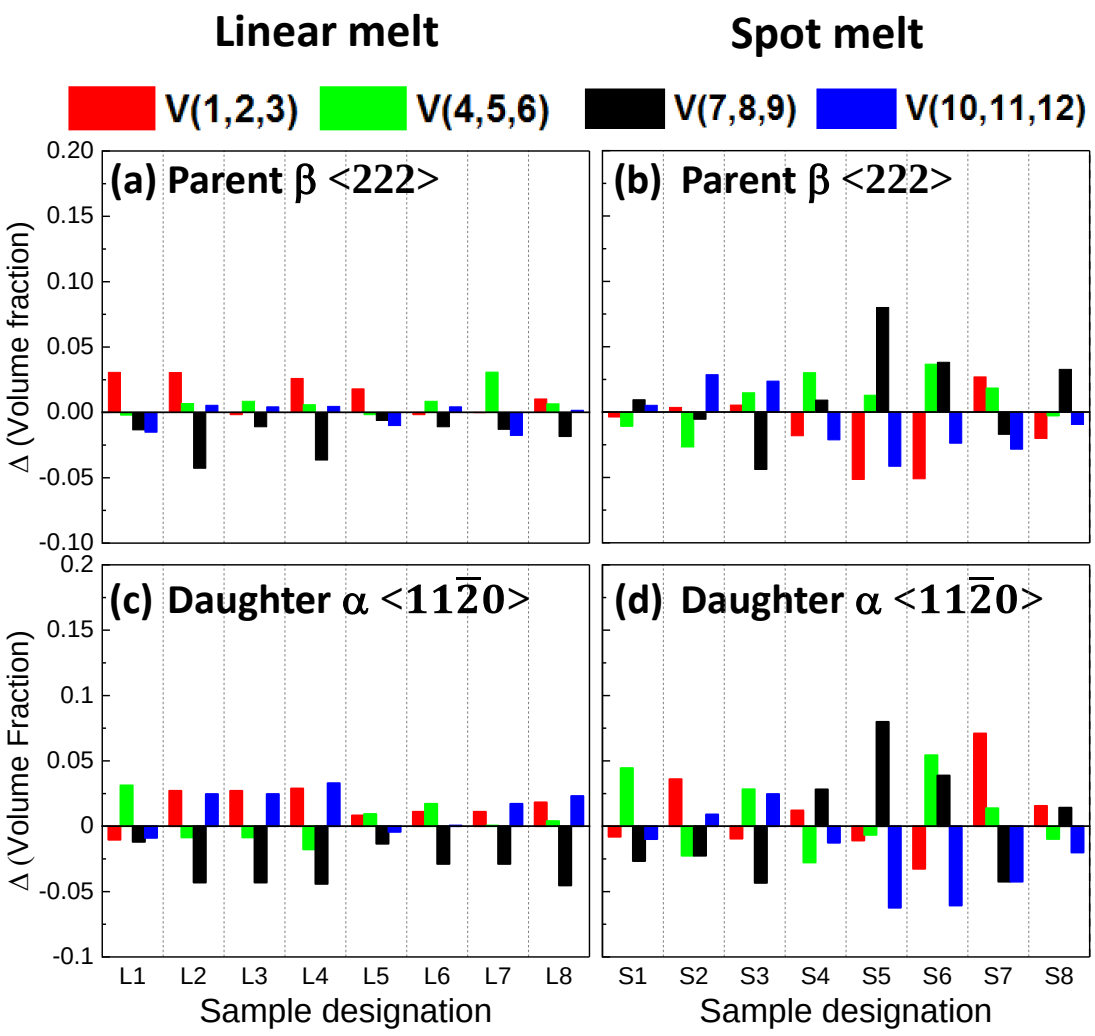

Figure 3.14. Comparison of directional variant selections in the linear (L) and spot (S) melt cases. The deviations (Δ) from the average volume fraction (i.e., 0.25) for each directional variant set are shown as a function of the build height for: the parent β <222> for (a) L vs. (b) S and the corresponding daughter α <11$\bar{2}$0> for (c) L vs. (d) S.

Chapter 4

Effect of laser power on melt-pool characteristics and solidification kinetics in laser spot melting of Ti-6Al-4V

4.1. Introduction

As ascertained in the previous chapter, the novel spot melt produced a more homogeneous microstructure across the build height compared to the linear-melt case both in terms of the phase fraction and texture. Therefore, a detailed study into the physical phenomena operational in the melt pool scale which provide the aforementioned "desirable" microstructure in spot-melt strategy is necessary. Following the literature review in Sec. 2.3.4, the two key physical variables that dictate the solidification microstructure are thermal gradient (G) at and velocity (R) of the liquid-solid interface. The solidification parameters, G and R, are extracted from temperature-field solutions of coupled heat transfer and fluid flow models [20, 21, 24, 106]. These parameters can be further be input into phenomenological models to predict solidification microstructure, enabling microstructure control through process control. However, the above models are calibrated only using the ex-situ microstructure data (for maximum melt pool size) and make assumptions ignoring certain physics in model, which is again not uniform across the modelling studies. Therefore, transient melt pool evolution data from in-situ laser melting experiments is essential in informing these models to obtain high-fidelity simulations.

In this chapter, we probe the transient evolution of the melt pool during the laser spot melting of Ti-6Al-4V alloy for a range of input laser powers. First, the time evolution of melt pool and vapor cavity dimensions during the melting event are examined. Second, the transient nature of the melt pool kinetics during the solidification event is presented. Further, the variation of key metrics extracted from the time evolution plots are compared as a function of input power.

Finally, physical processes operational during the melting and solidification events are ascertained using dimensional analysis and their bearing on solidification microstructure is discussed.

4.2. Experimental details

4.2.1. Material specifications and laser-AM simulator

A Ti-6Al-4V sheet procured from TMS Titanium was ground to a thickness of 500 μm (3 mm (H) X 50 mm (L)) and was used as a substrate for the laser melting experiments. The composition of the substrate is presented in Table 4.1. The Ti-6Al-4V plate was mounted in an argon backfilled (to a pressure almost equal to the atmospheric pressure) chamber with X-ray transparent windows and laser setup for the experiments (herein will be referred to as the laser-AM simulator). A detailed description of the laser-AM simulator is provided in the article by Parab et al. [101]. The laser setup contained a Yb-fiber laser with a maximum power of 540 W and a focal beam size of 50 μm. A laser diameter ($1/e^2$) of 100 μm was used for the present study. The experimental matrix probed in this study involved a range of laser powers (P) from 82 W to 311 W and a constant dwell time (t_d) of 0.5 ms (shown in Table 4.2).

4.2.2. In-situ, dynamic synchrotron x-ray radiography

The in-situ, dynamic synchrotron x-ray radiography was conducted in beamline 32-ID-B at the Advanced Photon Source, Argonne National Laboratory. Polychromatic x-rays ("pink beam") with first harmonic at 24.4 keV (λ = 0.508 Å) with a beamsize of 2 mm × 2 mm were used as a probe for the measurement with a scintillator and high frame-rate camera downstream for recording the x-ray radiographs. A schematic of the setup is shown in Fig. 4.1a. The camera used was a Photron FastCam SA-Z with a spatial resolution of 2 μm and a field-of-view of

Table 4.1. Chemical composition (in wt.%, with Ti in balance) of Ti-6Al-4V sheet procured from TMS Titanium.

Composition (wt.%)				
Al	V	Fe	O	C + H + N + Y
6.11	3.98	0.2	0.16	< 0.02

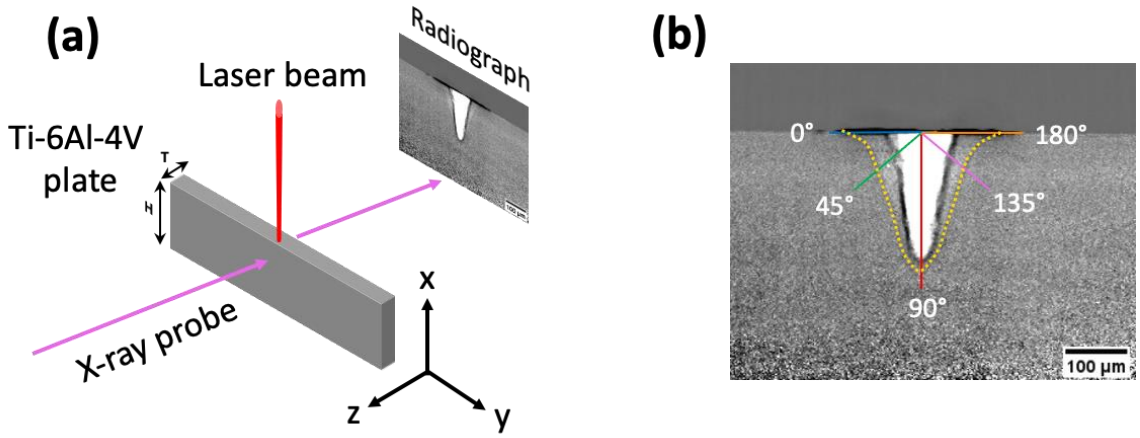

Figure 4.1. (a) Schematic of the x-ray radiography experimental setup at beamline 32-ID-B, APS. The dimensions of the plate are T = 500 μm, H = 3000 μm; (b) Schematic of an x-ray radiograph with the cardinal directions of measurement labelled. Note that the dotted yellow line represents the melt pool boundary.

1 mm × 1 mm. The camera was operated at a frame rate of 70000 Hz (i.e. temporal resolution of 14.28 μs). The dimensions and velocities of both the melt pool and the vapor cavity were measured by tracking the S/L and V/L interfaces, respectively, in the obtained radiographs using the Manual Tracking plugin available in the open-source platform, FIJI [150]. Fig. 4.1b shows a schematic of the angles along which the measurements were taken.

4.2.3. Microstructural characterization

Then the specimen containing a single spot melt was separated and mounted in the conducting Bakelite. Silicon carbide papers starting from 400 grit down to 4000 grit were used to grind the mounted samples. Finally, the mounted samples were polished with 0.05 μm colloidal silica solution. High-contrast SEM backscattered electron (BSE) images of the single melt pool were acquired on each sample. An accelerating voltage of 10kV, beam current of 3.2nA and dwell time of 20 μs was used to achieve sufficient signal-to-noise ratio (S/N) and contrast in the acquired BSE images. An EBSD detector system (EDAX, AMETEK Inc), installed on the Apreo SEM, was used to carry out the EBSD mapping experiments. An accelerating voltage of 20kV and a beam current of 6.4nA as well as a step size of 0.2 μm were chosen for EBSD data acquisition. The EBSD data were processed using TSL OIM software. The IPF maps were color-coded relative to the z-axis crystal orientation. Prior β grain morphology and texture were reconstructed based on the Burgers orientation relationship (BOR) by using a modified MATLAB code.

4.3. Results

4.3.1. Radiography images

Table 4.2 shows the process conditions of each experimental case along with observed melting modes (conduction or keyhole). Fig. 4.2 presents the representative snapshots of key stages during the melting and solidification events for a laser spot melt using experiment case 3 (P = 168 W) as an example. The white region shows the vapor cavity whereas the yellow dotted line is used to outline the melt pool boundary. Figs. 4.2a,b,c show the sequence of occurrences during the melting event starting with the initiation of the melt pool at 57 μs, followed by the vapor cavity initiation at 185 μs and finally, instant at which the laser is switched off at 500 μs. It should be noted that while the laser is switched off at the same instant (t = 500 μs) for all the experiments, the instants at which the melt pool and vapor cavity initiation occur change with the laser power and will be discussed in the later sections. Figs. 4.2d,e,f depict the sequence of occurrences during the solidification of the melt pool after the laser is switched off. Videos of all the experimental cases (as labelled in Table 4.2), including both the melting and solidification events, have been provided in the supplementary section.

4.3.2. Melting event

The positions of the melt pool boundary and vapor cavity boundary during the melting event were measured as described in section 4.1.2 to obtain the quantitative temporal evolution of the liquid-solid interface and vapor-liquid interface.

4.2.2.1 S/L interface

Fig. 4.3 presents the evolution of melt pool characteristics as a function of time, including both the melting and solidification events, for different laser powers. Only the melting event (t <

Table 4.2. List of experimental conditions and the observed melting modes. The corresponding videos in the supplementary section are also pointed out.

Power (W)	Dwell time (ms)	Melting mode	Supplementary video #
82	0.5	Conduction	1
139	0.5	Keyhole	2
168	0.5	Keyhole	3
197	0.5	Keyhole	4
254	0.5	Keyhole	5
311	0.5	Keyhole	6

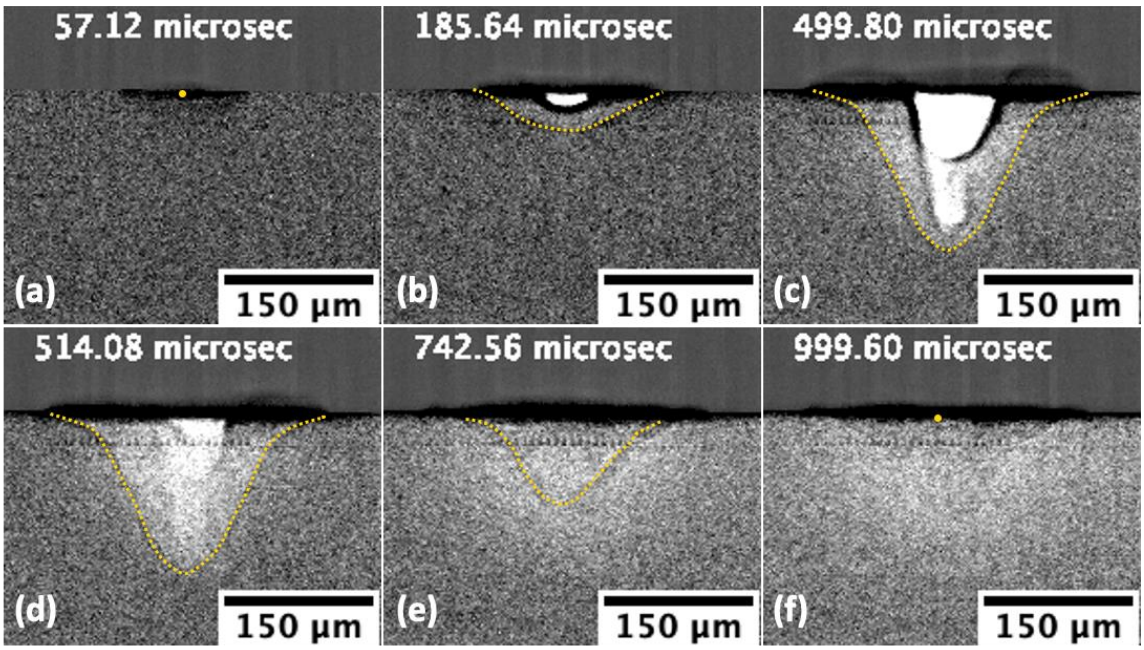

Figure 4.2. Radiographs of salient stages during laser melting and solidification of a spot using experimental case 3 (P = 168 W) as an example - (a) Melting start, (b) Vapor cavity initiation, (c) Laser off, (d) Solidification start, (e) Mid-solidification event ($t_{0.5}$), (f) End of solidification. Note that the yellow dotted line outlines the liquid-solid boundary, and the bright white region is the vapor cavity.

500 μs) is presented here and the solidification event will be presented in section 4.2.3. Fig. 4.3a shows that for the time duration from 0 to 500 μs (i.e. during the melting event), the melt pool area increases with increasing time until the laser is switched off. Similar trends are seen for the melt pool dimensions in the 0° (half-width), 45° (oblique) and, 90°(depth) directions during the melting event, as indicated by Figs. 4.3b,c,d. The conduction (82 W) mode melt pool shows a consistently higher width compared to its depth. On the other hand, the higher power cases begin with a higher width and soon transition into a shape with higher depth due to the emergence and drilling of the vapor cavity (keyholing). These findings are more clearly depicted in Fig. 4.3e showing the time evolution of the aspect ratio (depth divided by half-width) of the melt pool. The horizontal dotted line at D/W = 1 demarcates the width-elongated (D/W < 1) from the depth-elongated (D/W > 1) regimes. The conduction mode melt pools are seen to maintain a steady width-elongated shape with an aspect ratio of 0.4-0.5 throughout the melting duration, after an initial transient increase. In the keyhole cases, however, the initial transient in D/W is seen to be steeper before moving onto a quasi-steady state aspect ratio. This results in a quicker transition from width-elongated to depth-elongated shape with increasing power and is caused by increased intensity of keyhole drilling with an increase in power. The quasi-steady state aspect ratio is also seen to increase with increasing laser power.

Fig. 4.4a,b and c show the time evolution of liquid-solid interface velocity during melting for the 0° (half-width), 45° (oblique) and, 90° (depth) directions, respectively. The velocity peaks initially and exponentially decrease to a near-steady melting state, with a velocity ranging from 0 – 0.25 m/s, until the laser is turned off. The velocity deviates from this trend in the 90° direction for the power cases undergoing keyhole mode melting due to the high dynamic nature of keyhole drilling.

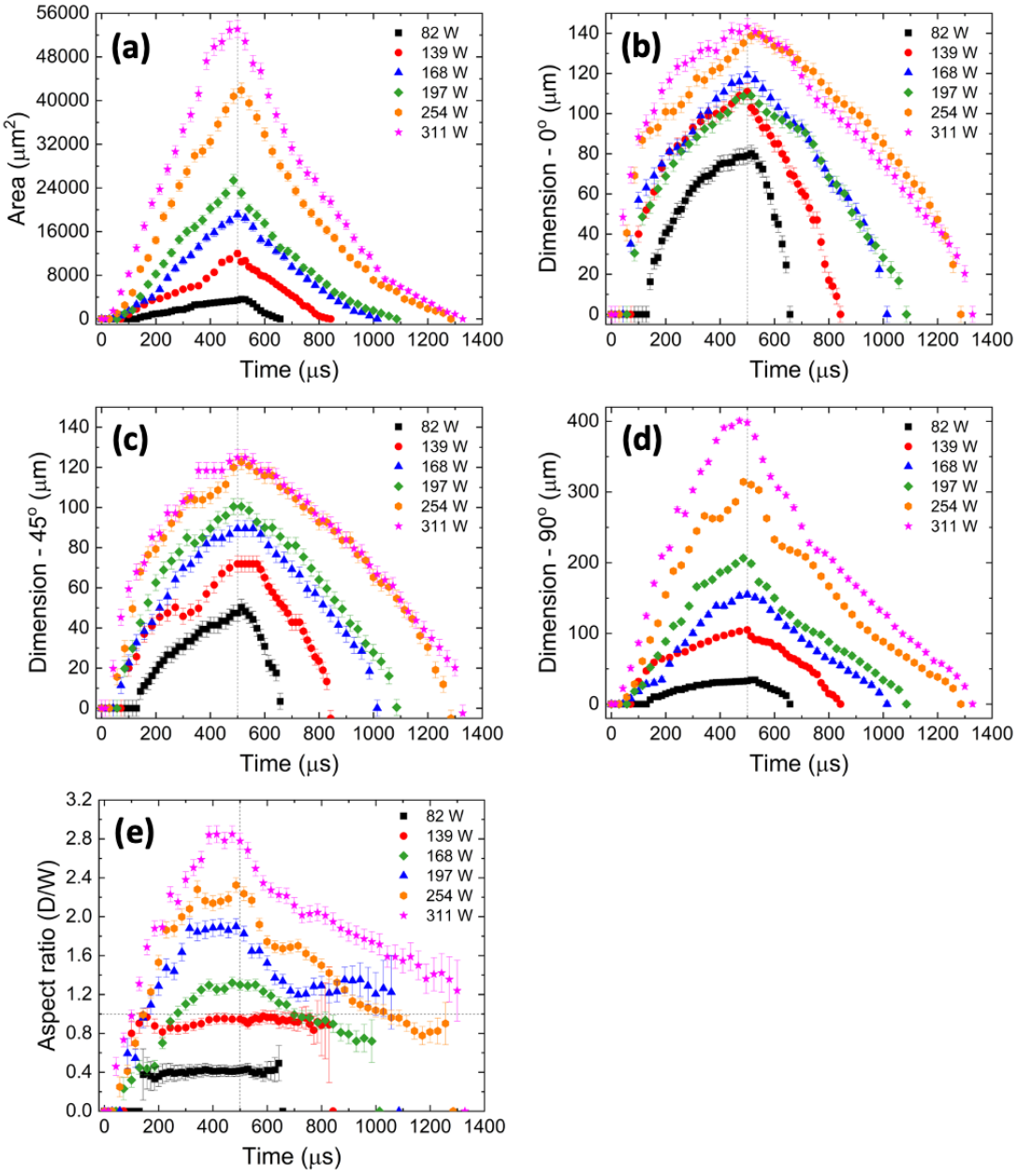

Figure 4.3. Temporal evolution of melt pool characteristics for all the experimental cases - (a) Area, (b) Dimension - 0º, (c) Dimension - 45º, (d) Dimension - 90º, (e) Aspect Ratio (= D/W = Dimension-90º/Dimension-0º). Note that the uncertainty in time axis (= 14.28 μs) is smaller than the symbol width used.

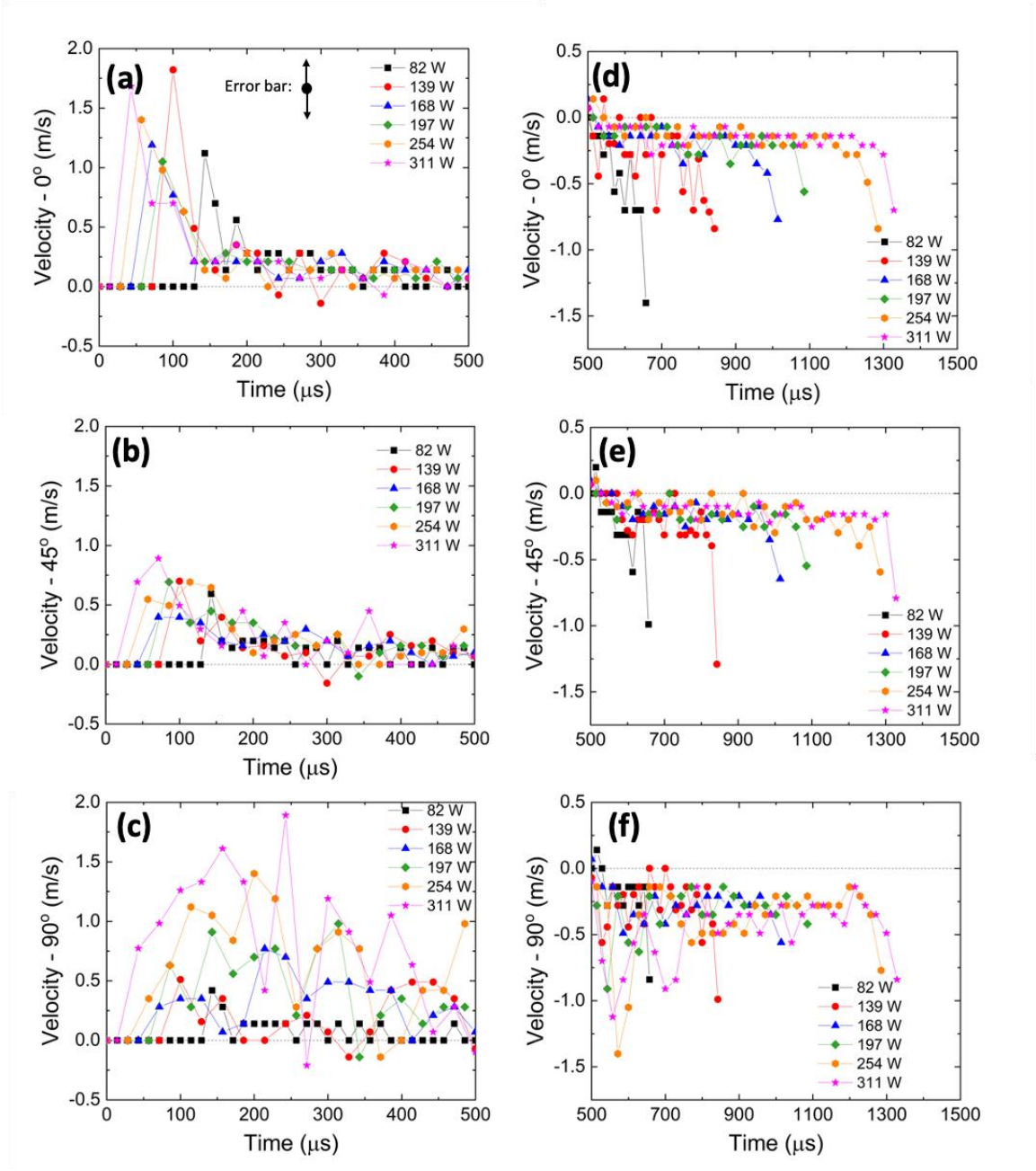

Figure 4.4. Temporal evolution of S/L interface velocity for all the experimental cases during melting in different directions - (a) 0º, (b) 45º, (c) 90º. Temporal evolution of S/L interface velocity for all the experimental cases during solidification in different directions - (d) 0º, (e) 45º, (f) 90º. Note that the error bar for all the velocity measurements (= 0.3 m/s) is shown in (a). Also, uncertainty in time axis (= 14.28 μs) is smaller than the symbol widths used. The same co-ordinate system is used for both melting and solidification and a negative velocity implies the melt pool is shrinking/solidifying.

4.2.2.2 V/L interface

Fig. 4.5 presents the time evolution of the vapor cavity characteristics for different laser powers. Only the melting event ($t < 500$ μs) is presented here since the vapor cavity collapses soon after the laser is switched off. Fig. 4.5a shows that the vapor cavity area shows a general increasing trend with the progression of time with fluctuations in the late stages of the melting event (due to the highly dynamic nature of the keyhole). Fig. 4.5b,c show that the vapor cavity dimensions in the 0° (half-width) and 45° (oblique) directions, respectively, increase initially and fluctuate by a large extent in the later stages of melting. Fig. 4.5d shows that the vapor cavity dimensions in the 90°(depth) direction increases with increasing time and fluctuates to smaller extent compared to the other directions. It can also be seen that the dimensions are significantly higher in the depth direction compared to the other directions. The trends for the vapor cavity growth rate and onset times in the vapor cavity dimensions are similar to the ones shown by the vapor cavity area. The evolution of the vapor cavity aspect ratio (depth divided by half-width) is shown in Fig 4.5e. The vapor cavities are seen to transition to being depth-elongated ($D/W > 1$) quicker with increasing laser power.

Fig. 4.6a,b and c show the time evolution of vapor-liquid interface velocity for the 0° (half-width), 45° (oblique) and, 90° (depth) directions. The velocity reflects the fluctuating behavior of the vapor cavity as seen in the vapor cavity dimensions. The 0° (half-width) and 45° (oblique) directions are seen to fluctuate (expand and shrink) more often than the 90° (depth) direction. Also, the magnitude of the V/L interface velocity is seen to be higher in the 90° (depth) direction.

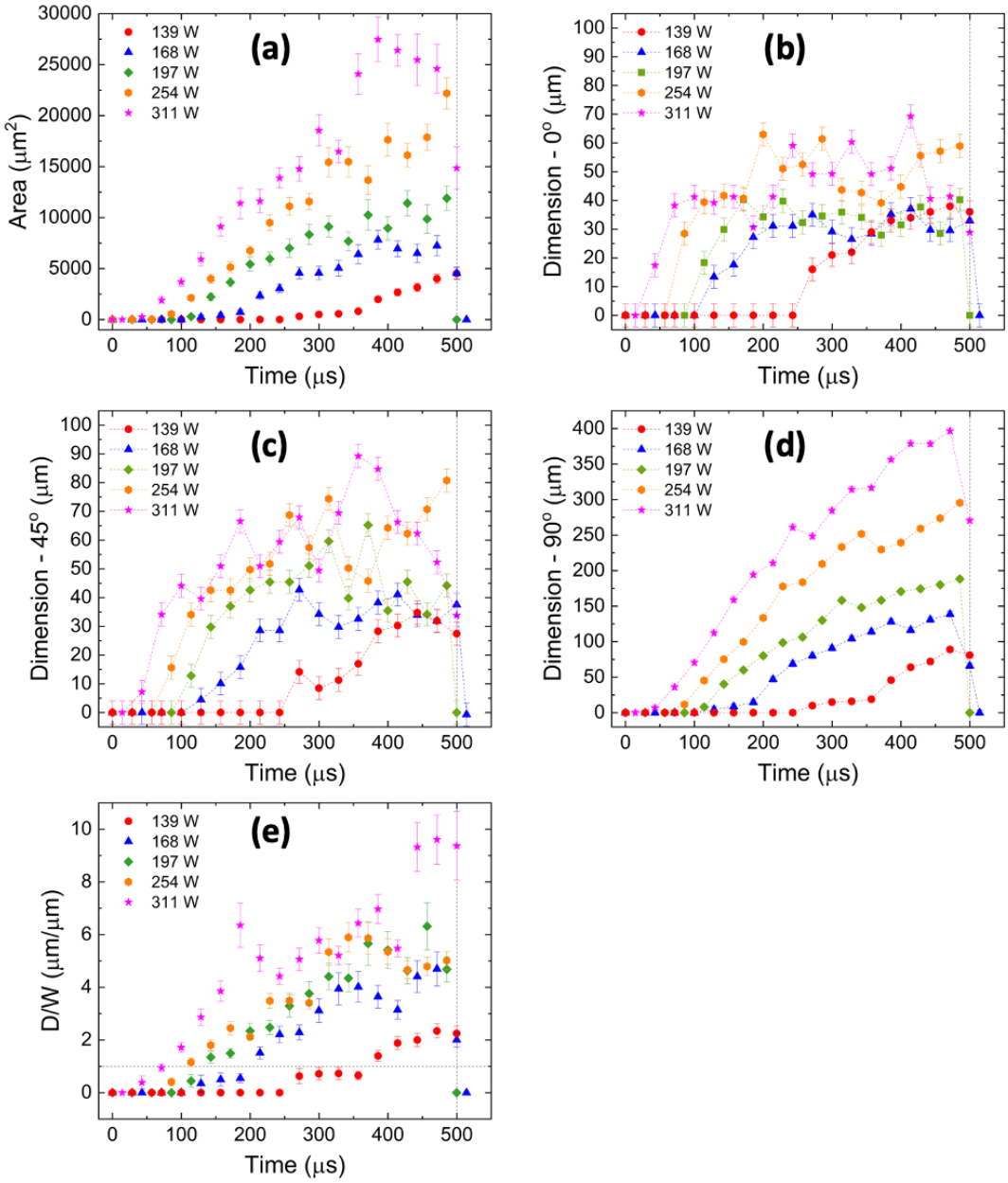

Figure 4.5. Temporal evolution of vapor cavity characteristics for all the experimental cases - (a) Area, (b) Dimension - 0º, (c) Dimension - 45º, (d) Dimension - 90º, (e) Aspect Ratio (= D/W = Dimension-90º/Dimension-0º). Note that the uncertainty in time axis (= 14.28 μs) is smaller than the symbol width used.

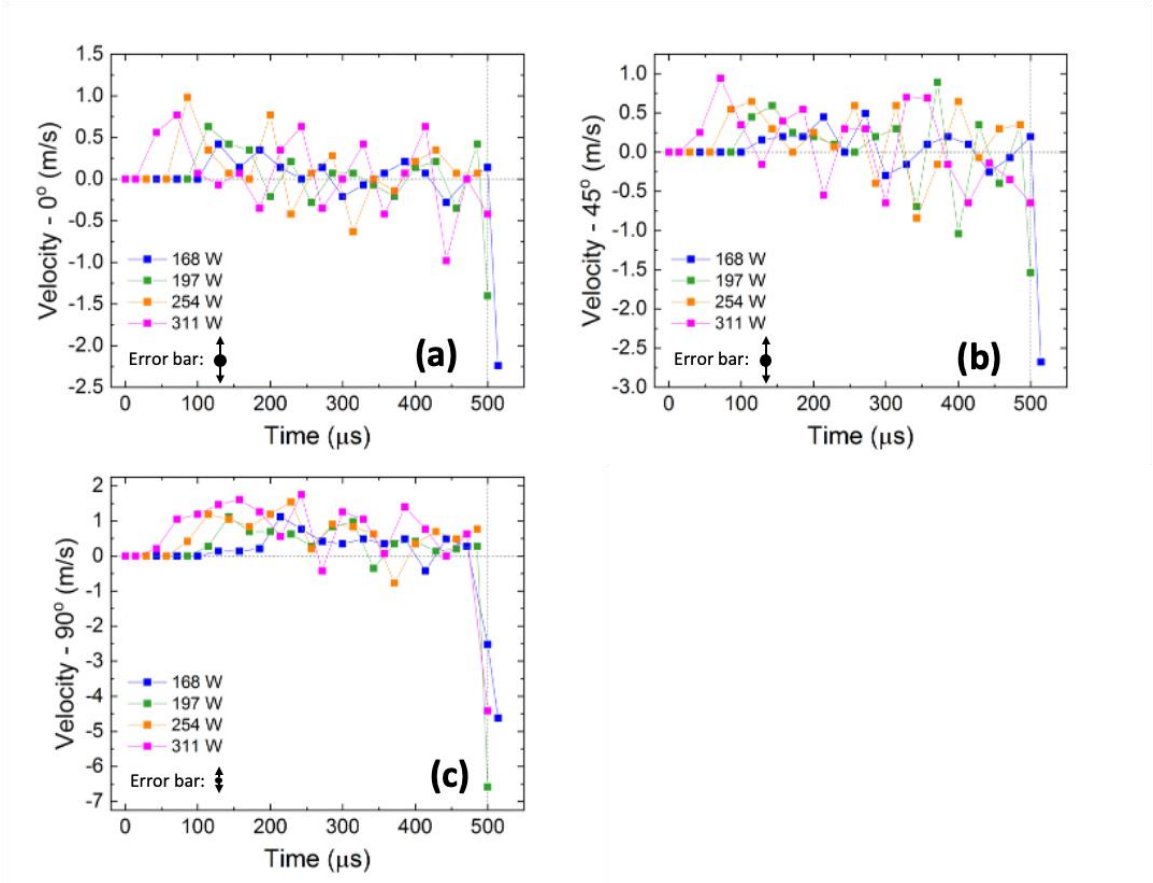

Figure 4.6. Temporal evolution of L/V interface velocity for all the experimental cases during melting in different directions - (a) 0º, (b) 45º, (c) 90º. Temporal evolution of L/V interface velocity for all the experimental cases during solidification in different directions - (d) 0º, (e) 45º, (f) 90º. Note that the error bar for all the velocity measurements (= 0.3 m/s) is shown for each figure. Also, uncertainty in time axis (= 14.28 μs) is smaller than the symbol widths used. The same co-ordinate system is used for both melting and solidification and a negative velocity implies the melt pool is shrinking/solidifying.

4.3.3. Solidification event

The time evolution of melt pool characteristics during the solidification event as shown in Fig. 4.3 for t > 500 μs is presented here. Fig. 4.3a shows that for the time after the laser is switched off (t = 500 μs), the melt pool area decreases non-linearly to zero with a similar trend for all laser powers. It can also be qualitatively seen that the solidification time increases with increasing laser power. Figs. 4.3b,c,d show that the melt pool dimensions in the 0° (half-width), 45° (oblique) and, 90°(depth) directions decrease non-linearly to zero with a different trends. Fig. 4.3e shows the aspect ratio of the solidifying melt pool decreases with time. However, the aspect ratio of the conduction mode melt pool is seen to decrease significantly less than that of the keyhole mode melt pools.

Fig. 4.4d,e and f show the time evolution of liquid-solid interface velocity during solidification for the 0° (half-width), 45° (oblique) and, 90° (depth) directions, respectively. The magnitude of the melt pool velocities are seen to range from 0.1 – 1 m/s. For the keyhole mode cases, the time evolution of velocity in the 0° (half-width) direction suddenly increases during the start of solidification, followed by a steady-state and a sudden increase at the end of solidification. The 45° (oblique) and 90° (depth) directions follow the same trend, except the initial stages where a pore results in the acceleration of the melt pool velocity in the latter direction. However, for the conduction mode melt pool (82 W), the solidification velocity in all directions increases non-linearly with time.

4.3.4. Ex-situ microstructure characterization

Fig. 4.7a presents the SEM-BSE image of the melt pool in the keyhole (168 W) mode. Three distinct regions can be identified due to their contrast – the melt pool/FZ (lighter contrast), heat-affected zone/HAZ (medium contrast) and Ti-64 substrate (dark contrast). The substrate

shows a typical rolled Ti-64 microstructure containing equiaxed α interspersed with β grains (thin and white features). The HAZ microstructure is similar to the substrate with thicker β grains. Fig. 4.7b, c, and d show the phase maps of the substrate, FZ and HAZ, respectively. The microstructures are seen to consist of retained β area% of 3.3%, 4.3% and 16% in the case of substrate, FZ and HAZ, respectively.

Fig. 4.8 shows the α-phase IPF-Y (Y = build direction) maps, representative pole figures and boundary misorientation distributions corresponding to each microstructural region in the case of the keyhole (168 W) melt pool. From the IPFs, it can be observed that the α-phase morphology is lath-like in the FZ and HAZ regions, whereas globular in the substrate. The α pole figures show a (0002) texture in build direction for all three regions. The misorientation angle distribution shows peaks around 60 degrees for the FZ and HAZ, whereas the substrate misorientation angle distribution shows a peak below 10 degrees (latter can be attributed to low angle grain boundaries). Additionally, the intensity of the peaks around the 60-degree misorientation is higher in the case of FZ than the HAZ.

Fig. 4.9 shows the retained β-phase IPF-Y maps and representative pole figures corresponding to each microstructural region in the case of the keyhole (168 W) melt pool. The β pole figures for HAZ and substrate show a (110) texture in build direction, whereas the FZ shows a tilted fiber-like texture. Fig. 4.10 shows the reconstructed β-phase IPF-Y maps and representative pole figures corresponding to each microstructural region in the case of the keyhole (168 W) melt pool. Note that substrate does not undergo an α-to-β transformation during the spot melting, therefore, resulting in no reconstructed β-phase. From the IPFs, it can be observed that the β-phase morphology is columnar in the FZ and more globular in the HAZ. The β pole figures for both the FZ and HAZ show a (110) texture in build direction. The number

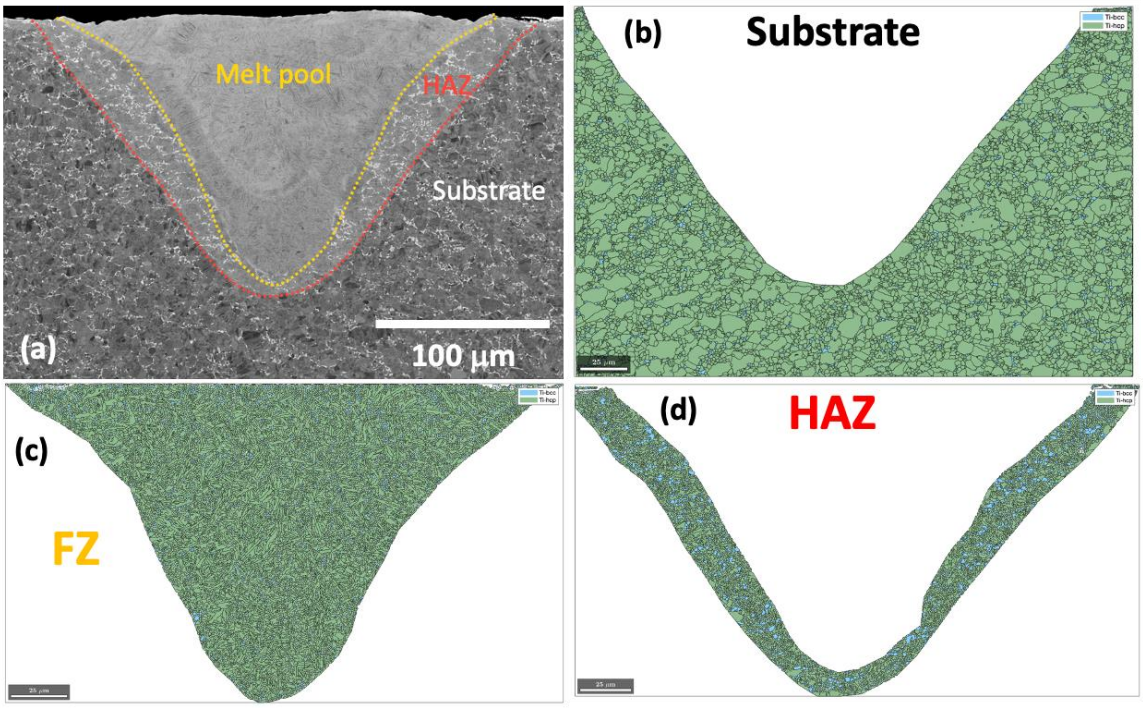

Figure 4.7. (a) SEM-BSE micrograph of the keyhole mode (168 W) melt pool depicting the three microstructural regions – Melt pool/FZ, heat-affected zone/HAZ and the substrate. Phase maps of the three microstructural regions - (b) Substrate, (c) FZ, (d) HAZ depicting the α phase in green and β phase in blue.

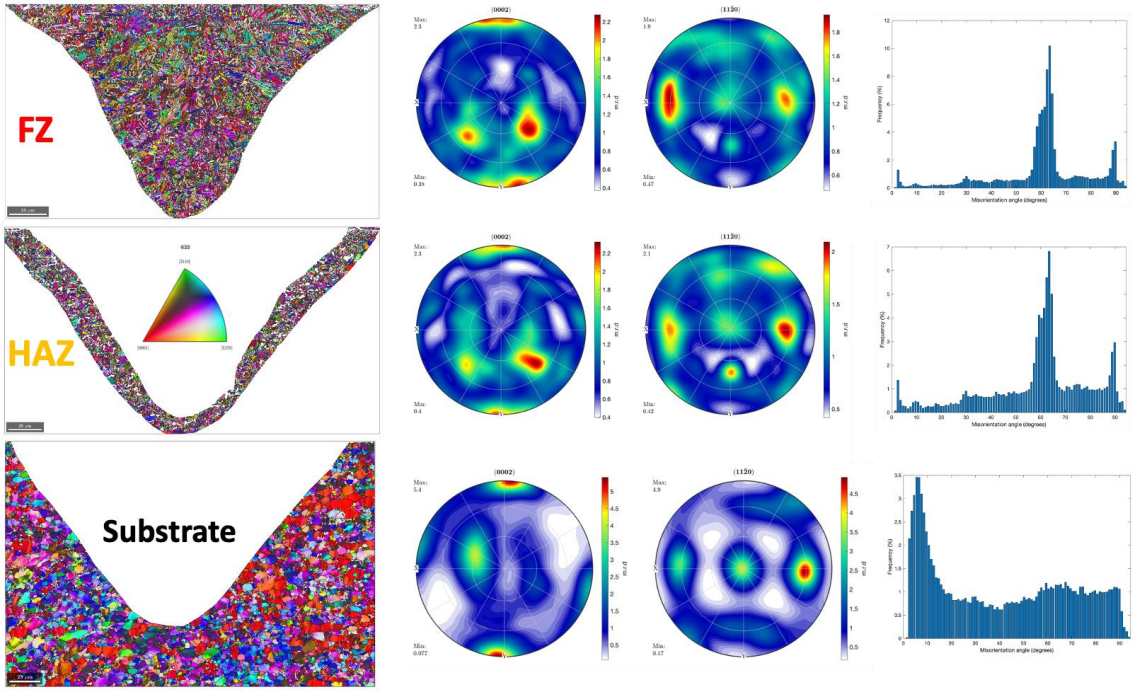

Figure 4.8. α-phase IPF-Y (Y = build direction) maps, representative pole figures and boundary misorientation distributions corresponding to each microstructural region in the case of the keyhole (168 W) melt pool

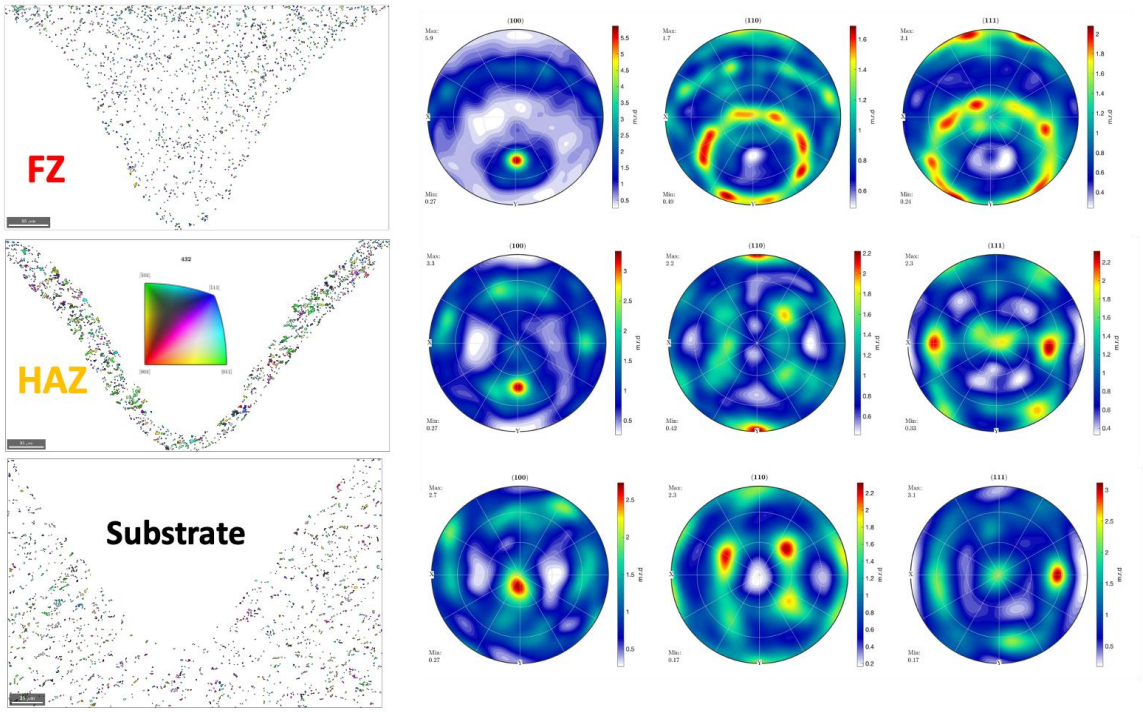

Figure 4.9. Retained β-phase IPF-Y maps and representative pole figures corresponding to each microstructural region in the case of the keyhole (168 W) melt pool

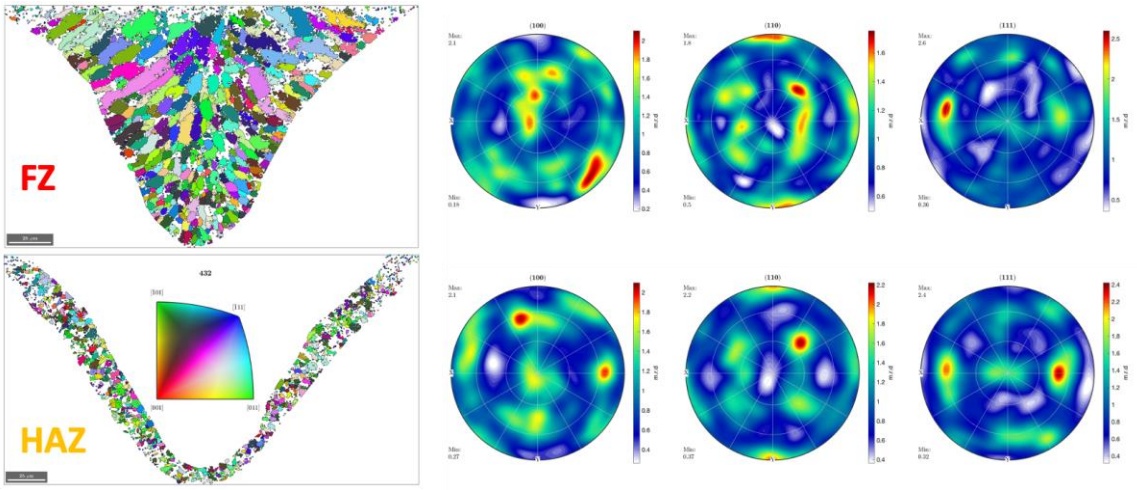

Figure 4.10. Reconstructed β-phase IPF-Y maps and representative pole figures corresponding to each microstructural region in the case of the keyhole (168 W) melt pool.

Table 4.3. The number-average values of the characteristics of the α-phase, retained β-phase and reconstructed β-phase for each microstructural region in the keyhole mode (168 W) melt pool.

Phase	Characteristic	FZ	HAZ	Substrate
α-phase	Width (μm)	0.87	0.83	1.52
	Aspect ratio	1.78	1.63	1.67
Retained β-phase	Width (μm)	0.71	0.88	0.84
	Aspect ratio	1.47	1.49	1.8
Reconstructed β-phase	Width (μm)	1.53	1.27	-
	Aspect ratio	1.65	1.55	-

average values of the characteristics of the α-phase, retained β-phase and reconstructed β-phase for each microstructural region are presented in Table. 4.3.

Fig. 4.11a and b present the SEM-BSE image of the melt pool in the conduction (82 W) mode as a whole (showing all the microstructural regions) and enlarged image of the melt pool center inside the FZ, respectively. Fig. 4.11b shows the α' (or α) to be acicular in nature. Fig. 4.11c shows the α-phase IPF-Y corresponding to the Fig. 4.11a. Fig. 4.11d and e show the reconstructed β-phase IPF-Y maps and representative pole figures corresponding to the melt pool region shown in Fig. 4.11b. From the IPFs, it can be observed that the β-phase morphology is columnar. The β pole figures show a (110) texture in build direction.

4.4. Discussions

4.4.1. Melting event

4.4.1.1. Variation of melt pool and vapor cavity kinetics with laser power

Fig 4.12a shows the variation of melt pool and vapor cavity initiation times with laser power, extracted from their respective area evolution plots in Fig. 4.3a. It is seen that the melt pool initiation time decreases with increasing laser power. This observation can be justified based on the presence of surface oxide layer in Ti-6Al-4V [151, 152] and its proposed "breaking" during laser incidence. Inspite of the decrease in the absorptivity (to a lower constant value) due to the presence of the surface oxide layer, an increase in incident laser power results in a concurrent increase in absorbed laser power and consequently decreases the melting initiation time. The trend observed for the vapor cavity initiation can also be attributed to the increase in absorbed laser power with increasing incident power. Following King et al. [91], the absorbed energy density is $AP\tau/\pi\sigma^2\sqrt{D\tau}$ where A is the absorptivity of the material, P is the incident laser

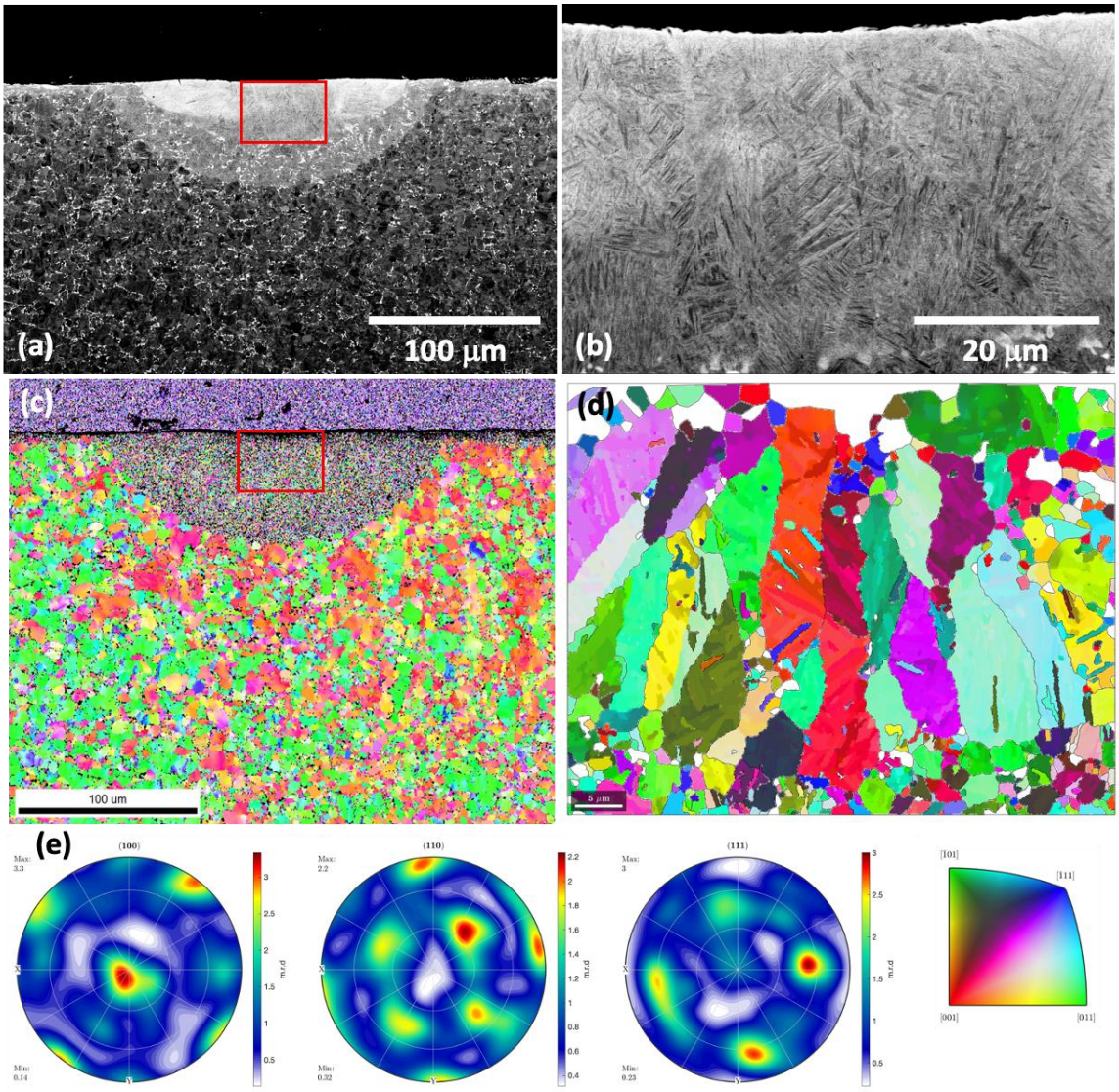

Figure 4.11. (a) SEM-BSE micrograph of the conduction mode (82 W) melt pool consisting of all three microstructural regions; (b) Enlarged BSE image of the melt pool center; (c) α-phase IPF-Y corresponding to (a); (d), (e) Reconstructed β-phase IPF-Y and pole figures corresponding to (b).

power, τ is the dwell time, σ is the laser diameter and D is the thermal diffusivity of the material. Further, King et al. state that the conduction to keyhole transition occurs when the absorbed energy exceeds approximately 6 times the enthalpy at melting (h_s), which is a constant for given material. This implies that for higher laser powers (P), the dwell time (τ) required to cross the keyhole threshold is lower (for constant absorptivity). Additionally, it has been observed that the absorptivity (A) increases with increasing laser power [132], which further supports the above argument. Fig. 4.12b shows the variation of linear melting rate (extracted from Fig. 4.3a) with changing laser power. The linear melting rates increase with increasing laser power. This linear melting rate is the rate of increase of the sum of the vapor cavity, melt sliver around the vapor cavity and the "missing" volume of the melt pool. The processes which can account for the "missing" volume of the melt pool are – (a) evaporation from vapor cavity [153], (b) melt displacement to the surface of the melt pool [154], and (c) explosive melt expulsion [155]. For the laser conditions used in the present study, melt expulsion and evaporation contribute very less to this discrepancy and therefore, melt displacement accounts for most of it.

The variation of maximum dimensions of the melt pool and vapor cavity with laser power are presented in Fig. 4.12c. It is seen that an increase in power results in a steeper increase in the depth direction than width. A ratio of the maximum vapor dimension to maximum melt pool dimension from Fig. 4.12c is used to calculate the percent vapor in different directions in Fig. 4.12d. It is seen that the depth has a significantly higher percent of vapor than the width and the percent vapor in both directions increases with increasing laser power. The above observations can be explained by the fact that the primary laser absorption being in the depth direction and absorption of secondary reflections being in the width direction.

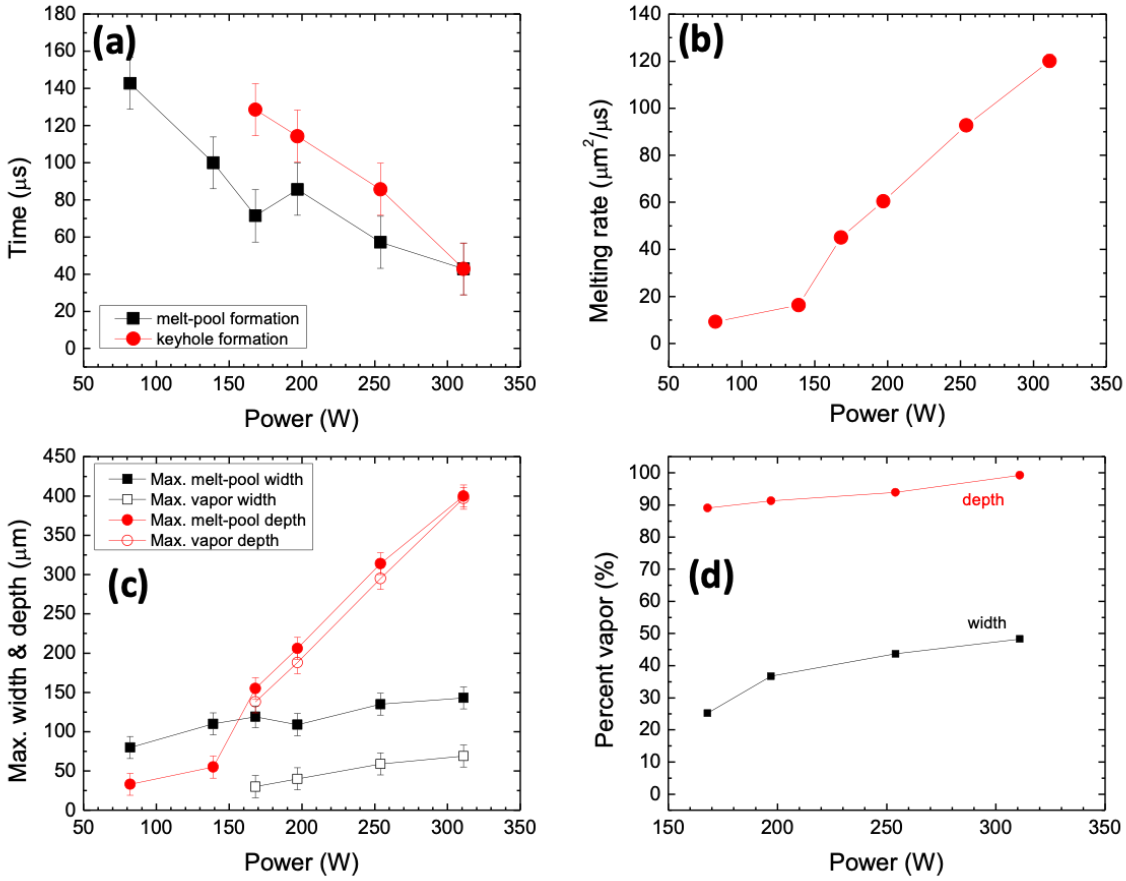

Figure 4.12. Variation of characteristic metrics of melting kinetics with laser power – (a) Melt-pool initiation time and keyhole initiation time, (b) linear melting rate, (c) maximum dimensions of the melt pool and vapor cavity, (d) Percent vapor in the width (0^o) and depth (90^o) direction.

4.4.1.2. Fluid flow and heat transfer during laser melting

The driving forces that dictate the motion of the fluid in the conduction mode melt pool are buoyancy and surface tension which oppose the viscous forces [20, 21, 24, 106]. The flow due to the buoyancy force arises due to the spatial variation of liquid metal density resulting from a temperature variation in the bulk of the melt pool. On the other hand, a spatial variation of temperature on the surface of the melt pool resulting in a change of melt surface tension from the center to the outer edge of the melt pool is the cause for the flow due to the surface tension force (also known as Marangoni flow). The relative significance of the driving forces with respect to the opposing viscous forces during fluid flow can be described using dimensionless numbers, as shown in Eqs. 1 and 2. The Grashof number (Gr) is used to determine the ratio of magnitude of the buoyancy force to the viscous force (Eq. 1), whereas the surface tension Reynolds number is used to determine the ratio of magnitude of the surface tension force to the viscous force (Eq. 2). The relative importance of the driving forces during fluid flow can be described using the ratio of the above dimensionless numbers, Ma and Gr, as shown in Eq. 3.

$$Gr = \frac{g\beta L_B^3 \Delta T \rho^2}{\mu^2} \quad \cdots\cdots\cdots (1)$$

$$Ma = \frac{\rho L_R \Delta T \left|\frac{d\gamma}{dT}\right|}{\mu^2} \quad \cdots\cdots\cdots (2)$$

$$R_{S/B} = \frac{Ma}{Gr} = \frac{L_R \left|\frac{d\gamma}{dT}\right|}{g\beta L_B^3 \rho} \quad \cdots\cdots\cdots (3)$$

where g is the acceleration due to gravity, β is the thermal expansion coefficient, ΔT is the temperature difference between the peak temperature and solidus temperature, L_B is the characteristic length for the buoyancy force (approximated as one-eighth of the melt pool full-width), ρ is the density of the liquid alloy, μ is the viscosity of the liquid alloy, L_R is the

characteristic length of the melt pool (approximated as half of the melt pool full-width) and ($d\gamma/dT$) is the temperature gradient of surface tension for the alloy system.

First, using the thermophysical properties of Ti-6Al-4V alloy listed in Ref. [156] and a conservative estimate for ΔT of 500 K, the $R_{S/B}$ calculated at the instant just before the laser is turned off is equal to 7.4×10^6 implying that melt pool flow is mainly driven by the surface tension force and to a much less extent by the buoyancy force. Since the dominant driving force for the fluid flow is the surface tension force, the order of magnitude of the maximal velocity can approximated using the following equation

$$u_m^{3/2} \approx \left|\frac{d\gamma}{dT}\right| \frac{dT}{dR_W} \frac{R_W^{1/2}}{0.664\rho^{1/2}\mu^{1/2}} \quad \cdots\cdots\cdots (4)$$

where R_W is melt pool radius (i.e. half of the melt pool full-width) and dT/dR_W is the average thermal gradient in the weld pool (5×10^6 K/m). From Eq. 4, the maximal velocity is estimated to be of the order of 5 m/s.

The significant amount of fluid flow in the melt pool from the above analysis points to convection having a considerable effect on the heat transfer out of the melt pool. In this regard, the relative importance of heat transfer by heat conduction and convection can be evaluated using the Peclet number (Pe), defined as follows

$$Pe = \frac{Heat\ convection}{Heat\ conduction} = \frac{u\rho C_p L_R}{k} \quad \cdots\cdots\cdots (5)$$

where, u is the average liquid velocity (taken here as 5 m/s following u_m). The calculated Pe at the instant just before the laser is turned off is approximately equal to 35. This implies the melt pool convection is the dominant mode of heat transfer during the melting event and therefore, significantly affects the melt pool geometry.

The above estimations are only valid for a conduction melt pool as evaporation recoil pressure plays a stronger role in liquid metal flow than the surface tension and hydrostatic pressures in keyhole melt pools as shown in Refs. [92, 107].

4.4.2. Solidification event

4.4.2.1. Variation of solidification kinetics with laser power

In the numerical simulations on spot melts by Debroy et al. [20, 21, 24, 106] in multiple alloys, it has been seen that the R follows an increasing trend as the solidification progresses. However, one of their shortcomings is that the temperature solutions are used to pinpoint the L/S boundary and there is no undercooling considered for solidification. This is overcome in a study by Katayama and Matsunawa [96] on Al-Mg alloys where they include the effect of latent heat and different micro-segregation models (with a caveat that flow is ignored, but its effect on heat transfer is included using a higher effective thermal diffusivity in the melt pool). It is seen that the including latent heat in the numerical model results in a three-stage variation in solidification velocity – initial increase, near steady state and final increase. The present experimental findings shown in Figs. 4.4d,e,f also follow a three-stage evolution of R. This implies that the consideration of latent heat and micro-segregation is very important in modelling the melt pool development during solidification.

Debroy et al. [20, 21, 24, 106] report a higher R in the 0º direction than the 90º direction in their simulations on conduction mode melt pools. Also, Zhao et al. [102] report a higher R in the 90º direction in their experimental study on keyhole spot melt. Our experimental findings agree with the above results for conduction and keyhole melt pools, respectively. To further investigate the direction dependent kinetics during solidification, the time evolution of fractional decrease in dimension ($\Delta d/d_{max}$) for 0º, 45º and 90º is shown in Fig. 4.13. Here we can see that for

the conduction mode, all the directions follow the same trend with the same "incubation time" and $t_{0.5}$ (time for half of solidification to be completed). However, as the laser power increases, the 90º direction (depth) has a lower "incubation time" and $t_{0.5}$, while the 0º and 45º directions both exhibit slower kinetics. This implies that the solidification kinetics along the 90º direction (along the depth) is faster in a keyhole melt pool. A likely cause for this observation is the higher rate of conduction through the substrate due to the relatively hotter liquid present at the bottom of the keyhole than the top.

Fig. 4.14a shows the variation of steady state velocity with laser power. The steady state velocity decreases with increasing power and reaches a near constant value at higher powers. This observation is in line with the empirical observations in welding literature which state that smaller melt pools have a higher cooling rate.

4.4.2.2. Rationalization of solidification microstructure

Justification for the position of the HAZ: In section 4.3.4., the region with the lighter contrast was claimed to be the heat-affected zone (HAZ) i.e. the region which experiences temperatures between the β-transus and solidus. To justify this claim, an analytical heat transfer model (considering only heat conduction) given by Grong [157] was used.

According to the Grong model, the temperature of any point at a distance, r, from the point of laser incidence is expressed as Eqn. 6, shown below

$$(T - T_0) = \frac{2Q}{\rho C_p (4\pi\alpha t)^{3/2}} e^{-(\frac{r^2}{4\alpha t})} \quad \cdots\cdots\cdots (6)$$

Where, T_0 is the room temperature, Q is the absorbed energy (= incident power * absorptivity * dwell time), t is the dwell time, ρ is the density of Ti64 (= 4430 kg/m^3), C_p is the specific heat of Ti64 (= 546 J/kg/K) and α is the thermal diffusivity of Ti64 (= 2.9*10^{-6} m^2/s). Note that the

material properties were acquired from the reference [158]. The edge of the FZ (i.e. melt pool width) was used to calibrate the system and obtain an absorptivity value of about 0.5.

Using Eqn.6, it was determined that the isotherm of about 1150K coincides with the outer edge of the "light contrast" region. The outer edge of the HAZ should correspond to the β-transus i.e. 1263 K (by definition), therefore, meaning that the HAZ should be narrower than that seen in the microstructure . Considering the Grong model's limitation of not taking into account other modes of heat transfer (convection, radiation) and the fact that higher heating rates necessitate superheating over the equilibrium for the α-to-β transformation [159] (i.e. HAZ will be wider than that expected with equilibrium value), we can say that the lighter contrast region is indeed the HAZ.

Area % of retained-β in the phase plots: Phase plots of the keyhole mode melt pool in Fig. 4.7 show that the HAZ has a higher retained-β fraction compared to the FZ and substrate. This can be justified using the fact that the cooling rate at the FZ > cooling rate at the HAZ and a lower cooling rate might lead to the transformation taking the diffusional route, rather than displacive, resulting in a mixed microstructure of (α′+α+β) as has been seen in E-PBF Ti64 by Galarraga et al. [33].

Variant selection in the α-phase: The misorientation angle distribution in Fig. 4.8. show peaks around 60 degrees for the FZ and HAZ. This corresponds to specific intervariant boundary misorientations and is indicative of Type II and IV variants [57, 77] being preferably selected during the β-to-α transformation. Additionally, the intensity of the peaks around the 60-degree misorientation is higher in the case of FZ than the HAZ. This implies that the HAZ region has lesser fraction of α transformed as martensite than the FZ and also, supports the mixed microstructure hypothesis used to justify the area % of retained-β. Also, the Burgers orientation

relationship is seen to be followed during the α-β transformation since the β(110) and α(0002) directions lineup along the build direction.

Crystallographic texture in the β-phase: In both the conduction and keyhole mode melt pools, the β pole figures show a (110) texture along the build direction rather than the more commonly seen (100) easy-growth texture. One (or both) of the plausible causes listed here might be at play: (i) Epitaxial solidification – The retained-β and reconstructed-β both show the same texture meaning that most locations stray grain nucleation does not occur, except in the case of depth direction in 168 W case where we do see near equiaxed β-grains
(ii) Melt pool shape – The easy growth is occurring perpendicular to the S/L interface and the interface itself is inclined at 45 degrees to the build direction resulting in the (110) pole being parallel to the build direction.

Estimation of thermal gradient using feature size: As detailed in the background in Sec. 2.3.4., the combined forms of the solidification parameters, (G × R) and (G/R) dictate the size and morphology of the solidified substructure, respectively [110]. Classic solidification and welding literature used the microstructure size to back-calculate the cooling rate through empirical, alloy-specific relations. In one such study, Broderick et al. [160], found that the β grain size (L) decreases with increasing cooling rate ($\dot{T}$) and is given by the equation:

$$L = 3.1 \times 10^{6}\, \dot{T}^{-0.93} \quad \ldots\ldots\ldots (7)$$

The average grain width calculated from the reconstructed β-grains from the EBSD pattern are 1 μm and 1.5 μm for 82 W and 168 W, respectively. Using these values for L in Eqn. 7, we get 4.5×10^6 K/s and 2.5×10^6 K/s for 82 W and 168 W, respectively. We also know that as an approximation we can use, $\dot{T} = \mathrm{G} \times \mathrm{R}$. From Fig. 4.14, we have R = 0.4 m/s for 82 W and 0.2 m/s for 168 W. This gives us the average G = 11.25×10^6 K/m for 82 W and 12.5×10^6 K/m

for 168 W. As expected, these G-R co-ordinates are in the fully columnar region in the G-R map for Ti-6Al-4V (replotted from [29]).

4.5. Summary

The temporal evolution of melt pool and vapor cavity dynamics, and solidification kinetics during spot melting was studied as a function of laser power. The ex-situ microstructural characterization was performed and correlated with the solidification kinetics. The salient results of the study are as follows:

- The melt pool and vapor cavity initiation time decreased with increasing laser power. The melt pool initiation time was rationalized based on the time taken to break the surface oxide layer and the vapor cavity initiation were explained using the conduction-to-keyhole criterion.
- The linear melting rate was seen to increase with increasing laser power. Additionally, the percentage of vapor cavity in each direction was also seen to increase with increasing power. The percent vapor in the depth direction was much greater than the width direction. This was attributed to the primary laser absorption being in the depth direction.
- Dimensionless numbers were used to determine the driving forces for fluid flow and dominant heat transfer mechanism. The fluid flow in the conduction melt pool is mainly driven by Marangoni (surface tension gradient) force. The dominant heat transfer mechanism in the melt pool was convection.
- The melt pools showed three stages during solidification – initial increase, steady-state and final-increase. The steady state velocity was seen to decrease and reach a near constant value with increase in laser power. Also, the solidification kinetics for keyhole melt pools was seen to be faster in the 90º direction than the 0º and 45º directions.

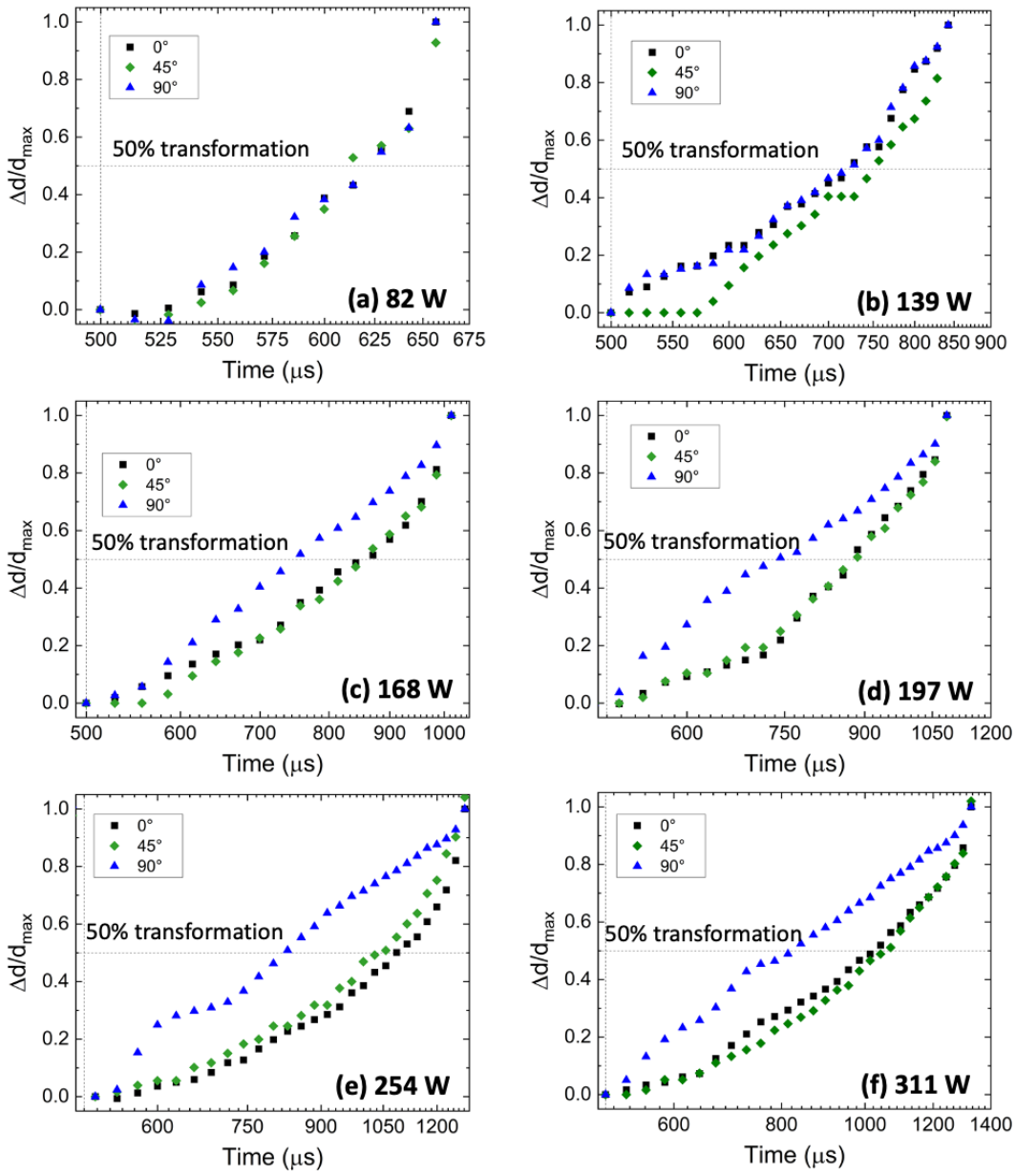

Figure 4.13. The time evolution of fractional decrease in dimension ($\Delta d/d_{max}$) for 0º, 45º and 90º for each power case. The time corresponding to the intersection of each curve and the horizontal "50% transformation" line is the $t_{0.5}$.

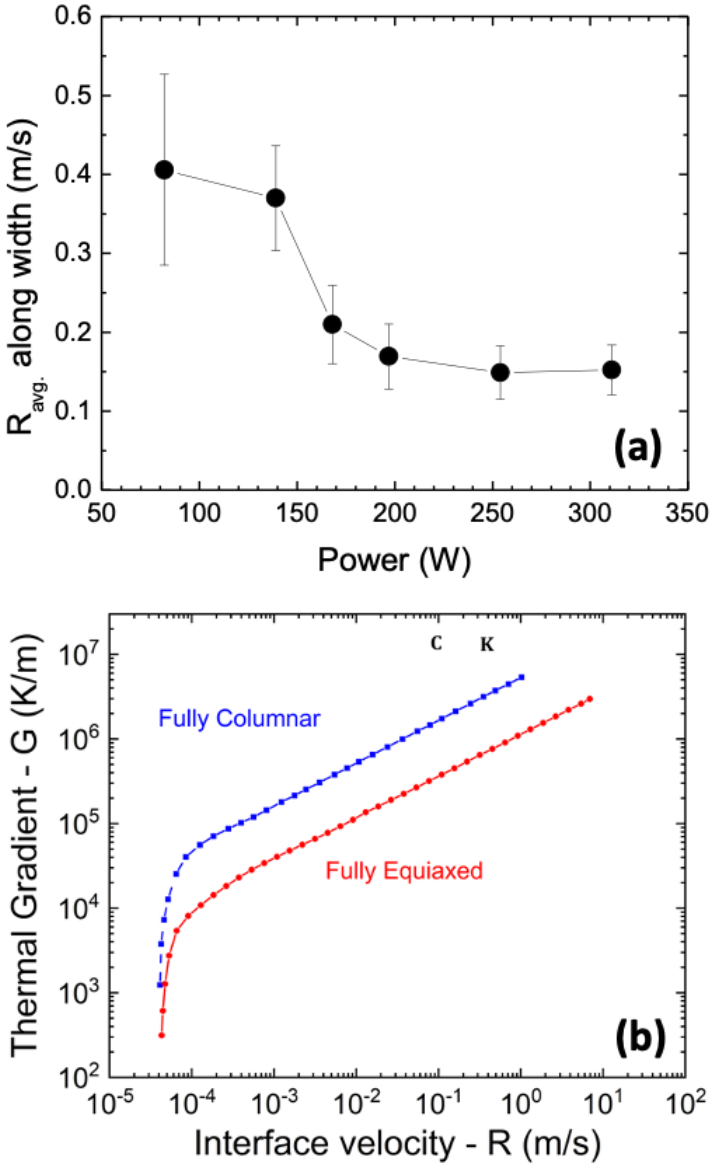

Figure 4.14. (a) Variation in steady state velocity (along the width) with changing laser power, (b) G-R map for Ti-6Al-4V (replotted from [29]). Note that C = 82 W and K = 168 W.

- Both the conduction (82W) and keyhole (168 W) melt pool showed a columnar microstructure with (110) texture along the build direction. This was attributed to either epitaxial solidification from the substrate or a combined effect of the melt pool shape and the easy growth direction being perpendicular to the S/L interface.

Chapter 5

Physics-based approach to obtain transient temperature evolution based on in-situ radiographs of spot melting event

5.1. Motivation and objectives

As reviewed in the Sec. 2.3, understanding the transient dynamics of the melt pool and vapor cavity is key in determining the suitable process parameters required to produce the desired microstructure in AM and welding processes. Building on the research detailed in Sec. 2.4.2, we leveraged x-ray radiography to understand the transient dynamics in spot melts as a function of the laser power in Chapter 4. Another important part of the puzzle in determining the solidification microstructure is the thermal gradient (G) and cooling rate. The evolution of temperature around a melt pool (therefore, cooling rate and/or thermal gradient (G)) has been estimated in recent years either only on the top surface of the melt pool using high-speed IR thermography [161] during the AM process or in the sub-surface regions using in-situ high-speed x-ray diffraction [162, 163]. All these methods either sacrifice the spatial resolution for good temporal resolution or vice versa. In this chapter, we aim to address two objectives: (i) Convert a time series of radiographs depicting spot melting into density maps using the Beer-Lambert's law as the physical basis; (ii) Further extract useful sub-surface temperature distribution and its transient evolution in and around the melt pool by converting the above density map into a temperature map.

5.2. Scientific background

The fundamental basis for most used radiography and tomography tools in materials science is image contrast based on difference in mass-absorption and depends heavily on the nature of the atomic species in the system. In the case of systems where absorption contrast is

operational, irrespective of type of incident radiation, the measured (transmitted) intensity (I) and incident intensity (I_0) are related through the Beer-Lambert's law [164], as shown in Eqn. 1

$$I = I_0 e^{-(\frac{\mu}{\rho})t} \quad \cdots\cdots\cdots (1)$$

where, μ is the absorption coefficient, ρ is the density and t is the thickness of the absorbing medium. In the current case, the data obtained from the x-ray radiographs are pixels whose grayscale values (I) are proportional to the absorption coefficient. Further, Eqn. 1 can be rearranged to describe the density (ρ) as a function of I. Since the density of different phases (solid, liquid and vapor) are different, it can be used as a discriminator to distinguish the interphase boundaries. Further, density (ρ) is a function of temperature and therefore, the density maps can be used to estimate temperature fields. This approach has been successful in computed tomography as reviewed by Fani et al. [165]

5.3. Detailed methodology with example case study

The case study used here is a conduction-mode spot melt experiment on a Ti-6Al-4V substrate (conducted in an argon ambient) with the following process parameters: laser power = 82W and dwell time = 8ms. The workflow implementing the proposed solution is shown in Fig. 5.1. Each step in the workflow is implemented using the MATLAB code written in-house (provided in the Appendix) and is described in detail with simplifying assumptions made, if any.

Step 1: The raw image sequence obtained from x-ray radiography experiments are converted from intensity contrast maps to density contrast maps using the Beer-Lambert's law (as shown by Eqn.1) as the governing equation. The first task is to calibrate the conversion from intensity to density and is performed using the first image in the sequence (at room temperature,

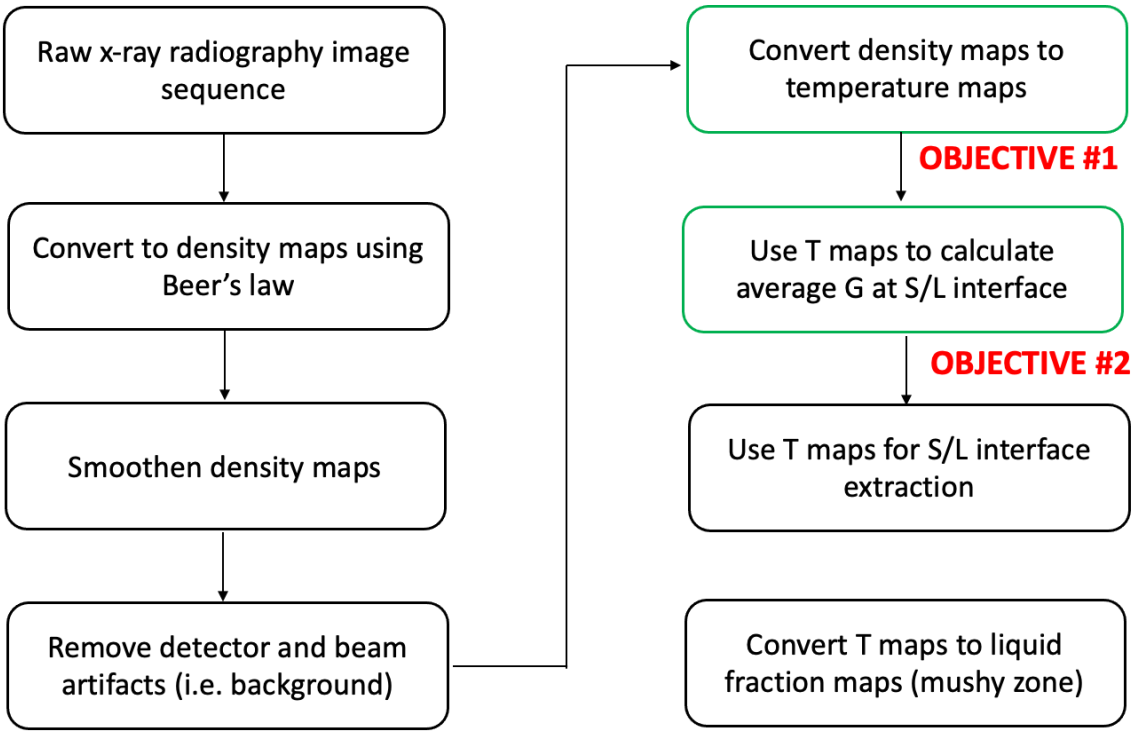

Figure 5.1. Flowchart showing the sequence of operations to convert a radiography image into a density map (and further, into a thermography image). The two key objectives of the study are highlighted.

before initiation of melting process). Due to the absorption coefficients at the given x-ray energy, we can infer that the Ti-64 region absorbs more x-rays than the Ar region. For the calibration process, the I_o (= I_{Ar}) and I_{Ti64} are taken to be equal to the maximum and minimum intensities, respectively, in the first image of the sequence. Further, using known room-temperature density values of the Ti-64 (4430 kg/m^3) and the Ar (1.652 kg/m^3) at room temperature with the corresponding intensity values, the (μt) factor in Eqn.1 is determined. The (μt) factor can be used to calculate the density corresponding to each intensity point in the image sequence. An example of a raw intensity map and corresponding raw density map is shown in Fig. 5.2a and b respectively.

Step 2: A raw density heatmap obtained from Step 1 and the corresponding 3D plot is shown Fig 5.2b and c, respectively. The 3D plot (Fig. 5.2c) shows that the map is very speckled and smoothing operation is necessary to even out the outlier pixels. A smoothing operation is carried out using an "n-point moving average" method in MATLAB, wherein each point is designated as the average of n x n nearest neighbor pixels surrounding it. Note that this operation has been only performed on the Ti64 region (and not on the Ar region; to avoid severe averaging of the substrate top region and loss of valuable melt pool data) and all following steps will use only the data from the Ti64 region. A possible disadvantage of this smoothing technique is that very-high intensity pixels might end up bleeding into neighboring pixels during the averaging process creating an outlier "smudge" of pixels and a possible solution for this might be to use a median filter. As the next step, an optimization of the n-point averaging method was conducted (with n = 3,5 and 10). Fig. 5.3 shows that n = 5 is an acceptable optimal case which doesn't excessively smooth out the features (as in the case of n = 10) or doesn't smooth the raw density surface much (as in the case of n = 3) as seen in the corresponding 3D plots.

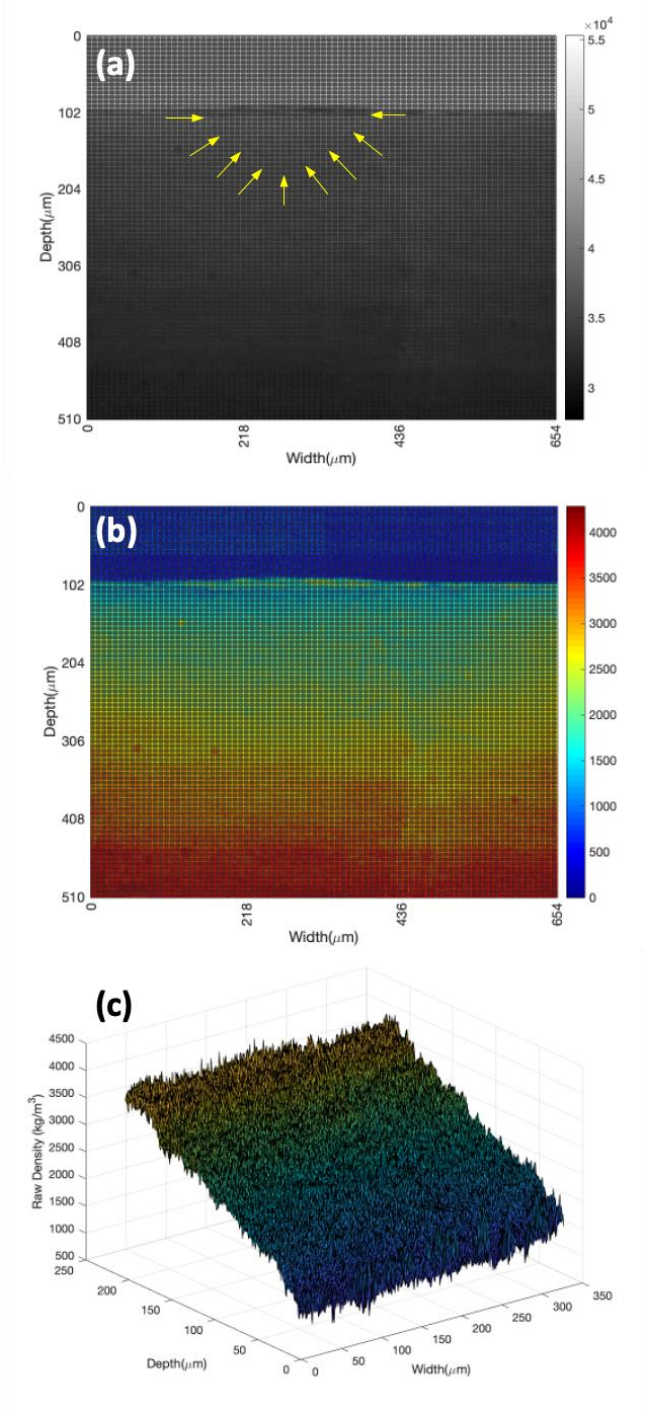

Figure 5.2. (a) Raw radiography image shown with the solid-liquid interface outlined with yellow arrows; (b) Raw density map obtained from radiography map shown in (a), colorscale depicts the density in kg/m^3; (c) 3D surface plot of the raw density map shown in (b) depicting the speckling (and therefore, need for the smoothing operation).

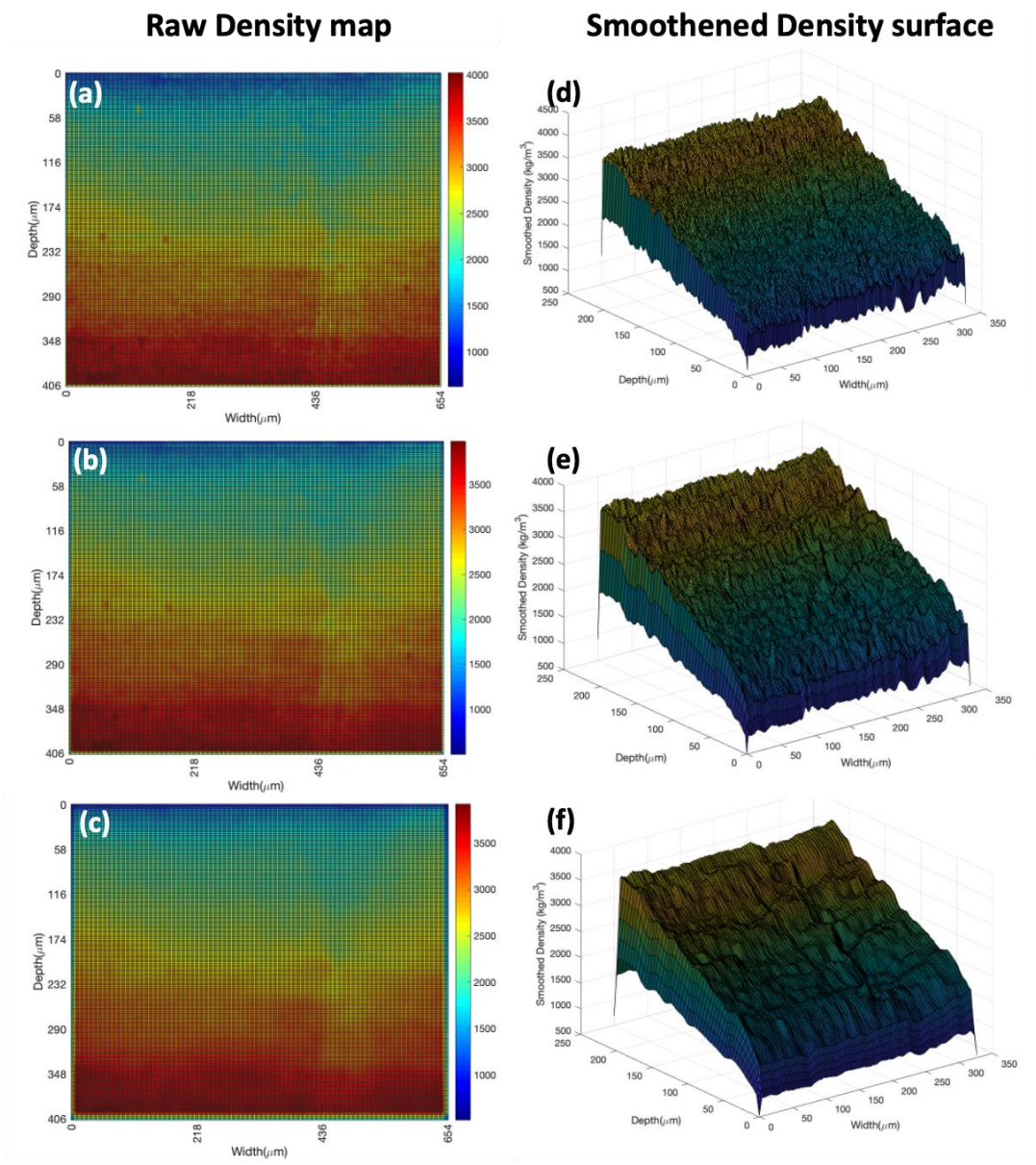

Figure 5.3. Smoothened density maps obtained from the raw density map shown in Fig. 5.2 using the n-point averaging method for different n - (a) n = 3, (b) n = 5, (c) n =10; Corresponding 3D surface plots of smoothened density for different n - (d) n = 3, (e) n = 5, (f) n =10.

Step 3: The smoothened density plots may still contain background artefacts which arise from the characteristics of the incident beam, experimental setup, variation of sample thickness (along the height) or detector assembly, to name a few. To remove this background, a "correction" map is obtained by dividing the first smoothened density map by the room temperature density (ρ(Ti64) = 4430 kg/m^3). Further, each smoothed density map in the time series is divided by the "correction" map. Snapshots of a spot melting event at different time intervals before and after the background correction process are shown in Fig. 5.4. The corrected density maps show a clear S/L interface, thus satisfying objective #1 of this study. The histograms of the above corrected density maps, shown in Fig. 5.4e, provide a good sanity check as they indicate the average density decreases with increasing dwell time (since average temperature increases with increasing dwell time and the density is inversely proportional to the temperature).

Step 4: The literature values for the variation of density of solid and liquid Ti64 are fit to different polynomial functions for different temperature ranges using the "polyfit" function in MATLAB – the literature values and fit polynomials are shown in Fig. 5.5. Note that the temperature ranges, corresponding literature sources, order of polynomial fits are provided in Table 5.1. The corrected density maps are further converted to temperature maps using the above polynomial equations. The assumption made here during the calculation of the density of the solid + liquid mixture in the mushy zone is that the liquid fraction varies linearly with the temperature (shown in the inset of Fig. 5.5). Corrected density maps and corresponding temperature maps of a spot melting event at different time intervals are shown in Fig. 5.6.

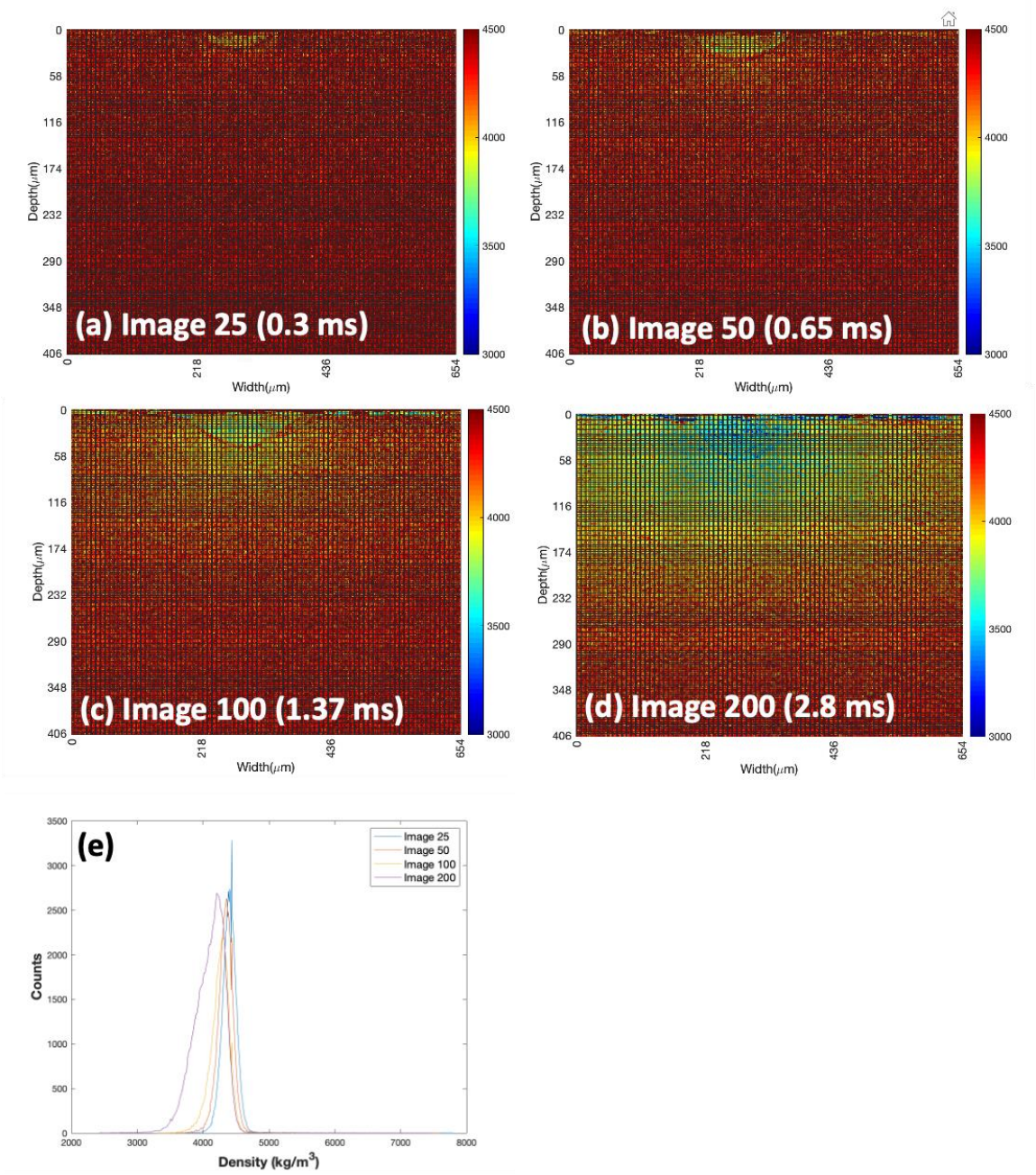

Figure 5.4. Snapshots of corrected density maps (after background removal from the smoothened density maps) from the time series of spot melting at time instants of (a) t = 0.3 ms, (b) t = 0.65 ms, (c) t = 1.37 ms, (d) t = 2.8 ms. The solid-liquid interface is clearly visible at all time instants. (e) Histogram of the density values from corrected density maps in (a,b,c,d) showing the average density decreases with increasing dwell time.

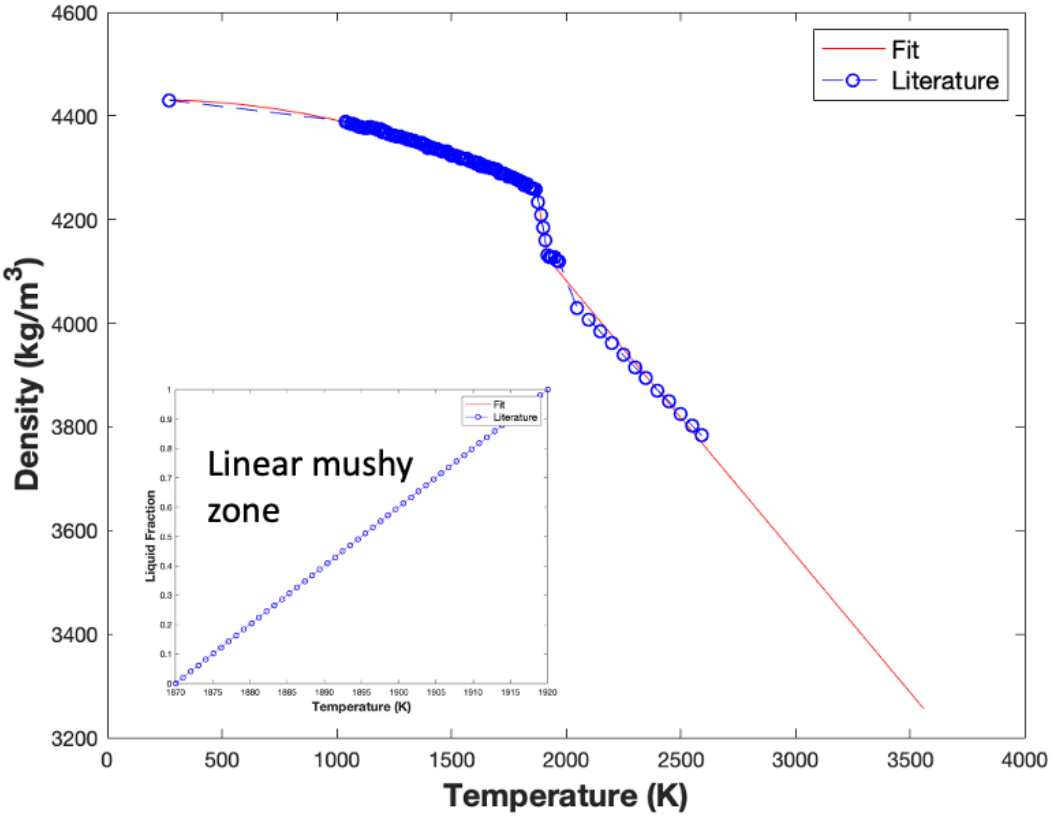

Figure 5.5. The variation of density of Ti-6Al-4V with temperature adapted from published literature (blue circles) for solid, mushy zone and liquid phases and corresponding polynomial fits (red line) for each region; (Inset) Linear variation of liquid fraction vs temperature assumed while calculating the density in the mushy zone.

Table 5.1. Order of polynomial used to fit reported density values from experimental literature (with literature sources) for different phases of Ti-6Al-4V and corresponding temperature ranges. *Density data for the temperature range corresponding to the only mushy zone used from source [166]

Phase	T range (K)	Order of polyfit	References
Solid	270 - 1870	2	[167]
Mushy zone	1870 - 1920	1	[166, 167]*
Liquid	1920 - 3560	1	[167, 168]
Vapor	> 3560	-	[168]

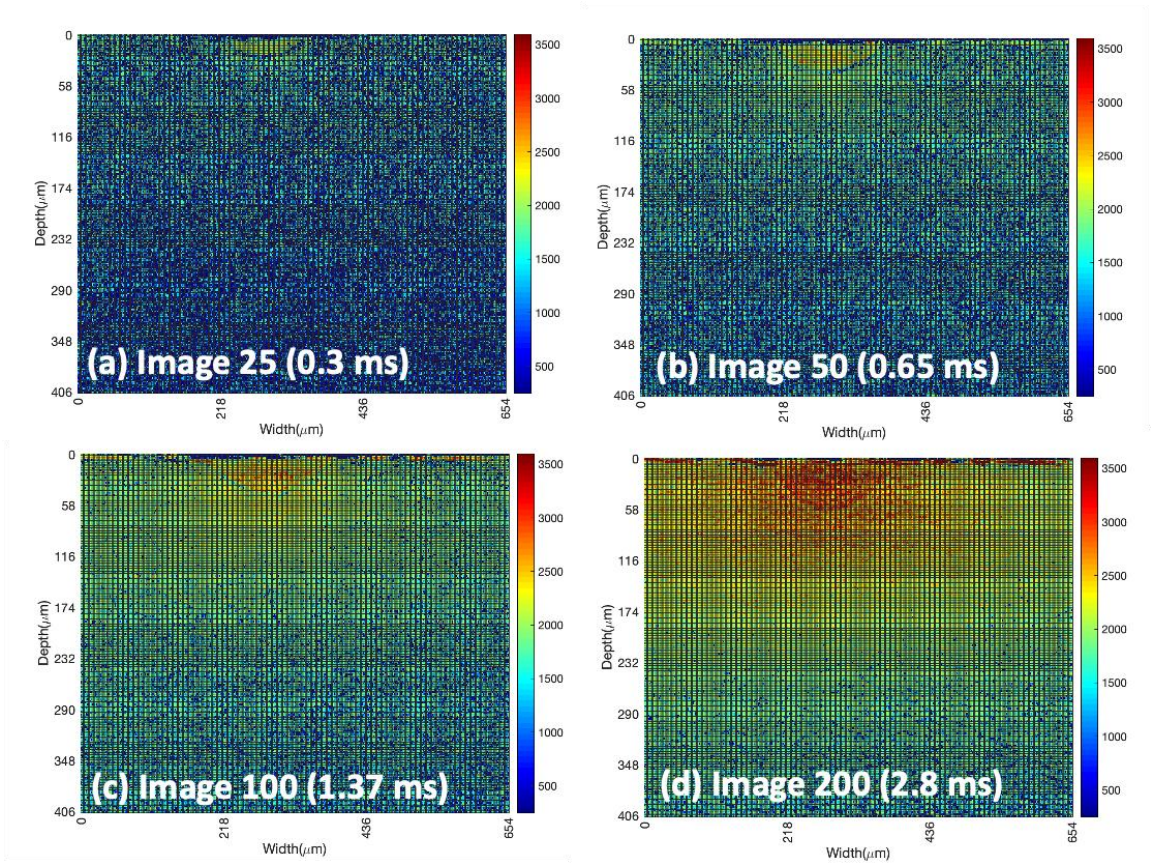

Figure 5.6. Snapshots of temperature maps (obtained from corrected density maps) from the time series of spot melting at time instants of (a) t = 0.3 ms, (b) t = 0.65 ms, (c) t = 1.37 ms, (d) t = 2.8 ms. The solid-liquid interface is clearly visible at all time instants. However, the solid-liquid interface seems to be at progressively higher temperatures with increasing dwell time.

5.4. Discussion

Sensitivity of the method / sources of uncertainty: While the temporal resolution remains unaffected by the operations performed in the workflow, the spatial resolution of the temperature maps is hugely dependent on smoothing method used. Additionally, the uncertainty in temperature values is dependent mostly on the uncertainty in the density values resulting from the smoothing operation and on the uncertainty in experimental density vs. temperature data (and the polynomial fits) used for the conversion of density maps to temperature maps.

Current challenges and possible solutions: It can be seen from the temperature maps in Fig. 5.6. that the solid-liquid interface appears to be at a higher temperature with increasing dwell time (while it is known to be equal to the solidus temperature). This occurs because x-ray radiography does not resolve the absorption data in the direction of the beam. The melt pool size and the heat content increase progressively with increasing dwell time and since we observe a sum of the absorption of the beam through-thickness on a given radiograph pixel, the S/L interface appears to be at higher temperatures with increasing dwell time. A possible method of solving this (in the case of spot melts) to obtain "true" temperature maps is by assuming a symmetric melt pool shape along all its 3-D cross-sections and follow the method used by [169].

Significance: In addition to understanding the transient evolution of thermal gradient, the "true" temperature maps can be used to automate the extraction of melt pool and vapor cavity dimensions (by tracking the solidus and vaporization temperature isotherms). Additionally, the "true" temperature maps can be converted into spatial variation of liquid fraction, thus helping us understand more about mushy zone during both melting and solidification.

Chapter 6
Conclusions

The aim of this thesis research was to better understand the novel spot melt strategy for application in additive manufacturing using both ex-situ and in-situ characterization tools. The questions which formed the basis of the study are answered here:

Theme 1: *Exploration of differences in microstructure between the novel spot-melt and conventional raster-melt built Ti-6Al-4V*

(i) *Does the crystallographic texture and phase fraction vary as a function of scan strategy and build height?*

- Texture: Spot-melt strategy showed β<100> fiber texture, whereas the linear-melt strategy showed a cube texture about the build axis. The easy growth direction of BCC <001> aligned closely with the build direction consistent with the net maximum thermal gradient (G) being almost parallel to the build direction. The texture intensity in the spot-melt case was relatively uniform across the build height, while the linear-melt case showed a gradual decrease in the overall intensity from the top of the build to the substrate. In terms of both the phase fraction and texture, the novel spot melt produced a more homogeneous microstructure across the build height compared to the linear-melt case.
- Phase fraction: The β phase fractions in both E-PBF builds were significantly higher than the feedstock powder (3 wt.%). The β phase fraction for the spot-melt sample was about 11 wt.% at the top of the build and gradually decreased to about 8 wt.% near the substrate. This was attributed to the repeated thermal cycling of the build layers during the processing. The linear-melt sample showed an overall higher β phase fraction and also a stronger trend of

decreasing β fraction towards the substrate compared to the spot melt case likely due to a gradual increase in the heat accumulation towards the top of the build in the linear-melt case.

(ii) *Does the Burgers Orientation Relationship (BOR) between the β and α phases sustain through the thermal excursions around the β-transus experienced during the build process?*

The Burgers orientation relationship (BOR) between the parent β phase and the daughter α phase was clearly observed in both spot- and linear-melt samples across the entire build height despite the significant thermal excursions experienced during the build process. This was attributed to the "texture memory" effect observed in Ti-6Al-4V processed using other methods with the reasonable assumption that the thermal excursions were mostly in the (α + β) phase field and did not dwell for long in the β phase field to induce grain growth.

(iii) *Is there a preferred set(s) of α-variants observed in the build microstructure?*

The daughter α texture intensities mostly inherited the trends set by the parent β texture. The α variant selection was more predominant in the spot-melt than in the linear-melt samples. In the case of spot-melt samples, the planar variant pair of V(2,8), corresponding to $(\bar{1}01)_\beta$ with $[\bar{2}\bar{2}\bar{2}]_\beta$ and $[2\bar{2}2]_\beta$, was most consistently preferred across the build height.

Theme 2: *In-depth parametric study of the transient evolution of laser spot melt in Ti-6Al-4V alloy*

(i) *How does a single laser spot evolve spatially and temporally in terms of dimensions and velocity of the melt pool and vapor cavity?*

- In the melting stage, the melt pool begins with an initial transient and is followed by a quasi-steady state increase in dimensions. The vapor cavity dimensions shows a general increasing trend with the progression of time with fluctuations in the late stages of the melting event (due to the highly dynamic nature of the keyhole)
- The conduction mode melt pools are seen to maintain a steady width-elongated shape with an aspect ratio of 0.4-0.5 throughout the melting duration, after an initial transient increase. In the keyhole cases, however, the initial transient in D/W is seen to be steeper before moving onto a quasi-steady state aspect ratio.
- Dimensionless numbers were used to determine the driving forces for fluid flow and dominant heat transfer mechanism. The fluid flow in the conduction melt pool is mainly driven by Marangoni (surface tension gradient) force. The dominant heat transfer mechanism in the melt pool was convection.
- The melt pools showed three stages during solidification – initial increase, steady-state and final-increase. Also, the solidification kinetics for keyhole melt pools was seen to be faster in the 90º direction than the 0º and 45º directions.

(ii) *How do key characteristics of spot melting dynamics and solidification kinetics as change as a function of laser power?*

- The melt pool and vapor cavity initiation time decreased with increasing laser power. The melt pool initiation time was rationalized based on the time taken to break the surface oxide layer and the vapor cavity initiation were explained using the conduction-to-keyhole criterion.
- The linear melting rate was seen to increase with increasing laser power. Additionally, the percentage of vapor cavity in each direction was also seen to increase with increasing

power. The percent vapor in the depth direction was much greater than the width direction. This was attributed to the primary laser absorption being in the depth direction.

- The steady state solidification velocity was seen to decrease and reach a near constant value with increase in laser power.

(iii) *Do the solidification microstructures in conduction and keyhole mode melt pools correlate well with the measured transient melt pool evolution data?*

- Both the conduction (82W) and keyhole (168 W) melt pool showed a columnar microstructure with (110) texture along the build direction. This was attributed to either epitaxial solidification from the substrate or a combined effect of the melt pool shape and the easy growth direction being perpendicular to the S/L interface.

Theme 3: *Physics-based approach to obtain transient temperature evolution based on in-situ radiographs of spot melting event*

(i) Can we convert a time series of radiographs depicting spot melting into density maps using the Beer-Lambert's law as the physical basis?
(ii) Can we further extract useful sub-surface temperature distribution and its transient evolution in and around the melt pool by converting the above density map into a temperature map?

- Yes. The feasibility of both the above was demonstrated. However, in its current state the workflow yielded averaged through-thickness density and temperature values since radiography is a through-thickness technique.

These observations of the transient melt pool evolution are of both fundamental and technological advantage. First, from an engineering standpoint, these observations can be employed to better inform spot-melt strategies to produce additively manufactured parts with suitable microstructures. Second, from a fundamental standpoint, these observations can used to validate and improve high-fidelity, high-performance, multi-physics melt pool simulation platforms (such as the Exascale simulation for Additive Manufacturing – ExaAM).

Chapter 7
Future work

1) Effect of other process parameters and alloy systems

The effect of other spot melt characteristics (such as spot dwell time) on melt pool dynamics and solidification kinetics can be probed. Additionally, in the present study, the range of thermal gradients (G) accessed was narrow. An experimental matrix with process parameters such as laser beam diameter, beam shape and substrate pre-heat temperature which have been seen to have a significant effect on the G can be probed to study the kinetics involved in the formation of a wider range of solidification microstructures. The studies with substrate
All the above parametric studies can be naturally translated to different alloy systems. In this case, a comparison between spot melts in alloys and their pure metal counterparts can be used to try and separate the effect of the mushy zone. All these studies can be further extended to include a critical part of powder-bed processes, the metal powder on substrate.

2) Double spot melt pools

The present study dealt with the characterization of a single spot melt pool, which is a unit process of a spot-melt built AM product. The actual spot-melt build in AM involves interaction between the melt pool dynamics of more than one melt pool which will further affect the microstructure formation. The logical next step is to study double spot melt pools. In this regard, two key parameters that might affect the interaction between sequential spot melts are the spatial overlap (Δx) and temporal delay (Δt) between them. Therefore, double spot melts with an experimental matrix involving a combination of Δx and Δt with constant power and dwell time in Ti-6Al-4V will be studied as a next step.

3) Raster melting

There have been many in-situ x-ray radiography studies looking at the vapor cavity dynamics and porosity mitigation [103, 126] in raster melting. However, solidification kinetics in this case haven't been studied in detail. Solidification kinetics can be probed as a function of an experimental matrix with laser power and scan speed as variables.

List of References

[1] W.J. Sames, F.A. List, S. Pannala, R.R. Dehoff, S.S. Babu, The metallurgy and processing science of metal additive manufacturing, International Materials Reviews 61(5) (2016) 315-360.

[2] L.E. Murr, Metallurgy of additive manufacturing: Examples from electron beam melting, Addit. Manuf. 5 (2015) 40-53.

[3] L.E. Murr, S.M. Gaytan, D.A. Ramirez, E. Martinez, J. Hernandez, K.N. Amato, P.W. Shindo, F.R. Medina, R.B. Wicker, Metal Fabrication by Additive Manufacturing Using Laser and Electron Beam Melting Technologies, J. Mater. Sci. Technol. 28(1) (2012) 1-14.

[4] L.E. Murr, E. Martinez, S.M. Gaytan, D.A. Ramirez, B.I. Machado, P.W. Shindo, J.L. Martinez, F. Medina, J. Wooten, D. Ciscel, U. Ackelid, R.B. Wicker, Microstructural Architecture, Microstructures, and Mechanical Properties for a Nickel-Base Superalloy Fabricated by Electron Beam Melting, Metallurgical and Materials Transactions A 42(11) (2011) 3491-3508.

[5] N. Raghavan, Understanding Process-Structure Relationship For Site-Specifific Microstructure Control in Electron Beam Powder Bed Additive Manufacturing Process Using Numerical Modeling, University of Tennessee, 2017.

[6] T. DebRoy, H.L. Wei, J.S. Zuback, T. Mukherjee, J.W. Elmer, J.O. Milewski, A.M. Beese, A. Wilson-Heid, A. De, W. Zhang, Additive manufacturing of metallic components – Process, structure and properties, Prog. Mater. Sci. 92 (2018) 112-224.

[7] T. DebRoy, S.A. David, Physical processes in fusion welding, Reviews of Modern Physics 67(1) (1995) 85-112.

[8] M. Gaumann, C. Bezençon, P. Canalis, W. Kurz, Single-crystal laser deposition of superalloys: Processing-microstructure maps, Acta Mater. 49 (2001) 1051-1062.

[9] M. Gaumann, S. Henry, F. Cleton, J.-D. Wagniere, W. Kurz, Epitaxial laser metal forming: analysis of microstructure formation, Materials Science and Engineering A 271 (1999).

[10] W. Kurz, C. Bezençon, M. Gäumann, Columnar to equiaxed transition in solidification processing, Science and Technology of Advanced Materials 2(1) (2001) 185-191.

[11] H. Helmer, A. Bauereiß, R.F. Singer, C. Körner, Grain structure evolution in Inconel 718 during selective electron beam melting, Mat. Sci. Eng. A 668 (2016) 180-187.

[12] R.R. Dehoff, M.M. Kirka, W.J. Sames, H. Bilheux, A.S. Tremsin, L.E. Lowe, S.S. Babu, Site specific control of crystallographic grain orientation through electron beam additive manufacturing, Mater. Sci. Technol. 31(8) (2014) 931-938.

[13] M.M. Kirka, P. Nandwana, Y. Lee, R.R. Dehoff, Solidification and solid-state transformation sciences in metals additive manufacturing, Scr. Mater. 135 (2017) 130-134.

[14] Y.S. Lee, M.M. Kirka, R.B. Dinwiddie, N. Raghavan, J. Turner, R.R. Dehoff, S.S. Babu, Role of scan strategies on thermal gradient and solidification rate in electron beam powder bed fusion, Addit. Manuf. 22 (2018) 516-527.

[15] N. Raghavan, R. Dehoff, S. Pannala, S. Simunovic, M. Kirka, J. Turner, N. Carlson, S.S. Babu, Numerical modeling of heat-transfer and the influence of process parameters on tailoring the grain morphology of IN718 in electron beam additive manufacturing, Acta Mater. 112 (2016) 303-314.

[16] P. Nandwana, Y. Lee, Influence of scan strategy on porosity and microstructure of Ti-6Al-4V fabricated by electron beam powder bed fusion, Mater. Today Commun. 24 (2020) 100962.

[17] G.L. Knapp, N. Raghavan, A. Plotkowski, T. DebRoy, Experiments and simulations on solidification microstructure for Inconel 718 in powder bed fusion electron beam additive manufacturing, Addit. Manuf. 25 (2019) 511-521.

[18] S.S. Al-Bermani, M.L. Blackmore, W. Zhang, I. Todd, The Origin of Microstructural Diversity, Texture, and Mechanical Properties in Electron Beam Melted Ti-6Al-4V, Metall. Mater. Trans. A 41A(13) (2010) 3422-3434.

[19] H.L. Wei, J. Mazumder, T. DebRoy, Evolution of solidification texture during additive manufacturing, Sci. Rep. 5 (2015) 16446.

[20] X. He, J.W. Elmer, T. DebRoy, Heat transfer and fluid flow in laser microwelding, Journal of Applied Physics 97(8) (2005).

[21] X. He, P.W. Fuerschbach, T. DebRoy, Heat transfer and fluid flow during laser spot welding of 304 stainless steel, J. Phys. D: Appl. Phys 36 (2003) 1388–1398.

[22] S.A. Khairallah, A.T. Anderson, A. Rubenchik, W.E. King, Laser powder-bed fusion additive manufacturing: Physics of complex melt flow and formation mechanisms of pores, spatter, and denudation zones, Acta Mater. 108 (2016) 36-45.

[23] N. Kouraytem, X. Li, R. Cunningham, C. Zhao, N. Parab, T. Sun, A.D. Rollett, A.D. Spear, W. Tan, Effect of Laser-Matter Interaction on Molten Pool Flow and Keyhole Dynamics, Physical Review Applied 11(6) (2019).

[24] W. Zhang, G.G. Roy, J.W. Elmer, T. DebRoy, Modeling of heat transfer and fluid flow during gas tungsten arc spot welding of low carbon steel, Journal of Applied Physics 93(5) (2003) 3022-3033.

[25] T. Zacharia, S.A. David, J.M. Vitek, T. DebRoy, Weld Pool Development during GTA and Laser Beam Welding of Type 304 Stainless Steel, Part II—Experimental Correlation, Welding Journal 68 (1989).

[26] A. Intl., Standard Terminology for Additive Manufacturing – General Principles – Terminology (ISO/ASTM 52900:2015(E)), 2016, pp. 1-9.

[27] W.E. Frazier, Metal Additive Manufacturing: A Review, J. Mater. Eng. Perform. 23(6) (2014) 1917-1928.

[28] L. Thijs, F. Verhaeghe, T. Craeghs, J.V. Humbeeck, J.-P. Kruth, A study of the microstructural evolution during selective laser melting of Ti–6Al–4V, Acta Mater. 58(9) (2010) 3303-3312.

[29] P.A. Kobryn, S.L. Semiatin, Microstructure and texture evolution during solidification processing of Ti–6Al–4V, J. Mater. Process. Technol. 135(2-3) (2003) 330-339.

[30] E. Brandl, V. Michailov, B. Viehweger, C. Leyens, Deposition of Ti–6Al–4V using laser and wire, part I: Microstructural properties of single beads, Surf. Coat. Technol. 206(6) (2011) 1120-1129.

[31] A.A. Antonysamy, J. Meyer, P.B. Prangnell, Effect of build geometry on the β-grain structure and texture in additive manufacture of Ti-6Al-4V by selective electron beam melting, Mater. Charact. 84 (2013) 153-168.

[32] H. Galarraga, D.A. Lados, R.R. Dehoff, M.M. Kirka, P. Nandwana, Effects of the microstructure and porosity on properties of Ti-6Al-4V ELI alloy fabricated by electron beam melting (EBM), Addit. Manuf. 10 (2016) 47-57.

[33] H. Galarraga, R.J. Warren, D.A. Lados, R.R. Dehoff, M.M. Kirka, P. Nandwana, Effects of heat treatments on microstructure and properties of Ti-6Al-4V ELI alloy fabricated by electron beam melting (EBM), Mat. Sci. Eng. A 685 (2017) 417-428.

[34] P. Nandwana, Y. Lee, C. Ranger, A.D. Rollett, R.R. Dehoff, S.S. Babu, Post-processing to Modify the α Phase Micro-Texture and β Phase Grain Morphology in Ti-6Al-4V Fabricated by Powder Bed Electron Beam Melting, Metall. Mater. Trans. A 50A(8) (2019) 3973-3974.

[35] G. Kasperovich, J. Haubrich, J. Gussone, G. Requena, Correlation between porosity and processing parameters in TiAl6V4 produced by selective laser melting, Mater. Des. 105 (2016) 160-170.

[36] J.V. Gordon, S.P. Narra, R.W. Cunningham, H. Liu, H. Chen, R.M. Suter, J.L. Beuth, A.D. Rollett, Defect structure process maps for laser powder bed fusion additive manufacturing, Addit. Manuf. 36 (2020).

[37] R. Cunningham, S.P. Narra, C. Montgomery, J. Beuth, A.D. Rollett, Synchrotron-Based X-ray Microtomography Characterization of the Effect of Processing Variables on Porosity Formation in Laser Power-Bed Additive Manufacturing of Ti-6Al-4V, JOM 69(3) (2017) 479-484.

[38] M. Tang, P.C. Pistorius, J.L. Beuth, Prediction of lack-of-fusion porosity for powder bed fusion, Addit. Manuf. 14 (2017) 39-48.

[39] J. Gockel, J. Beuth, K. Taminger, Integrated control of solidification microstructure and melt pool dimensions in electron beam wire feed additive manufacturing of Ti-6Al-4V, Addit. Manuf. 1-4 (2014) 119-126.

[40] N. Hrabe, T. Quinn, Effects of processing on microstructure and mechanical properties of a titanium alloy (Ti-6Al-4V) fabricated using electron beam melting (EBM), Part 2: Energy input, orientation, and location, Materials Science and Engineering a-Structural Materials Properties Microstructure and Processing 573 (2013) 271-277.

[41] K. Dietrich, J. Diller, S. Dubiez-Le Goff, D. Bauer, P. Forêt, G. Witt, The influence of oxygen on the chemical composition and mechanical properties of Ti-6Al-4V during laser powder bed fusion (L-PBF), Addit. Manuf. 32 (2020).

[42] H.P. Tang, M. Qian, N. Liu, X.Z. Zhang, G.Y. Yang, J. Wang, Effect of Powder Reuse Times on Additive Manufacturing of Ti-6Al-4V by Selective Electron Beam Melting, Jom 67(3) (2015) 555-563.

[43] P. Nandwana, W.H. Peter, R.R. Dehoff, L.E. Lowe, M.M. Kirka, F. Medina, S.S. Babu, Recyclability Study on Inconel 718 and Ti-6Al-4V Powders for Use in Electron Beam Melting, Metall. Mater. Trans. B-Proc. Metall. Mater. Proc. Sci. 47(1) (2016) 754-762.

[44] A.H. Chern, P. Nandwana, T. Yuan, M.M. Kirka, R.R. Dehoff, P.K. Liaw, C.E. Duty, A review on the fatigue behavior of Ti-6Al-4V fabricated by electron beam melting additive manufacturing, International Journal of Fatigue 119 (2019) 173-184.

[45] H. Galarraga, R.J. Warren, D.A. Lados, R.R. Dehoff, M.M. Kirka, Fatigue crack growth mechanisms at the microstructure scale in as-fabricated and heat treated Ti-6Al-4V ELI manufactured by electron beam melting (EBM), Engineering Fracture Mechanics 176 (2017) 263-280.

[46] N. Hrabe, T. Gnäupel-Herold, T. Quinn, Fatigue properties of a titanium alloy (Ti–6Al–4V) fabricated via electron beam melting (EBM): Effects of internal defects and residual stress, International Journal of Fatigue 94 (2017) 202-210.

[47] L.N. Carter, C. Martin, P.J. Withers, M.M. Attallah, The influence of the laser scan strategy on grain structure and cracking behaviour in SLM powder-bed fabricated nickel superalloy, J. Alloys Compd. 615 (2014) 338-347.

[48] Arcam, EBM Hardware. http://www.arcam.com/technology/electron-beammelting/hardware/, (accessed April 19.2019).

[49] S. Tammas-Williams, H. Zhao, F. Leonard, F. Derguti, I. Todd, P.B. Prangnell, XCT analysis of the influence of melt strategies on defect population in Ti-6Al-4V components manufactured by Selective Electron Beam Melting, Mater. Charact. 102 (2015) 47-61.

[50] Y.M. Arısoy, L.E. Criales, T. Özel, B. Lane, S. Moylan, A. Donmez, Influence of scan strategy and process parameters on microstructure and its optimization in additively manufactured nickel alloy 625 via laser powder bed fusion, The International Journal of Advanced Manufacturing Technology 90(5-8) (2016) 1393-1417.

[51] A. Plotkowski, M.M. Kirka, S.S. Babu, Verification and validation of a rapid heat transfer calculation methodology for transient melt pool solidification conditions in powder bed metal additive manufacturing, Addit. Manuf. 18 (2017) 256-268.

[52] R.R. Kamath, P. Nandwana, Y. Ren, H. Choo, Solidification texture, variant selection, and phase fraction in a spot-melt electron-beam powder bed fusion processed Ti-6Al-4V, Addit. Manuf. 46 (2021).

[53] G. Lütjering, J.C. Williams, Titanium, Springer2007.

[54] M.J. Donachie, Titanium: A Technical Guide, ASM International (2000).

[55] J.W. Elmer, T.A. Palmer, S.S. Babu, E.D. Specht, In situ observations of lattice expansion and transformation rates of α and β phases in Ti–6Al–4V, Mat. Sci. Eng. A 391(1-2) (2005) 104-113.

[56] W.G. Burgers, On the process of transition of the cubic-body-centered modification into the hexagonal-close-packed modification of zirconium, Physica 1 (1934) 561-586.

[57] H. Beladi, Q. Chao, G.S. Rohrer, Variant selection and intervariant crystallographic planes distribution in martensite in a Ti–6Al–4V alloy, Acta Mater. 80 (2014) 478-489.

[58] T. Ahmed, H.J. Rack, Phase transformations during cooling in α + β titanium alloys, Mat. Sci. Eng. A 243 (1998) 206-211.

[59] S.M. Kelly, Thermal and Microstructure Modeling of Metal Deposition Processes with Application to Ti-6Al-4V, Mat. Sci. Eng., Virginia Polytechnic Institute and State University, 2004.

[60] X. Tan, Y. Kok, W.Q. Toh, Y.J. Tan, M. Descoins, D. Mangelinck, S.B. Tor, K.F. Leong, C.K. Chua, Revealing martensitic transformation and α/β interface evolution in electron beam melting three-dimensional-printed Ti-6Al-4V, Sci. Rep. 6 (2016) 26039.

[61] S.C. Vogel, S. Takajo, M.A. Kumar, E.N. Caspi, A. Pesach, E. Tiferet, O. Yeheskel, Ambient and High-Temperature Bulk Characterization of Additively Manufactured Ti-6Al-4V Using Neutron Diffraction, JOM 70(9) (2018) 1714-1722.

[62] A. Safdar, L.Y. Wei, A. Snis, Z. Lai, Evaluation of microstructural development in electron beam melted Ti-6Al-4V, Mater. Charact. 65 (2012) 8-15.

[63] S. Cao, R. Chu, X. Zhou, K. Yang, Q. Jia, C.V.S. Lim, A. Huang, X. Wu, Role of martensite decomposition in tensile properties of selective laser melted Ti-6Al-4V, J. Alloys Compd. 744 (2018) 357-363.

[64] J. Haubrich, J. Gussone, P. Barriobero-Vila, P. Kürnsteiner, E.A. Jägle, D. Raabe, N. Schell, G. Requena, The role of lattice defects, element partitioning and intrinsic heat effects on the microstructure in selective laser melted Ti-6Al-4V, Acta Mater. 167 (2019) 136-148.

[65] X. Tan, Y. Kok, Y.J. Tan, M. Descoins, D. Mangelinck, S.B. Tor, K.F. Leong, C.K. Chua, Graded microstructure and mechanical properties of additive manufactured Ti–6Al–4V via electron beam melting, Acta Mater. 97 (2015) 1-16.

[66] N. Sridharan, Y. Chen, P. Nandwana, R.M. Ulfig, D.J. Larson, S.S. Babu, On the potential mechanisms of β to α′ + β decomposition in two phase titanium alloys during additive manufacturing: a combined transmission Kikuchi diffraction and 3D atom probe study, J Mater. Sci. 55(4) (2020) 1715-1726.

[67] Y.N. Wang, J.C. Huang, Texture analysis in hexagonal materials, Mater. Chem. Phys. 81(1) (2003) 11-26.

[68] S.L. Semiatin, V. Seetharaman, I. Weiss, The Thermomechanical Processing of Alpha/Beta Titanium Alloys, JOM 49 (1997) 33-39.

[69] M. Simonelli, Y.Y. Tse, C. Tuck, On the Texture Formation of Selective Laser Melted Ti-6Al-4V, Metall. Mater. Trans. A 45A(6) (2014) 2863-2872.

[70] C. de Formanoir, S. Michotte, O. Rigo, L. Germain, S. Godet, Electron beam melted Ti-6Al-4V: Microstructure, texture and mechanical behavior of the as-built and heat-treated material, Mat. Sci. Eng. A 652 (2016) 105-119.

[71] M. Shao, S. Vijayan, P. Nandwana, J.R. Jinschek, The effect of beam scan strategies on microstructural variations in Ti-6Al-4V fabricated by electron beam powder bed fusion, Mater. Des. 196 (2020) 109165.

[72] P.L. Stephenson, N. Haghdadi, R. DeMott, X.Z. Liao, S.P. Ringer, S. Primig, Effect of scanning strategy on variant selection in additively manufactured Ti-6Al-4V, Addit. Manuf. 36 (2020) 101581.

[73] D.R. Waryoba, J.S. Keist, C. Ranger, T.A. Palmer, Microtexture in additively manufactured Ti-6Al-4V fabricated using directed energy deposition, Mat. Sci. Eng. A 734 (2018) 149-163.

[74] D. Bhattacharyya, G.B. Viswanathan, S.C. Vogel, D.J. Williams, V. Venkatesh, H.L. Fraser, A study of the mechanism of α to β phase transformation by tracking texture evolution with temperature in Ti–6Al–4V using neutron diffraction, Scr. Mater. 54(2) (2006) 231-236.

[75] I. Lonardelli, N. Gey, H.R. Wenk, M. Humbert, S.C. Vogel, L. Lutterotti, In situ observation of texture evolution during α→β and β→α phase transformations in titanium alloys investigated by neutron diffraction, Acta Mater. 55(17) (2007) 5718-5727.

[76] G.C. Obasi, R.J. Moat, D.G. Leo Prakash, W. Kockelmann, J. Quinta da Fonseca, M. Preuss, In situ neutron diffraction study of texture evolution and variant selection during the α→β→α phase transformation in Ti–6Al–4V, Acta Mater. 60(20) (2012) 7169-7182.

[77] S.C. Wang, M. Aindow, M.J. Starink, Effect of self-accommodation on α/α boundary populations in pure titanium, Acta Mater. 51(9) (2003) 2485-2503.

[78] H. Moustahfid, N. Gey, M. Humbert, M.J. Philippe, Study of the β-α Phase Transformations of a Ti-64 Sheet Induced from a High-Temperature β State and a High-Temperature α+β State, Metallurgical and Materials Transactions A 28 (1997) 51-61.

[79] N. Gey, M. Humbert, Characterization of the variant selection occuring during the α → β → α transformations of a cold rolled titanium sheet, Acta Mater. 50 (2002) 277-287.

[80] Z.S. Zhu, J.L. Gu, N.P. Chen, Variant selection in α → β → α phase transformation of cold rolled titanium sheet, Scr. Mater. 34 (1996) 1281-1286.

[81] N. Gey, M. Humbert, M.J. Philippe, Y. Combres, Investigation of the α- and β- texture evolution of hot rolled Ti-64 products, Materials Science and Engineering A 219 (1996) 80-88.

[82] G.C. Obasi, S. Birosca, J. Quinta da Fonseca, M. Preuss, Effect of β grain growth on variant selection and texture memory effect during α→β→α phase transformation in Ti–6 Al–4 V, Acta Mater. 60(3) (2012) 1048-1058.

[83] G.C. Obasi, S. Birosca, D.G. Leo Prakash, J. Quinta da Fonseca, M. Preuss, The influence of rolling temperature on texture evolution and variant selection during α→β→α phase transformation in Ti–6Al–4V, Acta Mater. 60(17) (2012) 6013-6024.

[84] D. Bhattacharyya, G.B. Viswanathan, R. Denkenberger, D. Furrer, H.L. Fraser, The role of crystallographic and geometrical relationships between α and β phases in an α/β titanium alloy, Acta Mater. 51(16) (2003) 4679-4691.

[85] A.W. Bowen, The Influence of Crystallographic Orientation on Tensile Behaviour in Strongly Textured Ti-6AI-4V, Mat. Sci. Eng. 40 (1979) 31-47.

[86] M. Peters, A. Gysler, G. Lutjering, Influence of Texture on Fatigue Properties of Ti-6AI-4V, Met. Trans. A 15A (1984).

[87] A.W. Bowen, The influence of crystallographic orientation on fatigue crack growth in strongly textured Ti-6Al-4V, Acta Met. 23 (1975) 1401-1409.

[88] I. Bantounas, D. Dye, T.C. Lindley, The effect of grain orientation on fracture morphology during high-cycle fatigue of Ti–6Al–4V, Acta Mater. 57(12) (2009) 3584-3595.

[89] A.W. Bowen, The influence of crystallographic orientation on the fracture toughness of strongly textured Ti-6Al-4V, Acta Met. 26 (1978) 1423-1433.

[90] É. Martin, M. Azzi, G.A. Salishchev, J. Szpunar, Influence of microstructure and texture on the corrosion and tribocorrosion behavior of Ti–6Al–4V, Tribol. Int. 43(5-6) (2010) 918-924.

[91] W.E. King, H.D. Barth, V.M. Castillo, G.F. Gallegos, J.W. Gibbs, D.E. Hahn, C. Kamath, A.M. Rubenchik, Observation of keyhole-mode laser melting in laser powder-bed fusion additive manufacturing, J. Mater. Process. Technol. 214(12) (2014) 2915-2925.

[92] V. Semak, A. Matsunawa, The role of recoil pressure in energy balance during laser materials processing, Journal of Physics D: Applied Physics 30 (1997) 12.

[93] X. He, J.T. Norris, P.W. Fuerschbach, T. DebRoy, Liquid metal expulsion during laser spot welding of 304 stainless steel, Journal of Physics D: Applied Physics 39(3) (2006) 525-534.

[94] A.F.H. Kaplan, M. Mizutani, S. Katayama, A. Matsunawa, Unbounded keyhole collapse and bubble formation during pulsed laser interaction with liquid zinc, Journal of Physics D: Applied Physics 35 (2002) 1218-1228.

[95] X. Xiao, C. Lu, Y. Fu, X. Ye, L. Song, Progress on Experimental Study of Melt Pool Flow Dynamics in Laser Material Processing, Liquid Metals, IntechOpen2021.

[96] S. Katayama, M. Mizutani, A. Matsunawa, Modelling of melting and solidification behaviour during laser spot welding, Science and Technology of Welding and Joining 2(1) (1997) 1-9.

[97] M. Rappaz, S.A. David, J.M. Vitek, L.A. Boatner, Analysis of Solidification Microstructures in Fe-Ni-Cr Single-Crystal Welds, Met. Trans. A 21A (1990) 1767-1782.

[98] S. Katayama, Y. Kobayashi, M. Mizutani, A. Matsunawa, Effect of vacuum on penetration and defects in laser welding, Journal of Laser Applications 13(5) (2001) 187-192.

[99] A. Matsunawa, J.-D. Kim, N. Seto, M. Mizutani, S. Katayama, Dynamics of keyhole and molten pool in laser welding, Journal of Laser Applications 10(6) (1998) 247-254.

[100] R. Cunningham, C. Zhao, N.D. Parab, C. Kantzos, J. Pauza, K. Fezzaa, T. Sun, A.D. Rollett, Keyhole threshold and morphology in laser melting revealed by ultrahigh-speed x-ray imaging, Science 363 (2019) 849-852.

[101] N.D. Parab, C. Zhao, R. Cunningham, L.I. Escano, K. Fezzaa, W. Everhart, A.D. Rollett, L. Chen, T. Sun, Ultrafast X-ray imaging of laser-metal additive manufacturing processes, J Synchrotron Radiat 25(Pt 5) (2018) 1467-1477.

[102] C. Zhao, K. Fezzaa, R.W. Cunningham, H. Wen, F. De Carlo, L. Chen, A.D. Rollett, T. Sun, Real-time monitoring of laser powder bed fusion process using high-speed X-ray imaging and diffraction, Sci Rep 7(1) (2017) 3602.

[103] C. Zhao, N.D. Parab, X. Li, K. Fezzaa, W. Tan, A.D. Rollett, T. Sun, Critical instability at moving keyhole tip generates porosity in laser melting, Science 370(6520) (2020) 1080-1086.

[104] R. Sahoo, T. Debroy, M.J. McNallan, Surface Tension of Binary Metal Surface Active Solute Systems under Conditions Relevant to Welding Metallurgy, Metallurgical Transactions B 19B (1988) 483-491.

[105] C.X. Zhao, C. Kwakernaak, Y. Pan, I.M. Richardson, Z. Saldi, S. Kenjeres, C.R. Kleijn, The effect of oxygen on transitional Marangoni flow in laser spot welding, Acta Mater. 58(19) (2010) 6345-6357.

[106] A. Robert, T. DebRoy, Geometry of Laser Spot Welds from Dimensionless Numbers, Metallurgical and Materials Transactions B 32B (2001) 941-947.

[107] J. Zhou, H.-L. Tsai, P.-C. Wang, Transport Phenomena and Keyhole Dynamics during Pulsed Laser Welding, Journal of Heat Transfer 128(7) (2006) 680-690.

[108] T. Mukherjee, V. Manvatkar, A. De, T. DebRoy, Dimensionless numbers in additive manufacturing, Journal of Applied Physics 121(6) (2017).

[109] T. Mukherjee, J.S. Zuback, A. De, T. DebRoy, Printability of alloys for additive manufacturing, Sci Rep 6 (2016) 19717.

[110] R. Trivedi, W. Kurz, Solidification Microstructures: A Conceptual Approach, Acta Metallurgica et Materialia 42 (1994) 15-23.

[111] Y. Lee, M. Nordin, S.S. Babu, D.F. Farson, Effect of fluid convection on dendrite arm spacing in laser deposition, Metallurgical and Materials Transactions B 45(4) (2014) 1520-1529.

[112] J.D. Hunt, Steady State Columnar and Equiaxed Growth of Dendrites and Eutectic, Mat. Sci. Eng. 65 (1984) 75-83.

[113] M. Gaumann, R. Trivedi, W. Kurz, Nucleation ahead of the advancing interface in directional solidification, Materials Science and Engineering A 226-228 (1997) 763-769.

[114] M. Rappaz, C.A. Gandin, J.-L. Desbiolles, P. Thevoz, Prediction of grain structures in various solidification processes, Metallurgical and Materials Transactions A 27(3) (1996) 695-705.

[115] Y. Lee, Simulation of Laser Additive Manufacturing and its Applications, Welding Engineering, Ohio State University, 2015.

[116] N. Raghavan, S. Simunovic, R. Dehoff, A. Plotkowski, J. Turner, M. Kirka, S. Babu, Localized melt-scan strategy for site specific control of grain size and primary dendrite arm spacing in electron beam additive manufacturing, Acta Mater. 140 (2017) 375-387.

[117] G. Ischia, H.-R. Wenk, L. Lutterotti, F. Berberich, Quantitative Rietveld texture analysis of zirconium from single synchrotron diffraction images, J. Appl. Crystallogr. 38(2) (2005) 377-380.

[118] S. Malinova, S. W., Z. Guoa, C.C. Tangb, A.E. Longa, Synchrotron X-ray diffraction study of the phase transformations in titanium alloys, Mater. Charact. 48 (2002) 279– 295.

[119] E. Cakmak, H. Choo, K. An, Y. Ren, A synchrotron X-ray diffraction study on the phase transformation kinetics and texture evolution of a TRIP steel subjected to torsional loading, Acta Mater. 60(19) (2012) 6703-6713.

[120] N. Haghdadi, R. DeMott, P.L. Stephenson, X.Z. Liao, S.P. Ringer, S. Primig, Five-parameter characterization of intervariant boundaries in additively manufactured Ti-6Al-4V, Mater. Des. 196 (2020) 109177.

[121] M.J. Quintana, M.J. Kenney, P. Agrawal, P.C. Collins, Texture Analysis of Additively Manufactured Ti-6Al-4V Deposited Using Different Scanning Strategies, Metall. Mater. Trans. A 51(12) (2020) 6574-6583.

[122] L. Lu, J.W. Huang, D. Fan, B.X. Bie, T. Sun, K. Fezzaa, X.L. Gong, S.N. Luo, Anisotropic deformation of extruded magnesium alloy AZ31 under uniaxial compression: A study with simultaneous in situ synchrotron x-ray imaging and diffraction, Acta Mater. 120 (2016) 86-94.

[123] Q. Guo, C. Zhao, M. Qu, L. Xiong, S.M.H. Hojjatzadeh, L.I. Escano, N.D. Parab, K. Fezzaa, T. Sun, L. Chen, In-situ full-field mapping of melt flow dynamics in laser metal additive manufacturing, Addit. Manuf. 31 (2020).

[124] L. Aucott, H. Dong, W. Mirihanage, R. Atwood, A. Kidess, S. Gao, S. Wen, J. Marsden, S. Feng, M. Tong, T. Connolley, M. Drakopoulos, C.R. Kleijn, I.M. Richardson, D.J. Browne, R.H. Mathiesen, H.V. Atkinson, Revealing internal flow behaviour in arc welding and additive manufacturing of metals, Nat Commun 9(1) (2018) 5414.

[125] S.M.H. Hojjatzadeh, N.D. Parab, W. Yan, Q. Guo, L. Xiong, C. Zhao, M. Qu, L.I. Escano, X. Xiao, K. Fezzaa, W. Everhart, T. Sun, L. Chen, Pore elimination mechanisms during 3D printing of metals, Nat Commun 10(1) (2019) 3088.

[126] A.A. Martin, N.P. Calta, S.A. Khairallah, J. Wang, P.J. Depond, A.Y. Fong, V. Thampy, G.M. Guss, A.M. Kiss, K.H. Stone, C.J. Tassone, J. Nelson Weker, M.F. Toney, T. van Buuren, M.J. Matthews, Dynamics of pore formation during laser powder bed fusion additive manufacturing, Nat Commun 10(1) (2019) 1987.

[127] Q. Guo, C. Zhao, L.I. Escano, Z. Young, L. Xiong, K. Fezzaa, W. Everhart, B. Brown, T. Sun, L. Chen, Transient dynamics of powder spattering in laser powder bed fusion additive manufacturing process revealed by in-situ high-speed high-energy x-ray imaging, Acta Mater. 151 (2018) 169-180.

[128] L.I. Escano, N.D. Parab, L. Xiong, Q. Guo, C. Zhao, K. Fezzaa, W. Everhart, T. Sun, L. Chen, Revealing particle-scale powder spreading dynamics in powder-bed-based additive manufacturing process by high-speed x-ray imaging, Sci Rep 8(1) (2018) 15079.

[129] N.P. Calta, A.A. Martin, J.A. Hammons, M.H. Nielsen, T.T. Roehling, K. Fezzaa, M.J. Matthews, J.R. Jeffries, T.M. Willey, J.R.I. Lee, Pressure dependence of the laser-metal interaction under laser powder bed fusion conditions probed by in situ X-ray imaging, Addit. Manuf. 32 (2020).

[130] C.L.A. Leung, S. Marussi, R.C. Atwood, M. Towrie, P.J. Withers, P.D. Lee, In situ X-ray imaging of defect and molten pool dynamics in laser additive manufacturing, Nat Commun 9(1) (2018) 1355.

[131] T.R. Allen, W. Huang, J.R. Tanner, W. Tan, J.M. Fraser, B.J. Simonds, Energy-Coupling Mechanisms Revealed through Simultaneous Keyhole Depth and Absorptance Measurements during Laser-Metal Processing, Physical Review Applied 13(6) (2020).

[132] B.J. Simonds, J. Tanner, A. Artusio-Glimpse, P.A. Williams, N. Parab, C. Zhao, T. Sun, The causal relationship between melt pool geometry and energy absorption measured in real time during laser-based manufacturing, Applied Materials Today 23 (2021).

[133] S.A. Khairallah, T. Sun, B.J. Simonds, Onset of periodic oscillations as a precursor of a transition to pore-generating turbulence in laser melting, Additive Manufacturing Letters 1 (2021).

[134] C.L. Frederick, Control of grain structure in selective-electron beam melting of nickel-based superalloys, Ph.D. Dissertation, University of Tennessee 2018, https://trace.tennessee.edu/utk_graddiss/4952.

[135] A. Hammersley, FIT2D: an introduction and overview, European Synchrotron Radiation Facility Internal Report ESRF97HA02T 68 (1997) 58.

[136] L. Lutterotti, S. Matthies, H. Wenk, MAUD: a friendly Java program for material analysis using diffraction, IUCr: Newsletter of the CPD 21(14-15) (1999).

[137] L. Lutterotti, R. Vasin, H.-R. Wenk, Rietveld texture analysis from synchrotron diffraction images. I. Calibration and basic analysis, Powder Diffr. 29(1) (2014) 76-84.

[138] F. Bachmann, R. Hielscher, H. Schaeben, Texture Analysis with MTEX – Free and Open Source Software Toolbox, Solid State Phenomena 160 (2010) 63-68.

[139] A.M. Birt, V.K. Champagne, R.D. Sisson, D. Apelian, Microstructural analysis of Ti–6Al–4V powder for cold gas dynamic spray applications, Adv. Powder Technol. 26(5) (2015) 1335-1347.

[140] S.L. Lu, H.P. Tang, Y.P. Ning, N. Liu, D.H. StJohn, M. Qian, Microstructure and Mechanical Properties of Long Ti-6Al-4V Rods Additively Manufactured by Selective Electron Beam Melting Out of a Deep Powder Bed and the Effect of Subsequent Hot Isostatic Pressing, Metall. Mater. Trans. A 46(9) (2015) 3824-3834.

[141] M.G. Glavicic, P.A. Kobryn, T.R. Bieler, S.L. Semiatin, An automated method to determine the orientation of the high-temperature beta phase from measured EBSD data for the low-temperature alpha-phase in Ti–6Al–4V, Mat. Sci. Eng. A 351(1-2) (2003) 258-264.

[142] A. Pesach, E. Tiferet, S.C. Vogel, M. Chonin, A. Diskin, L. Zilberman, O. Rivin, O. Yeheskel, E.N. Caspi, Texture analysis of additively manufactured Ti-6Al-4V using neutron diffraction, Addit. Manuf. 23 (2018) 394-401.

[143] M. Neikter, R. Woracek, T. Maimaitiyili, C. Scheffzuk, M. Strobl, M.L. Antti, P. Akerfeldt, R. Pederson, C. Bjerken, Alpha texture variations in additive manufactured Ti-6Al-4V investigated with neutron diffraction, Addit. Manuf. 23 (2018) 225-234.

[144] T. Vilaro, C. Colin, J.D. Bartout, As-Fabricated and Heat-Treated Microstructures of the Ti-6Al-4V Alloy Processed by Selective Laser Melting, Metall. Mater. Trans. A 42A(10) (2011) 3190-3199.

[145] E. Cakmak, M.M. Kirka, T.R. Watkins, R.C. Cooper, K. An, H. Choo, W. Wu, R.R. Dehoff, S.S. Babu, Microstructural and micromechanical characterization of IN718 theta shaped specimens built with electron beam melting, Acta Mater. 108 (2016) 161-175.

[146] P. Nandwana, A. Plotkowski, R. Kannan, S. Yoder, R. Dehoff, Predicting geometric influences in metal additive manufacturing, Mater. Today Commun. 25 (2020) 101174.

[147] Z. Li, J. Li, Y. Zhu, X. Tian, H. Wang, Variant selection in laser melting deposited α + β titanium alloy, J. Alloys Compd. 661 (2016) 126-135.

[148] M.S. Fu, Y.R. Yuan, X. Ma, X. Lin, A study of alpha variant selection in laser solid forming Ti-6Al-4V, J. Alloys Compd. 792 (2019) 1261-1266.

[149] E. Farabi, P.D. Hodgson, G.S. Rohrer, H. Beladi, Five-parameter intervariant boundary characterization of martensite in commercially pure titanium, Acta Mater. 154 (2018) 147-160.

[150] J. Schindelin, I. Arganda-Carreras, E. Frise, V. Kaynig, M. Longair, T. Pietzsch, S. Preibisch, C. Rueden, S. Saalfeld, B. Schmid, J.Y. Tinevez, D.J. White, V. Hartenstein, K. Eliceiri, P. Tomancak, A. Cardona, Fiji: an open-source platform for biological-image analysis, Nat Methods 9(7) (2012) 676-82.

[151] J. Vaithilingam, R.D. Goodridge, R.J.M. Hague, S.D.R. Christie, S. Edmondson, The effect of laser remelting on the surface chemistry of Ti6al4V components fabricated by selective laser melting, J. Mater. Process. Technol. 232 (2016) 1-8.

[152] Q. Tao, Z. Wang, G. Chen, W. Cai, P. Cao, C. Zhang, W. Ding, X. Lu, T. Luo, X. Qu, M. Qin, Selective laser melting of CP-Ti to overcome the low cost and high performance trade-off, Addit. Manuf. 34 (2020).

[153] T. DebRoy, S. Basu, K. Mundra, Probing laser induced metal vaporization by gas dynamics and liquid pool transport phenomena, Journal of Applied Physics 70(3) (1991) 1313-1319.

[154] J.M. Fishburn, M.J. Withford, D.W. Coutts, J.A. Piper, Study of the fluence dependent interplay between laser induced material removal mechanisms in metals: Vaporization, melt displacement and melt ejection, Applied Surface Science 252(14) (2006) 5182-5188.

[155] S. Basu, T. DebRoy, Liquid metal expulsion during laser irradiation, Journal of Applied Physics 72(8) (1992) 3317-3322.

[156] R. Rai, J.W. Elmer, T.A. Palmer, T. DebRoy, Heat transfer and fluid flow during keyhole mode laser welding of tantalum, Ti–6Al–4V, 304L stainless steel and vanadium, Journal of Physics D: Applied Physics 40(18) (2007) 5753-5766.

[157] Ø. Grong, Metallurgical modelling of welding, Institute of materials London1997.

[158] K.C. Mills, Recommended values of thermophysical properties for selected commercial alloys, Woodhead Publishing2002.

[159] J.W. Elmer, T.A. Palmer, S.S. Babu, W. Zhang, T. DebRoy, Phase transformation dynamics during welding of Ti–6Al–4V, Journal of Applied Physics 95(12) (2004) 8327-8339.

[160] T.E. Broderick, A.G. Jackson, H. Jones, F.H. Froes, The Effect of Cooling Conditions on the Microstructure of Rapidly Solidified Ti-6AI-4V, Met. Trans. A 16A (1985) 1951-1958.

[161] J. Raplee, A. Plotkowski, M.M. Kirka, R. Dinwiddie, A. Okello, R.R. Dehoff, S.S. Babu, Thermographic Microstructure Monitoring in Electron Beam Additive Manufacturing, Sci Rep 7 (2017) 43554.

[162] V. Thampy, A.Y. Fong, N.P. Calta, J. Wang, A.A. Martin, P.J. Depond, A.M. Kiss, G. Guss, Q. Xing, R.T. Ott, A. van Buuren, M.F. Toney, J.N. Weker, M.J. Kramer, M.J. Matthews, C.J. Tassone, K.H. Stone, Subsurface Cooling Rates and Microstructural Response during Laser Based Metal Additive Manufacturing, Sci Rep 10(1) (2020) 1981.

[163] C. Kenel, D. Grolimund, X. Li, E. Panepucci, V.A. Samson, D.F. Sanchez, F. Marone, C. Leinenbach, In situ investigation of phase transformations in Ti-6Al-4V under additive manufacturing conditions combining laser melting and high-speed micro-X-ray diffraction, Sci Rep 7(1) (2017) 16358.

[164] A. Sakellariou, T. Sawkins, T. Senden, A. Limaye, X-ray tomography for mesoscale physics applications, Physica A: Statistical mechanics and its applications 339(1-2) (2004) 152-158.

[165] F. Fani, E. Schena, P. Saccomandi, S. Silvestri, CT-based thermometry: an overview, Int J Hyperthermia 30(4) (2014) 219-27.

[166] D. Holland-Moritz, A. Schmon, K. Aziz, G. Pottlacher, F. Kargl, Density of liquid Ti-6Al-4V, EPJ Web of Conferences 151 (2017).

[167] J.J.Z. Li, W.L. Johnson, W.-K. Rhim, Thermal expansion of liquid Ti–6Al–4V measured by electrostatic levitation, Applied Physics Letters 89(11) (2006).

[168] C.C. M. Boivineau, D. Doytier, V. Eyraud, M.-H. Nadal, B. Wilthan, and G. Pottlacher, Thermophysical Properties of Solid and Liquid Ti-6Al-4V (TA6V) Alloy, International Journal of Thermophysics 27(2) (2006) 507-529.

[169] A.J. Gilbert, M.R. Deinert, Neutron tomography of axisymmetric flow fields in porous media, Nuclear Instruments and Methods in Physics Research Section B: Beam Interactions with Materials and Atoms 301 (2013) 23-28.

Appendix

MATLAB code for conversion of radiography images to density and temperature maps

```
%% Code written by Rakesh R. Kamath, UT Knoxville (latest update:
06/01/2022)

% Function: Convert radiography images to density and temperature maps
% using Beer-Lambert's law

%% Read Use_Image sequence and concatenate into a 3D matrix

Tot_Im = 641; %Total number of Use_Images
Srt_Im = 50; % 0 microsec is at Use_Image 39
End_Im = 300; % Calculate end frames by hand
Use_Im = End_Im-Srt_Im; % Used Use_Images
y_pix = 384; %Total y-pixels (top-bottom)
y_pix_i = 80; % Ar-Metal interface
x_pix = 720; %Total x-pixels (left-right)
A = zeros(y_pix,x_pix,Use_Im); %Dummy Use_Image pixel data matrix

for i=1:Use_Im
    filename = ['Image_' num2str((i+Srt_Im-1),'%d') '.tif']; % Use
NameChanger software to change name to this format
    A(:,:,i) = imread(filename);
end

XTickLabels = 0:(x_pix-1);
YTickLabels = 0:(y_pix-1);
XTickLabels = 2*XTickLabels; % Each pixel is 2 microns
YTickLabels = 2*YTickLabels; % Each pixel is 2 microns
CustomXLabels = string(XTickLabels);
CustomYLabels = string(YTickLabels);
CustomXLabels(mod(XTickLabels,((x_pix-1)/9)) ~= 0) = " ";
CustomYLabels(mod(YTickLabels,((y_pix-1)/5)) ~= 0) = " ";

figure
h =
heatmap(A(:,:,200),'Colormap',gray,'YLabel','Depth(\mum)','XLabel','Wid
th(\mum)')
h.FontSize = 12;
h.XDisplayLabels = CustomXLabels;
h.YDisplayLabels = CustomYLabels;

%% STEP #1: Convert to density

I_Ar = max(max(A(:,:,1)));
I_Ti64 = min(min(A(:,:,1)));
Den_Ar = 1.652; % Units: kg/m^3
Den_Ti64 = 4430; % Units: kg/m^3
```

```
slope = (Den_Ti64-Den_Ar)/(log(I_Ti64)-log(I_Ar));  % Slope = mu *
thickness; assuming thickness is same for both Ar and Ti64

Density_Dist = zeros(y_pix,x_pix,Use_Im); % Dummy matrix for density

for z=1:Use_Im
    for y=1:y_pix
        for x=1:x_pix
            Density_Dist(y,x,z) = Den_Ar +
(slope*(log(A(y,x,z)/I_Ar)));
        end
    end
end

figure
h =
heatmap(Density_Dist(:,:,200),'Colormap',jet,'YLabel','Depth(\mum)','XL
abel','Width(\mum)')
h.FontSize = 12;
h.XDisplayLabels = CustomXLabels;
h.YDisplayLabels = CustomYLabels;

%% STEP #2: Smoothen noisy density maps

% Discard the argon-filled ambient area above the sample

Density_Dist_1 = zeros((y_pix-y_pix_i),x_pix,Use_Im);
Smooth_Density_Dist = zeros((y_pix-y_pix_i),x_pix,Use_Im);

for z=1:Use_Im
    for y=1:(y_pix-y_pix_i)
        for x=1:x_pix
            Density_Dist_1(y,x,z) = Density_Dist((y+y_pix_i),x,z);
        end
    end
end

% Use a smoothening function for all images

h = ones(5,5)/25; % 5-point moving average

for z=1:Use_Im
    Smooth_Density_Dist(:,:,z) = imfilter(Density_Dist_1(:,:,z),h);
end

XTickLabels = 0:(x_pix-1);
YTickLabels = 0:(y_pix-y_pix_i-1);
XTickLabels = 2*XTickLabels; % Each pixel is 2 microns
YTickLabels = 2*YTickLabels; % Each pixel is 2 microns
CustomXLabels = string(XTickLabels);
CustomYLabels = string(YTickLabels);
CustomXLabels(mod(XTickLabels,((x_pix-1)/9)) ~= 0) = " ";
```

```
CustomYLabels(mod(YTickLabels,((y_pix-y_pix_i-1)/7)) ~= 0) = " ";

figure
h =
heatmap(Smooth_Density_Dist(:,:,200),'Colormap',jet,'YLabel','Depth(\mu
m)','XLabel','Width(\mum)')
h.FontSize = 12;
h.XDisplayLabels = CustomXLabels;
h.YDisplayLabels = CustomYLabels;

figure
surf(Smooth_Density_Dist(:,:,200))
xlabel('Width(\mum)')
ylabel('Depth(\mum)')
zlabel('Smoothed Density (kg/m^3)')

figure
surf(Density_Dist((y_pix_i:y_pix),:,200))
xlabel('Width(\mum)')
ylabel('Depth(\mum)')
zlabel('Raw Density (kg/m^3)')

%% STEP #3: Find density correction matrix and apply to the full time
series

Density_Corr = zeros((y_pix-y_pix_i),x_pix);

for y=1:(y_pix-y_pix_i)
    for x=1:x_pix
        Density_Corr(y,x) = Den_Ti64/Density_Dist_1(y,x,1);
    end
end

Corr_Density_Dist = zeros((y_pix-y_pix_i),x_pix,Use_Im);

for z=1:Use_Im
    for y=1:(y_pix-y_pix_i)
        for x=1:x_pix
            Corr_Density_Dist(y,x,z) =
Density_Corr(y,x)*Density_Dist_1(y,x,z);
        end
    end
end

% Plots - For loop and make a video

XTickLabels = 0:(x_pix-1);
YTickLabels = 0:(y_pix-y_pix_i-1);
XTickLabels = 2*XTickLabels; % Each pixel is 2 microns
YTickLabels = 2*YTickLabels; % Each pixel is 2 microns
CustomXLabels = string(XTickLabels);
CustomYLabels = string(YTickLabels);
```

```
CustomXLabels(mod(XTickLabels,((x_pix-1)/9)) ~= 0) = " ";
CustomYLabels(mod(YTickLabels,((y_pix-y_pix_i-1)/7)) ~= 0) = " ";

figure
h =
heatmap(Corr_Density_Dist(:,:,25),'Colormap',jet,'ColorLimits',[3000
4500],'YLabel','Depth(\mum)','XLabel','Width(\mum)')
h.FontSize = 12;
h.XDisplayLabels = CustomXLabels;
h.YDisplayLabels = CustomYLabels;

figure
h =
heatmap(Corr_Density_Dist(:,:,50),'Colormap',jet,'ColorLimits',[3000
4500],'YLabel','Depth(\mum)','XLabel','Width(\mum)')
h.FontSize = 12;
h.XDisplayLabels = CustomXLabels;
h.YDisplayLabels = CustomYLabels;

figure
h =
heatmap(Corr_Density_Dist(:,:,100),'Colormap',jet,'ColorLimits',[3000
4500],'YLabel','Depth(\mum)','XLabel','Width(\mum)')
h.FontSize = 12;
h.XDisplayLabels = CustomXLabels;
h.YDisplayLabels = CustomYLabels;

figure
h =
heatmap(Corr_Density_Dist(:,:,200),'Colormap',jet,'ColorLimits',[3000
4500],'YLabel','Depth(\mum)','XLabel','Width(\mum)')
h.FontSize = 12;
h.XDisplayLabels = CustomXLabels;
h.YDisplayLabels = CustomYLabels;

% Histogram plots

[N1,edges1] = histcounts(Corr_Density_Dist(:,:,25));
edges1 = edges1(2:end) - (edges1(2)-edges1(1))/2;

[N2,edges2] = histcounts(Corr_Density_Dist(:,:,50));
edges2 = edges2(2:end) - (edges2(2)-edges2(1))/2;

[N3,edges3] = histcounts(Corr_Density_Dist(:,:,100));
edges3 = edges3(2:end) - (edges3(2)-edges3(1))/2;

[N4,edges4] = histcounts(Corr_Density_Dist(:,:,200));
edges4 = edges4(2:end) - (edges4(2)-edges4(1))/2;

figure
plot(edges1, N1)
hold on
```

```
plot(edges2, N2)
hold on
plot(edges3, N3)
hold on
plot(edges4, N4)
hold on
legend({'Image 25','Image 50','Image 100','Image
200'},'Location','northeast','fontsize',12)
xlabel('Density (kg/m^3)','fontsize',15,'fontweight','bold')
ylabel('Counts','fontsize',15,'fontweight','bold')


%% STEP #4: Convert density to temperature

% Solid (270K to 1860K)

solid = [270    4430
1040    4389.160907
1050    4386.58017
1060    4383.483286
1070    4383.483286
1080    4381.934844
1090    4380.90255
1100    4378.83796
1110    4377.805666
1120    4376.773371
1130    4376.773371
1140    4377.805666
1150    4377.805666
1160    4376.773371
1170    4375.224929
1180    4372.644193
1190    4373.16034
1200    4367.998867
1210    4370.063456
1220    4367.998867
1230    4364.901983
1240    4362.837394
1250    4361.805099
1260    4360.256657
1270    4360.772805
1280    4359.224363
1290    4357.675921
1300    4356.127479
1310    4354.062889
1320    4353.030595
1330    4351.482153
1340    4350.966006
1350    4349.417564
1360    4347.869122
1370    4347.869122
1380    4343.223796
1390    4344.256091
```

```
1400    4337.030028
1410    4339.610765
1420    4337.030028
1430    4335.997734
1440    4335.481586
1450    4333.933144
1460    4330.836261
1470    4330.836261
1480    4330.836261
1490    4327.739377
1500    4323.610198
1510    4323.610198
1520    4322.061756
1530    4321.029462
1540    4317.932578
1550    4317.416431
1560    4316.384136
1570    4316.384136
1580    4313.287252
1590    4310.190368
1600    4310.190368
1610    4306.577337
1620    4308.125779
1630    4302.964306
1640    4304.512748
1650    4300.383569
1660    4300.899717
1670    4298.31898
1680    4298.835127
1690    4296.254391
1700    4297.286685
1710    4289.028329
1720    4287.996034
1730    4287.996034
1740    4285.415297
1750    4282.834561
1760    4281.286119
1770    4280.769972
1780    4277.15694
1790    4276.124646
1800    4273.543909
1810    4270.963173
1820    4266.833994
1830    4267.350142
1840    4261.672521
1850    4259.607932
1860    4260.124079
];

% Mushy zone (1870K to 1920K) - Linear solidification model used

mushy_solid = [1870 4258.575637 1
1880    4257.027195 0.8
1890    4254.446459 0.6
```

```
1900    4252.38187  0.4
1910    4252.38187  0.2
1920    4251.349575 0];

mushy_liquid = [1870    4146.32068  0
1880    4140.126912 0.2
1890    4139.094618 0.4
1900    4139.094618 0.6
1910    4135.481586 0.8
1920    4130.320113 1];

mushy = [mushy_solid(:,1)
((mushy_solid(:,2).*mushy_solid(:,3))+(mushy_liquid(:,2).*mushy_liquid(
:,3)))];

% Liquid_1 (1930K to 3560K)

liquid = [1930  4126.707082
1940    4127.223229
1950    4126.190935
1960    4120.513314
1970    4117.932578
2050    4028
2100    4006
2150    3983
2200    3961
2250    3938
2300    3915
2350    3893
2400    3870
2450    3848
2500    3825
2550    3802
2592    3783];

%% Fitting (Easier way is to flip columns and later use polyval. Isn't
done because a 2nd degree polynomial will become 1/2 degree which is
unavailable in Matlab)

% Density-Temperature fitting

p1 = polyfit(solid(:,1),solid(:,2),2);
p2 = polyfit(mushy(:,1),mushy(:,2),1);
p3 = polyfit(liquid(:,1),liquid(:,2),1);

% Mushy zone - Temperature vs phase fraction

T_mushy = linspace(1870,1920,50)';
phase_fraction = linspace(0,1,50)';
T_fraction = [T_mushy phase_fraction];
p4 = polyfit(T_fraction(:,1),T_fraction(:,2),1);
```

```
%% For Variation plot

T_solid = linspace(270,1860,1590);
Den_solid = polyval(p1,T_solid);

T_mushy = linspace(1870,1920,50);
Den_mushy = polyval(p2,T_mushy);

T_liquid = linspace(1930,3560,1630);
Den_liquid = polyval(p3,T_liquid);

T_mushy = linspace(1870,1920,50);
Liq_frac = polyval(p4,T_mushy);

figure
plot(T_solid,Den_solid,'r',solid(:,1),solid(:,2),'b--o')
hold on
plot(T_mushy,Den_mushy,'r',mushy(:,1),mushy(:,2),'b--o')
hold on
plot(T_liquid,Den_liquid,'r',liquid(:,1),liquid(:,2),'b--o')
hold off
legend({'Fit','Literature'},'Location','northeast','fontsize',12)
xlabel('Temperature (K)','fontsize',15,'fontweight','bold')
ylabel('Density (kg/m^3)','fontsize',15,'fontweight','bold')

figure
plot(T_mushy,Liq_frac,'r',T_fraction(:,1),T_fraction(:,2),'b--o')
legend({'Fit','Literature'},'Location','northeast','fontsize',12)
xlabel('Temperature (K)','fontsize',15,'fontweight','bold')
ylabel('Liquid Fraction','fontsize',15,'fontweight','bold')

%% Convert density to temperature

Temp_dist = zeros((y_pix-y_pix_i),x_pix,Use_Im);

z = 100
%for z=1:Use_Im
    for y=1:(y_pix-y_pix_i)
        for x=1:x_pix

if((Corr_Density_Dist(y,x,z)>=3255)&&(Corr_Density_Dist(y,x,z)<=Den_Ti6
4))
                if(Corr_Density_Dist(y,x,z)>=4260)
                p1_temp = [p1(1,1),p1(1,2),p1(1,3)-
Corr_Density_Dist(y,x,z)];
                r1 = roots(p1_temp);
                Temp_dist(y,x,z) = max(r1);
                elseif(Corr_Density_Dist(y,x,z)<=4120)
                p3_temp = [p3(1,1),p3(1,2)-Corr_Density_Dist(y,x,z)];
                r3 = roots(p3_temp);
                Temp_dist(y,x,z) = max(r3);
                else
```

```
                p2_temp = [p2(1,1),p2(1,2)-Corr_Density_Dist(y,x,z)];
                r2 = roots(p2_temp);
                Temp_dist(y,x,z) = max(r2);
                end
            elseif(Corr_Density_Dist(y,x,z)>Den_Ti64)
            Temp_dist(y,x,z) = 270;
            else
            Temp_dist(y,x,z) = 3560;
            end
        end
    end
%end

figure(1)
h = heatmap(Temp_dist(:,:,25),'Colormap',jet,'ColorLimits',[250
3600],'YLabel','Depth(\mum)','XLabel','Width(\mum)')
h.FontSize = 12;
h.XDisplayLabels = CustomXLabels;
h.YDisplayLabels = CustomYLabels;

figure(2)
h = heatmap(Temp_dist(:,:,50),'Colormap',jet,'ColorLimits',[250
3600],'YLabel','Depth(\mum)','XLabel','Width(\mum)')
h.FontSize = 12;
h.XDisplayLabels = CustomXLabels;
h.YDisplayLabels = CustomYLabels;

figure(3)
h = heatmap(Temp_dist(:,:,100),'Colormap',jet,'ColorLimits',[250
3600],'YLabel','Depth(\mum)','XLabel','Width(\mum)')
h.FontSize = 12;
h.XDisplayLabels = CustomXLabels;
h.YDisplayLabels = CustomYLabels;

figure(4)
h = heatmap(Temp_dist(:,:,200),'Colormap',jet,'ColorLimits',[250
3600],'YLabel','Depth(\mum)','XLabel','Width(\mum)')
h.FontSize = 12;
h.XDisplayLabels = CustomXLabels;
h.YDisplayLabels = CustomYLabels;
```

Vita

Rakesh R. Kamath was born to Rekha Kamath (née Shenoy) and Rajaram Kamath at Kundapura, Karnataka State, India in 1992. While being curious about many things from a young age, Rakesh was most fascinated by chemistry and history. He decided to direct his curiosity and devote his time to learn and understand a branch of knowledge with its roots in the chemical sciences – Metallurgy and Materials Science. Rakesh started his journey by receiving his Bachelors in Technology (B.Tech) in Metallurgical and Materials Engineering from the National Institute of Technology, Karnataka in 2014. A significant highlight of this period in his career was his first exposure to materials research and being awestruck with Cahn's treatise on the history of materials science. Further, he went on earn a Masters in Engineering (M.E.) from the Indian Institute of Science, Bengaluru in 2016, after gaining research experience in the field of mechanical behavior of materials. For the next step in his research journey, Rakesh joined Prof. Hahn Choo's group at the University of Tennessee Knoxville in 2016 to pursue a Ph.D. in Materials Science and Engineering. During his stint at UTK, he was lucky to get an opportunity to work with excellent mentors and peers on understanding process-structure relationships in novel manufacturing processes using x-ray and neutron probes at large-scale user facilities. Rakesh is grateful to have been able to learn, research and re-learn materials science over the past decade and looks forward to continuing research into interesting materials phenomena in the future as he steps into his next role as a postdoctoral scholar at the Argonne National Laboratory, Chicago, IL.